

**Fabrication and Characterization of Semiconductor Ion Traps for
Quantum Information Processing**

by

Daniel Lynn Stick

A dissertation submitted in partial fulfillment
of the requirements for the degree of
Doctor of Philosophy
(Physics)
in The University of Michigan
2007

Doctoral Committee:

Professor Christopher R. Monroe, Chair
Professor Georg Raithel
Professor Jens Zorn
Associate Professor Cagliyan Kurdak
Assistant Professor Yaoyun Shi

©

Daniel Lynn Stick	2007
All Rights Reserved	

“I aint no bum, Mick. I aint no bum.”

– Rocky Balboa

To my parents

ACKNOWLEDGEMENTS

First, I would like to thank Chris Monroe for his guidance in my scientific career. I was unsure of what sub-field of physics that I wanted to pursue before I applied to graduate school, and it was the tour that he gave when I visited Michigan that sold me on this research. The responsibility he gave me early in my graduate career gave me confidence in my abilities, and his “forget your classes” attitude freed up a lot of time for research. I feel very fortunate to have had him as an advisor.

Winfried Hensinger has also had a profound impact on me; his determination and painful-yet-ultimately-successful commitment to searching parameter space ingrained in me the importance of hard work. I spent many long days and long nights in the lab with Winni, and greatly appreciate his friendship and influence on me as a scientist.

During my first few years of research I spent a good fraction of my time at the Laboratory for Physical Sciences (LPS), where I used the cleanroom to fabricate ion traps in collaboration with Keith Schwab. His frequent fabrication advice and willingness to help were instrumental in the ultimate success of this project. I will have fond memories of my time spent at LPS not just from the draining but strangely satisfying cleanroom work, but also from the camaraderie with Keith and the other researchers there. In particular Kevin Eng was an invaluable source of practical fabrication knowledge, and is responsible for helping me develop several key processing steps. I also want to acknowledge additional help from Benedetta Camarota, Carlos Sanchez, Kenton Brown, Dan Sullivan, Akshay Naik, Matt LaHaye, Olivier Buu, Harish Bhaskaran, and Alex Hutchinson. The staff at LPS was also extremely helpful, in particular Scott Horst and Steve Brown for their ICP help, Lisa Lucas for equipment

training, Toby Olver for general advice and trouble shooting, Lynn Calhoun for MBE growth, Russell for wafer thinning, and Les Lorenz for machining. Without all these people supporting me with their expertise and direct help I am sure that my best efforts would have been in vain.

I could not have asked for a better lab to work in at Michigan. My lab mates have made my time here very enjoyable and have been instrumental in my training as a scientist. I need to particularly acknowledge those who I have worked closely with on the GaAs microtrap projects with, including Martin Madsen for developing the idea of a semiconductor fabricated trap, and Winfried Hensinger and Steve Olmschenk for testing it. During the T trap project I had the privilege of also working with Dave Hucul and Mark Yeo in both the construction and testing phases. Few graduate school memories remain as vivid to me as listening to the Tijuana Brass late at night while working on the T trap vacuum chamber. Again, Winni's persistence in the construction of this trap helped push us through whatever design flaws we had chosen to implement.

Recently I have had the pleasure of working closely with Jon Sterk, Liz Otto, Dan Cook, and Yisa Rumala. I have spent a lot of time with Jon in particular over the last few years, and owe him for the hard work that he spent on the vacuum chamber design and novel trap testing. I know the project is in capable hands as he assumes leadership of this project. Working with these other new students as they entered the lab has helped me immensely; their questions have made me think through ideas that I had grown to assume, and their new perspectives have injected a needed dose of creativity into the experiment.

Although I haven't worked as closely with the other lab members as I have with those on my experiment, they have all been very helpful in broadening my knowledge of atomic physics. In particular, I have had many interesting and useful physics discussions with Louis Deslauriers, as well as interesting discussions outside of physics. Through interactions in group meetings, doing general lab work, around the coffee maker, I am grateful for their friendship and scientific skills. Paul Haljan, Boris Blinov, Ming-Shien Chang, Dzmitry Matsukevich, Peter Maunz, Dave Moehring,

Kelly Younge, Andrew Chew, Rudy Kohn, Russ Miller, Mark Acton, Kathy-Anne Brickman, and Patty Lee have all made my experience in Chris' lab a wonderful one.

Over the last few years I have been fortunate to interact with other groups and researchers. In particular Dave Wineland, John Bollinger, and their students at NIST have always been willing to give advice, and the combined advances we have made, as well as those in the other ion trapping groups at Oxford and Innsbruck, have proved the efficacy of collaboration over competition. I am also very grateful to Dick Slusher and Matt Blain for their foundry work on ion traps which we have tested. Without their efforts this field would not be attracting the attention today, and I sincerely wish them well in the future. Michael Pedersen, who I have never met but who is working at MEMS Exchange on building us an ion trap, also deserves recognition in the trap development category. I would be remiss if I did not express a great deal of thanks to Henry Everitt, who is responsible in no small part for the generous support of novel ion trap development for quantum computing. I also want to thank Jun Ye and Ben Lev for their help with my NRC application.

Those who laid the framework for my physics career deserve thanks as well. Mrs. Knighton, my middle school science teacher, and particularly Mr. Wood, my high school physics teacher, did more than they can imagine in fostering and supporting my love of science. They have been influential in both my scientific career and the many others they have taught. As an undergraduate at Caltech, I was blessed to do research with both Hideo Mabuchi and Erik Winfree. I'm sure they put up with plenty of frustrating moments as I was just getting my feet wet in research, but I am extremely happy that they stuck with me.

Also I need to thank the other members of my committee, comprising Yaoyun Shi, Cagliyan Kurdak, Jens Zorn, and Georg Raithel. I have been fortunate to interact with all of these faculty members in my prelim and outside of it. The field of quantum computing is a large and growing one, in no small part to the theoretical work being done by those like Prof. Shi. Prof. Kurdak has been generous with offering fabrication advice as well as facilities for annealing our receptacles. As my E&M teacher, Prof. Raithel was a thorough instructor, as well as a flexible one when I needed to do

fabrication work in Washington. I saw Prof. Zorn fairly regularly in the hallway and the machine shop, and enjoyed our conversations and the advice he gave.

This is the catch-all paragraph for things I want to say which do not fit anywhere else. For one, I hold Keith and Winni most responsible for my original coffee addiction, and Chris for helping secure it with his purchase of the Gaggia Titanium. If I had to pick the inanimate object I will miss the most, it is this fantastic marvel of engineering. I also need to thank Rich Vallery for his help with the latex class file which I used for formatting this thesis.

I also need to thank all my friends who have made my graduate school experience a wonderful one. I won't thank the guys I play poker with every week, as I feel like my rough streak over the last few months and the money I have given you are enough. Li Yu, Misty Richards, Annamarie Pluhars, and Bob Sherwood in Washington - thank you for your hospitality. To my friends at GCF and Campus Chapel, particularly Rolf Bouma and Mark Roeda, thank you for your spiritual guidance and support. The creation that I have the privilege to investigate makes my life exciting and rewarding.

Finally, to my family, I owe perhaps the most. My dad and mom who pushed me to do well in school and fostered a recreational interest in science and math through outside engineering and science projects - you have been wonderful parents. I suppose after 27 years of informal education combined with 21 years of formal education, I might be ready to get a real job. And to you, Christina, for being so supportive of my work and putting up with my blank stares as I zone out into the work of atomic physics, I want to thank you with all my heart. Hopefully my lifelong love will be a sufficient thank you. If not, there's the prestige of being married to a PhD physicist.

TABLE OF CONTENTS

DEDICATION	ii
ACKNOWLEDGEMENTS	iii
LIST OF TABLES	x
LIST OF FIGURES	xi
ABSTRACT	xiv
CHAPTER	
1. Introduction to trapped ion quantum computing	1
1.1 Trapped Ions	1
1.2 Moore’s law and classical computing	2
1.3 Quantum Information	3
1.4 General quantum computing requirements	5
1.5 Quantum phenomena	5
1.6 What numbers are we really talking about?	7
1.7 Atomic physics of trapped ion quantum computing	8
2. The cadmium qubit	10
2.1 State detection and initialization	10
2.2 Qubit rotations and quantum gates	11
2.2.1 The ion’s motion	12
2.2.2 The ion’s internal states	13
2.2.3 Microwave transitions	16
2.2.4 Stimulated Raman Transitions	17
2.2.5 Laser cooling	22
2.2.6 Thermometry	23
3. Ion trapping fundamentals	26
3.1 The ponderomotive potential	26
3.2 The Mathieu equation	26
3.3 The pseudo-potential approximation	31
3.4 The 3 dimensional hyperbolic electrode trap	32

3.4.1	Ring and Fork Trap	33
3.4.2	Needle trap	36
3.5	Linear traps	36
3.5.1	Four rod trap	38
3.5.2	Single layer trap	50
3.5.3	Three layer trap	52
3.6	The surface trap	52
3.7	Computer simulations of electric fields from electrodes	53
4.	Experimental setup	59
4.1	Achieving ultra high vacuum (UHV)	59
4.2	The bake	59
4.3	The chamber	61
4.4	RF resonator	63
4.5	Ovens	66
4.6	Photoionization	68
4.7	Lasers and frequency modulation	70
4.8	Imaging system	74
4.9	Instrument control and data collection	75
5.	Scalability: Demonstrating junctions in the T trap	79
5.1	T trap fabrication	81
5.1.1	Photolithography	82
5.1.2	Dry film photoresist	83
5.2	Trap layout and electronics	84
5.3	Shuttling results	85
5.4	T trap lessons	86
6.	Scalability: Demonstrating a microfabricated gallium arsenide trap	92
6.1	Mechanical characterization	92
6.2	Power dissipation	94
6.3	Power scaling laws	96
6.4	Gallium Arsenide properties and MBE Growth	98
6.5	GaAs trap fabrication	100
6.5.1	Scribing, dicing, and thinning	100
6.5.2	Photoresist and standard procedures	102
6.5.3	Backside etching	103
6.5.4	Bondpad etching	108
6.5.5	Ohmic Contacts	111
6.5.6	Cantilever etching	113
6.5.7	Annealing	113
6.5.8	$\text{Al}_{0.7}\text{Ga}_{0.3}\text{As}$ etch	113

6.5.9	Attaching to chip carrier	114
6.5.10	Interconnects, RF grounding, and filtering	115
6.6	Experimental results	118
6.6.1	Operating parameters	118
6.6.2	Motional heating	121
6.6.3	Motionally sensitive carrier transition	124
6.7	Future work on two layer traps	130
7.	Other microfabricated traps	133
7.1	Lucent trap	133
7.1.1	Fabrication	133
7.1.2	Simulations	134
7.1.3	Operating parameters and results	139
7.2	Sandia trap	143
7.3	Polysilicon MEMS Exchange trap	146
8.	Sources of motional heating	150
8.1	Heating rate and spectral density of electric field noise	151
8.2	Thermal (Johnson) noise	152
8.3	Trap construction	153
8.4	Heating results	154
8.5	Future work - molybdenum trap	156
9.	Conclusion	158
	BIBLIOGRAPHY	159

LIST OF TABLES

Table

1.1	A CNOT gate truth table	9
6.1	ICP settings	111
6.2	CHA Recipe	112
6.3	Annealing recipe	114

LIST OF FIGURES

Figure

2.1	Detection and initialization of the $^{111}\text{Cd}^+$ qubit	12
2.2	Detection statistics for the $^{111}\text{Cd}^+$ qubit in the dark and bright states	13
2.3	Rabi flopping on the carrier transition using microwaves	18
2.4	Raman transition diagram	19
2.5	Schematic of the laser beams used in the detection, initialization, and motional coupling of an ion	20
2.6	Energy level diagram of Raman transitions and Clebsch-Gordan coef- ficients	21
2.7	Raman spectra showing the sideband asymmetry	25
3.1	Ideal hyperbolic trap	32
3.2	Stability diagram for an ideal hyperbolic trap	34
3.3	Ring and fork trap	35
3.4	Two needle trap	36
3.5	Linear traps	37
3.6	Ideal linear hyperbolic trap	38
3.7	Stability diagram for hyperbolic linear trap	39
3.8	Two layer linear trap	41
3.9	Trap strength and depth as a function of the aspect ratio	42
3.10	Conformal mapping of a two layer trap to parallel plate capacitors . .	44
3.11	Higher order anharmonic coefficients of the two layer trap at the trap center	46
3.12	Higher order anharmonic coefficients of the two layer trap as a function of distance from the trap center	47
3.13	Contour plot of the ponderomotive potential for a trap with rotated principal axes	49
3.14	Bridge junction for a two layer trap	51
3.15	Single layer trap geometry	52
3.16	Three layer trap	53
3.17	Surface trap	54
3.18	CPO user interface	56
3.19	CPO example of a surface trap	57
3.20	CPO example of a linear ion trap	57
3.21	CPO example of a surface junction trap	58
4.1	Typical vacuum chamber	60
4.2	CPGA socket	63
4.3	CPGA socket assembly and mounting block	64
4.4	Laser access in Magdeburg hemisphere vacuum chamber	65
4.5	RF cavity resonator	67

4.6	Cadmium ovens	69
4.7	Photoionization energy level diagram	71
4.8	Laser layout	77
4.9	Imaging system	78
5.1	Schematic of an ion trap array	80
5.2	The “T” trap - Overhead view	87
5.3	The “T” trap Junction	88
5.4	T Trap photoresist	88
5.5	Photoresist edge bead	89
5.6	T Trap photoresist removal	89
5.7	The photoresist radiating to the bottom left of the hole has uneven thicknesses.	90
5.8	T Trap dimensions	90
5.9	T Trap voltage	91
6.1	Transmission line model for GaAs electrodes	95
6.2	GaAs trap fabrication	101
6.3	Membrane etched parallel to the primary flat	104
6.4	Membrane etched perpendicular to the primary flat.	105
6.5	Punctured membrane.	106
6.6	Buckled membrane	108
6.7	Y trap membrane.	109
6.8	Shorted bond pads	112
6.9	Collapsed cantilevers	115
6.10	GaAs mounted on a ceramic LCC	116
6.11	The LCC mounting structure	117
6.12	CCD image of a trapped ion in the GaAs trap	119
6.13	Lifetime histogram of an ion in the GaAs trap	120
6.14	Linewidth of a $^{111}\text{Cd}^+$ ion in the GaAs trap	122
6.15	The boil-out lifetime of an uncooled ion	123
6.16	Dark state initialization and detection	124
6.17	Rabi flopping on the carrier transition in the GaAs trap	125
6.18	Raman frequency scan showing the carrier transition as well as the red and blue sidebands	125
6.19	Raman transition probabilities for time delays of 0 and 1000 μs . . .	126
6.20	Suppression of the Raman transition rate after a given delay time . .	129
6.21	Offset in the A and B coefficients of the Raman transition	130
6.22	Silicon substrate fabrication	132
7.1	Transverse image of the Lucent surface trap	135
7.2	Overhead view of the Lucent surface trap	136
7.6	Voltages applied to the surface trap to eliminate the static electric field at the RF node	138
7.7	The total DC potential applied to the surface trap	140
7.8	The total surface trap potential, including the pseudopotential and static potential	140
7.9	Principal axes of the surface trap	141

7.10	Axial potential of the trap	141
7.11	Applied voltages to surface trap	142
7.12	A conceptual design of a surface trap with on board optics and control circuitry	144
7.13	A series of junction electrode shapes which exhibit decreasing RF hump sizes	145
7.14	Sandia trap	146
7.15	MEMS Exchange polysilicon trap fabrication steps	148
7.16	Polysilicon trap up till metallization step	149
7.17	Micrograph of the finished polysilicon trap	149
8.1	Spectral density of electric field noise for different traps and ions . . .	151
8.2	Needle schematic	155
8.3	Heating rate in the needle trap as a function of trap frequency	156
8.4	Heating rate in the needle trap as a function of trap distance	157

ABSTRACT

Fabrication and Characterization of Semiconductor Ion Traps for Quantum Information Processing

by

Daniel Lynn Stick

Chair: Christopher R. Monroe

The electromagnetic manipulation of isolated ions has led to many advances in atomic physics, from laser cooling to precision metrology and quantum control. As technical capability in this area has grown, so has interest in building miniature electromagnetic traps for the development of large-scale quantum information processors. This thesis will primarily focus on using microfabrication techniques to build arrays of miniature ion traps, similar to techniques used in fabricating high component density microprocessors. A specific focus will be on research using a gallium arsenide/aluminum gallium arsenide heterostructure as a trap architecture, as well as the recent testing of different ion traps fabricated at outside foundries. The construction and characterization of a conventional ceramic trap capable of shuttling an ion through a junction will also be detailed, and reveal the need for moving towards lithographically fabricated traps. Combined, these serve as a set of proof-of-principal experiments pointing to methods for designing and building large scale arrays of ion traps capable of constituting a quantum information processor.

As traps become smaller, electrical potentials on the electrodes have greater influence on the ion. This not only pertains to intentionally applied voltages, but also to deleterious noise sources, such as thermal Johnson noise and the more significant “patch potential” noise, which both cause motional heating of the ion. These problematic noise sources dovetail with my thesis research into trap miniaturization since their affects become more pronounced and impossible to ignore for small trap sizes.

Therefore characterizing them and investigating ways to suppress them have become an important component of my research. I will describe an experiment using a pair of movable needle electrodes to measure the ion heating rate corresponding to the harmonic frequency of the trap, the ion-electrode distance, and the electrode temperature. This information is used for characterizing the fluctuating potentials and exploring the possibility of suppressing motional heating by cooling the trap electrodes. This source of noise is also observed in other systems, and its characterization could potentially improve other precision experiments, such as those measuring deviations in the gravitational inverse square law with proximate masses.

CHAPTER 1

Introduction to trapped ion quantum computing

1.1 Trapped Ions

Ion traps have enjoyed a prominent position in atomic physics since their development by Wolfgang Paul [1] and Hans Dehmelt [2] in the 1950's and 1960's, for which they won the Nobel prize in 1989. They offer unprecedented levels of control over an atomic system by isolating single ions from their environment and allowing them to be interrogated with electromagnetic radiation. For this reason ion traps have been a very productive testbed, enabling such advances as laser cooling to the ground state of motion [3], performing precision measurements of atomic internal structure [4], and defining accurate and stable time and frequency standards [5]. In addition they are a leading candidate for quantum computing [6], which will motivate much of the work presented here.

There are two types of ion traps, the Paul trap and the Penning trap. Paul traps, also called RF traps, employ oscillating electric fields to create a time averaged potential well for the ion, with a potential minimum at either a point or along a line. In the case of a linear RF trap, additional static electric fields are used to confine the ions to single points along the line. The Penning trap uses a static magnetic field in conjunction with a static electric field to confine ions in circular orbits. This type of trap can be used in some of the same applications as the Paul trap, but for this thesis we will focus on developing Paul traps for quantum computing (QC) applications, as they are more practical for proposed large scale QC systems.

The aforementioned minimization of environmental influences from nearby material is unique to trapped ions and optically (and magnetically) trapped neutral atoms; single atoms confined in a material lattice, such as dopants in silicon, are exposed to the fields and phonons generated and contained by its host substrate. The energy depth of RF Paul traps further distinguishes them from optical neutral atom traps; with depths on the order of several to a hundred times room temperature, they can be a million times stronger than their neutral atom counterparts. This makes loading and storing single ions relatively easy, and furthermore allows for controlling the motion of an ion with electric fields, which is important for many quantum computing schemes.

1.2 Moore's law and classical computing

One of the motivations for building a quantum computer is the approaching computing power limitation for conventional microprocessors. Thus far, improvements in semiconductor processing have allowed classical computer speeds to increase exponentially for much of the last few decades, a trend popularly known as Moore's law. However, the technology advances that allow for smaller devices and denser chips, and thus faster computers, are expected to hit a fundamental limitation in the next few decades. In part this problem occurs once component sizes shrink to the point where quantum effects, which are an anathema to their deterministic nature, dominate the behavior of electrons in transistors. Electrons with wavelengths comparable to the size of their confining structure behave more like a quantum entity than a classical, point-like charged particle. When transistors become this small, on the order of 10 nanometers, electrons are able to tunnel across a transistor barrier whether or not a voltage is applied to the gate. At this point, regardless of whether photolithography can continue making smaller components, a major shift in computer engineering is necessary to continue increasing processor speed. Quantum computing is a fundamental shift because it takes advantage of quantum properties rather than trying to eliminate them. It could still use many of the industrial processing techniques for fab-

ricating the devices; several proposals (quantum dots, Josephson junctions [7]) look rather similar to current computer chips in that they are fabricated on semiconductor substrates and operated with electrical signals, albeit with exotic low temperature and precise control requirements. The hurdle that physicists in these fields are working on is to preserve the quantum nature of the device in the midst of its surrounding material, which can be a source of noise and decoherence. Interactions with phonons (often necessitating cooling the device to the sub-Kelvin level), impurities in the substrate, and even cosmic rays are a few of the noise sources that have to be contended with in these devices. Ion traps circumvent this issue by holding single atomic ion qubits in free space. At ultra high vacuum pressures, the interaction of the ion with its surroundings depends on collisions with the background gas (which can be made small in a good vacuum chamber) and noisy electrical fields from the surrounding electrodes (which can be mitigated with techniques discussed later).

It is important, however, that we not make too much out of the quantum computing motivation derived from the impending end of Moore's law. For one, the semiconductor industry and computer scientists continually find other strategies for making computers in practice faster to the user. These include greater vertical integration of CPUs, more efficient component distribution and advanced VLSI [8], and more efficient computing algorithms. Secondly, as will be discussed in more detail later in this section, only a few quantum algorithms have been discovered which exhibit a speedup over their classical counterparts. And finally, the technological hurdles of building a quantum computer are significant, and the territory of manipulating large entangled systems are an unexplored regime, so that one should be reasonably sober about making overly ambitious predictions. Nonetheless, the physics is interesting and much progress has been made in demonstrating proof-of-principal experiments that could lead to a practical implementation. Also, the growing interest in quantum simulations offers a useful application for a quantum computer without the stringent control requirements that for instance implementing Shor's algorithm would need.

1.3 Quantum Information

Richard Feynman [9] and David Deutsch [10] are generally credited for developing the idea of using the information stored in quantum states for computational purposes. They envisioned using these computers for simulating quantum systems; because such a system becomes exponentially larger and more complex with a linear increase in size (i.e. degrees of freedom), classical computers are impractical for simulating all but the simplest quantum problems. A quantum computer, however, could naturally store and process that information provided one could sufficiently prepare and manipulate its quantum states.

The field of theoretical quantum computing really exploded in 1994 when Peter Shor [11] discovered how to solve the problem of factoring a number more efficiently with a quantum computer. Using his algorithm, it was shown that the quantum version processing time would scale in order $(\log(N))^3$ [12] with the size N of the number being factored, whereas the best classical algorithm (the number field sieve [13]) scales exponentially worse, with order $\exp(\sqrt{\log N \log \log N})$. This result is important because much of cryptography is based on the computational difficulty of factoring large numbers. For instance, in a contest sponsored by RSA encryption, a 640 bit number was recently factored after approximately 30 2.2 GHz Opteron CPU years [14]. The power required to factor much larger numbers becomes prohibitive for classical computers, and serves as a motivation for designing a quantum computer. Shor's algorithm also inspired searches for other quantum algorithms, such as Grover's search algorithm which exhibits quadratic speedup over its classical search counterpart.

These algorithms would be considered impossible to implement if not for the discovery of quantum error correcting codes [15] which can correct for the inevitable environmental influences on a quantum system. These error correcting codes set a threshold level for fault tolerance; by limiting errors to below this threshold, a quantum algorithm can be reliably implemented. Of course, further reduction of error rates allows for a reduction in the amount of qubit resources needed for the computation. These are active areas of study; more efficient error correcting codes and quantum algorithms make actually constructing such a device more reasonable.

The goal of solving broader problems with a quantum computer remains an open question [16]. Until we know the relation between the BQP complexity class (bounded, quantum in polynomial time) and the NP Complete class (the class of problems which all non-deterministically polynomial problems can be reduced to) [12], we won't know whether a quantum computer can solve other problems which are computationally hard. For instance, the factoring problem is in the NP complexity class, but it is not NP complete, so it is not extensible to other hard problems. While the usefulness of a quantum computer is justifiable based solely on the factoring problem, it would have broader appeal if its usefulness could be extended to other hard computational problems.

1.4 General quantum computing requirements

The suitability of using a particular system for quantum computing is determined by how well it satisfies the DiVincenzo criteria [17]. These criteria require that the system ¹ uses a scalable architecture that can host a large number of qubits, ² the qubit state can be reliably initialized, ³ it has a long enough coherence time to perform many gate operations, ⁴ a universal set of quantum gates can be implemented, and ⁵ the state can be reliably detected. I will briefly discuss the last four requirements, but will spend the majority of this thesis presenting various proposals for satisfying the scalability condition using trapped ions.

Despite the above mentioned difficulties and obstacles, mathematicians, computer scientists, physicists, and engineers have been paying increasing attention to quantum computation as both an interesting way to study quantum mechanics and a potentially useful technology. There is no shortage of interesting experiments and practical applications that can emerge from quantum computing research. Already entanglement has been successfully put to use in building a more accurate atomic clock [18] and demonstrating a quantum cryptography architecture. Hopefully quantum computing will enjoy the same success as these related applications.

1.5 Quantum phenomena

While a classical bit can be one of two values at a time, typically denoted 0 or 1, quantum bits (qubits) can be in a superposition of 0 *and* 1 at the same time. This phenomenon allows a register of qubits to hold exponentially more information [12] than a register of classical bits. If we consider the case of two qubits, both in the state $\alpha|0\rangle + \beta|1\rangle$, the total state is $\alpha^2|00\rangle + \alpha\beta|01\rangle + \alpha\beta|10\rangle + \beta^2|11\rangle$. The information of these four states is stored in their amplitudes, and the quantum algorithm takes advantage of constructive and destructive interference to arrive at the correct answer. So in the end, whereas two classical bits would only be able to store a single state (say $|00\rangle$), the pair of quantum bits is able to store four states, an exponential increase with the number of bits. Since the amplitude is important in the computation, great care must be taken to initialize and maintain the qubit at the appropriate value. To compare, classical bits have threshold voltage values which define the state they are in, so that environmental fluctuations can be tolerated as long as they are not significant compared to the threshold. Qubits, however, are sensitive to certain sources of environmental noise, and the effect is directly propagated into the quantum computation.

Taking advantage of the parallelism available from having superpositions of states requires a key resource called entanglement, which is unique to a highly controlled quantum system. Entanglement refers to the correlation between two different systems, which in this thesis will be the internal states of an atom. If the combined system of states a and b is the total state $|1_a 0_b\rangle + |1_a 1_b\rangle$, we can see that states a and b are not dependent on each other, that is if we measure state a and we get 1, state b can still be either 0 or 1. Another way to see this is if we can factorize the total state; for the simple example above, we see that we can factor it into $|1_a\rangle(|0_b\rangle + |1_b\rangle)$, and so a and b are independent and not entangled. But what about $|0_a 0_b\rangle + |1_a 1_b\rangle$? This case cannot be factored, and we see that if we measure a to be 0, we know b has to also be zero, so it must be an entangled state. An interesting property of entanglement is that the correlations appear instantaneously; although in the last

example we do not know a priori whether both a and b are in 0 or 1, if we measure a to be 0, b has to be 0 as well. Entanglement operates without any intermediary particle or connecting force; two entangled particles are connected in such a way that correlations respond instantly over any distance. To create this initial entanglement however requires some common interaction; for the case of trapped ions, this is accomplished via common modes of motion and phonon interactions. This correlation also makes the qubit more sensitive to noise, as it gets propagated not just to the qubit that the noise acted on but also the other qubits it was entangled with. The strange phenomenon of entanglement is still being probed in experiments testing the fundamental nature of quantum mechanics.

1.6 What numbers are we really talking about?

Even given a structure for hosting a large array of ions, the technological and engineering hurdles for implementing a quantum computer are great. Assume that it would require 100 qubits to perform Shor's Factoring algorithm, and that each qubit needs 50 ions, with most of those being used for error correction. This 5000 ion array would need on the order of 50000 individually controlled DC electrodes. This number of separate input channels would be impossible to implement individually, given that it all must be done in vacuum, through UHV compatible connectors. For this reason, a quantum computer equivalent of VLSI would be required to handle the control circuitry just to move the ions around. Additionally, this number of ions would need a large number of lasers for cooling, detection, and gate operations. The precise control of these would have to be coordinated with the ion's motion in the trap, determined by the quasi-static electrodes. These lasers have to be aligned well enough on the ion, and maintain that alignment over the course of the computation, which would be a straightforward task for a small experiment, but would be impossible for a large array of 5000 ions. Some feedback to computer controlled motors on the mirrors would therefore be necessary. Based on these considerations, one can see that a great deal of infrastructure, including a very powerful classical computer, would

be required to run a useful quantum computer. Smaller algorithms using fewer ions could still perform useful calculations and provide insight into issues associated with larger ion trap arrays.

1.7 Atomic physics of trapped ion quantum computing

The qubit of an ion is based on the spin state of its valence electron and its nucleus, which are the same states that underlie atomic clocks. Depending on whether the spin of the electron is aligned with or against the nuclear spin determines the $|0\rangle$ and $|1\rangle$ states of the qubit. Detection is accomplished by resonantly exciting one of the qubit states and collecting the fluorescence when it decays. The state is initialized also through resonant excitations in which the ion is left in an off-resonant state after it decays. Both of these processes will be described in more detail in chapter 2. The length of time that a qubit remains in a prepared state (whether it is $|0\rangle$, $|0\rangle + |1\rangle$, or any other superposition) is called the coherence time. Decoherence occurs when the qubit state changes due to uncontrolled interactions with its environment, which include spontaneous emission, fluctuating electric fields, and fluctuating magnetic fields, to name a few. A quantum computer is limited in the number of qubit gates it can perform by the time it takes for decoherence errors to dominate.

The previous paragraph describes how single ions can store quantum information which can be manipulated and read out, but also crucial is the ability to interact and perform gates. Ions have an important advantage over some other proposed QC systems, such as neutral atoms, in that the strength of these interactions is much higher in ions due to Coulomb repulsion. Several groups have demonstrated gate operations [19, 20] in which the coupling of the ion's motion to its neighbor has been used to implement a controlled not (CNOT) gate, which is similar to an XOR logic operation. The truth table for a CNOT gate is shown in table 1.7. The CNOT gate along with a single qubit gate which rotates the state of the ion (changes the relative degree of $|0\rangle$ and $|1\rangle$) provides a universal set of operations in which any logic operation can be performed. Since the aforementioned experiment, other improved

00	→	00
01	→	01
10	→	11
11	→	10

Table 1.1: A CNOT gate truth table

gates equivalent to the CNOT gate have been demonstrated which have used spin dependent forces for entangling operations [21, 22].

Typical ions used for trapped ion quantum computing have hydrogen-like structures when singly ionized, i.e. they have one valence level electron with a $^2S_{1/2}$ ground state. This includes the alkali earth metals (e.g. Be, Mg, Ca, Ba) and the IIB transition metals with full D shells (e.g. Zn, Cd, Hg). These atomic species have a range of transition frequencies used for laser cooling and other qubit operations; the properties of the internal structure, such as the linewidth and location of excited states, determine the ion's suitability for quantum computing. There are two basic types of ion qubits: a hyperfine qubit, which uses the ground state hyperfine structure to store quantum information, and an optical qubit, which uses the ground state and a low lying D state (lower than the excited P state) as its qubit. The hyperfine qubit has the advantage of typically long lifetimes (on the order of thousands of years), which allows for theoretically long coherence times, or equivalently low spontaneous emission error rates during qubit storage (this is not the dominant source of error, however, so it is not a limiting factor). Additionally, these qubits do not have low lying D states which must be cleaned up, and so require relatively few lasers. The downside to using hyperfine qubits is that they often require UV or near UV wavelengths for detection and Raman transitions. The difficulty of generating this laser light can balance out some of the aforementioned advantages. From now on I will discuss our experiments in the context of the cadmium ions which we use. Many of the same principles which are discussed can be applied to other hyperfine qubits, albeit with different physical constants.

CHAPTER 2

The cadmium qubit

The choice of using cadmium as our qubit was motivated by its favorable atomic properties. It has a large ground state hyperfine splitting which allows for near perfect detection efficiency ($\sim 99.9\%$) and state initialization ($\sim 99.99\%$). Spontaneous emission from the $|\uparrow\rangle$ state is negligible, as it has an extremely long lifetime of thousands of years. By choosing the qubits to be the magnetically insensitive (to first order) $m_f = 0$ states, fluctuations of external magnetic fields have minimal effect. The trade-off for these benefits, as mentioned previously, is the UV (214.5 and 230 nm) light necessary for detection, initialization, photoionization, and stimulated Raman transitions.

2.1 State detection and initialization

The state of the valence electron is detected by applying a σ^+ polarized laser beam resonant between $|\downarrow\rangle$ (we also call this $|1\rangle$ or the bright state) and the excited state $^2P_{3/2}$ ($F=2$), such that the ion can only fall back into the initial $|\downarrow\rangle$ state (see figure 2.1). The photons emitted when the electron decays to the ground state are collected, and the state is determined by the absence or presence of photon counts. If the ion is in $|\uparrow\rangle$ (also $|0\rangle$ or the dark state), the laser is 13.7 GHz off resonance from the excited state transition, and therefore is unlikely to excite a transition. The maximum fidelity that we can achieve in light of this error mechanism is $F = 1 - \frac{4}{9}\gamma/2\Delta$, where $4/9$ is due to the Clebsch-Gordon coefficients from the $|2, 2\rangle$ decay channels, γ is the 60 MHz natural linewidth, and Δ is the 13.7 GHz detuning [23]. To maximize our

detection fidelity with respect to background scattering, we apply a low power beam ($s_0 = I/I_{sat} \sim .1$, $I_{sat} = \pi\gamma\hbar c/(\lambda^3) = 7.9 \mu\text{W}/\text{mm}^2$); when $s_0 \gg 1$, the fluorescence no longer increases with intensity, but the spurious background counts due to tails of the beam scattering off the trap electrodes does increase linearly with power. We also tune the beam nearly at the resonance peak so that we get the maximum ion fluorescence for a given background scattering. We choose our detection time such that it is long enough to distinguish from the background yet balance the competing problem that the longer we apply it the more likely we are to off resonantly populate the $|\downarrow\rangle$ state from the $|\uparrow\rangle$ state. Given these competing factors we use a $200 \mu\text{s}$ laser pulse which is well below the saturation intensity of Cd, during which we collect an average of 12 photons in the bright state and 0 photons in the dark state on a Hamamatsu 86240-01 photomultiplier tube (PMT) (see figure 2.2). The PMT has a detection efficiency of 20%, which combined with a solid angle collection of about 5% allows us to collect about .3% of all photons emitted, once other loss mechanisms are considered. By setting a discrimination level at two photons, we can experimentally discriminate between the dark and bright states with 99.7% fidelity.

The state of the ion qubit is initialized by applying a laser beam resonant between the $|\downarrow\rangle$ state and an excited state (see figure 2.1). When the ion decays from the excited state it returns with 1/3 probability to the $|\downarrow\rangle$ state and is excited again, or it decays into the $|\uparrow\rangle$ state with 2/3 probability, where it stays, since the laser beam is not resonant with the transition between $|\uparrow\rangle$ and the excited state. If we are well below saturation, the number of excitations it can make in time T is $\gamma_0 s T/2$, where $s = I/I_0$ is the saturation parameter, and γ_0 is the natural linewidth of 60 MHz. For a saturation parameter of .1 and a pulse time of $5 \mu\text{s}$, we would excite the ion 150 times, where each time would have a 2/3 probability of being initialized into the $|\uparrow\rangle$ state. The initialization fidelity is limited by the probability of off resonant pumping from the dark state back to the bright state, so the theoretical best fidelity we can achieve is 99.99%.

2.2 Qubit rotations and quantum gates

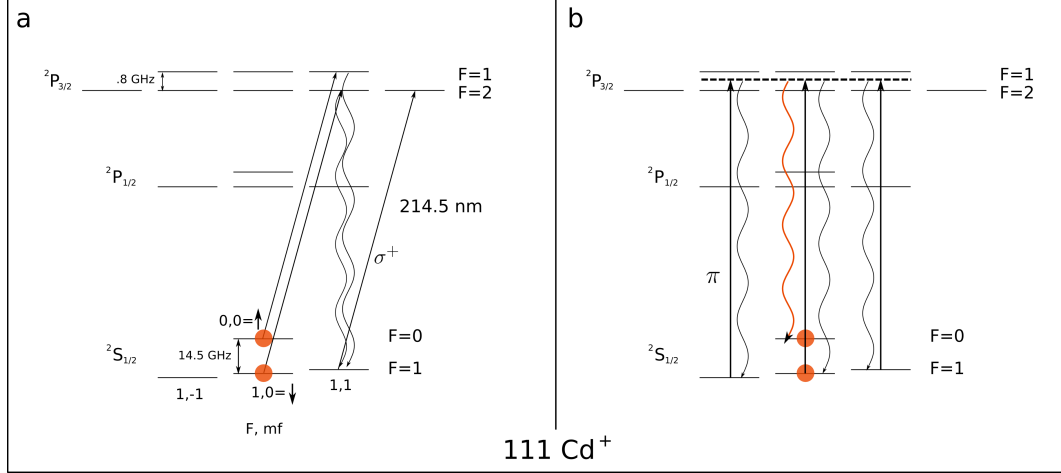


Figure 2.1: Detection and initialization of the $^{111}\text{Cd}^+$ qubit: Part **a** shows the energy diagram for the detection transition; by applying σ^+ laser radiation resonant between the $|\downarrow\rangle$ state and the excited $^2P_{3/2}$ ($F=2$) state we can detect the fluorescence from the cycling transition. Part **b** shows how an ion can be initialized into the $|\uparrow\rangle$ state. By applying π polarized light resonant between the $|\downarrow\rangle$ and between the $^2P_{3/2}$ ($F=1$) and ($F=2$) states the ion will eventually fall into the $|\uparrow\rangle$ state via the orange line transition and stay there.

The relative populations of the qubit states is important for storing quantum information, as discussed with regard to superpositions in section 1.5. Changing the amplitudes of these superpositions is called a qubit rotation. By describing the state of an ion as $\cos(\theta) |0\rangle + \sin(\theta) |1\rangle$, we can see that, for instance, a $\pi/2$ rotation would result in the amplitude of the $|0\rangle$ and $|1\rangle$ states being switched. For the work done for this thesis, we will be mostly concerned with single qubit rotations, primarily via carrier stimulated Raman transitions. The following derivations and formalism can be found in a variety of texts; here we follow a similar derivation to that in [6]. We will also discuss coupling the spin state of the ion to the motion, focusing mostly on sideband thermometry techniques, but also briefly discussing motional gates.

2.2.1 The ion's motion

As will be discussed in greater detail in chapter 3, an ion's motion in the trap has both a low frequency (~ 1 MHz) harmonic (or secular) component and a higher

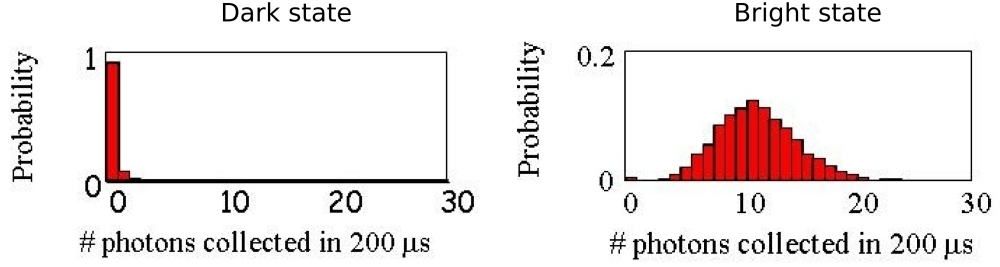


Figure 2.2: Detection statistics for the $^{111}\text{Cd}^+$ qubit in the dark and bright states: This figure shows the collected photon statistics for a $200\ \mu\text{s}$ time period on a PMT. In part **a** we see the dark state counts, partially due to background scattering, but to a larger extent due to the probability of off-resonant excitation out of the dark state, and so is a convolution of Poissonian probabilities for different pump out times. Part **b** shows the bright state counts, which is a standard Poissonian distribution. By setting a discrimination level of 2 photons, a detection fidelity of 99.7% is achieved.

frequency ($\sim 50\ \text{MHz}$) micromotion component. Since interactions are performed on resonance with this lower frequency harmonic part, we ignore the micromotion part in our quantum treatment of motion. We also only consider one direction of motion; a linear trap which tightly confines the ion in two dimensions makes using the third, less tightly confined dimension, available for motional coupling of the laser beam, provided the \mathbf{k} vector of the laser has a component along this direction. The Hamiltonian for the harmonic motion is then $H_{\text{motion}} = \hbar\omega_i(1/2 + \hat{n}_i)$, $i \in \{x, y, z\}$, where $\hat{n}_i = a_i^\dagger a_i$ and ω_i is the secular motion. For a particular independent direction \hat{z} , the center of mass motion operator is $z = z_0(a + a^\dagger)$, where $z_0 = (\hbar/2m\omega_z)^{1/2}$ is the spread of the ground state wave function. For a Cd ion in an $\omega_z/2\pi = 1\ \text{MHz}$ trap, $z_0 = 6.7\ \text{nm}$. An ion can occupy a distribution of motional levels, so the state in the Schrödinger picture is written as:

$$\Psi_{\text{motion}} = \sum_{n=0}^{\infty} C_n e^{-in\omega_i t} |n\rangle \quad (2.1)$$

2.2.2 The ion's internal states

The $|\uparrow\rangle$ and $|\downarrow\rangle$ qubits of the ion can be treated as a spin $1/2$ magnetic moment in

a magnetic field [24], a general formulation which can be used to describe other two level systems as well. Given two levels $|\uparrow\rangle$ and $|\downarrow\rangle$ which are separated by $\hbar\omega_0$, the interaction Hamiltonian is:

$$H_{int} = \frac{\hbar\omega_0}{2}\hat{\sigma}_z = \frac{\hbar\omega_0}{2} \begin{bmatrix} 1 & 0 \\ 0 & -1 \end{bmatrix} \quad (2.2)$$

and its corresponding wavefunction:

$$\Psi_{int} = C_{\downarrow}e^{i\omega_0 t/2}|\downarrow\rangle + C_{\uparrow}e^{-i\omega_0 t/2}|\uparrow\rangle \quad (2.3)$$

where $\hat{\sigma}_z$ is the Pauli spin matrix, $|\uparrow\rangle = \begin{pmatrix} 1 \\ 0 \end{pmatrix}$, and $|\downarrow\rangle = \begin{pmatrix} 0 \\ 1 \end{pmatrix}$. Combined with the motional Hamiltonian described above, the total unperturbed Hamiltonian H_0 (dropping the ground state motional energy) is:

$$H_0 = \frac{\hbar\omega_0}{2}\hat{\sigma}_z + \hbar\omega_z\hat{n} \quad (2.4)$$

Since we are interrogating trapped ions with microwaves and lasers, we are concerned with the interaction Hamiltonian from coupling internal levels with electric and magnetic fields. In this derivation we will use the magnetic dipole transition between $|\uparrow\rangle$ and $|\downarrow\rangle$, although this can be easily adapted in the case of an electric dipole transition. The interaction Hamiltonian is:

$$H_I = -\boldsymbol{\mu} \cdot \mathbf{B} \quad (2.5)$$

$$= \frac{\hbar\Omega}{2}(\sigma_+e^{i(\mathbf{k}\cdot\mathbf{r}-\omega t+\phi)} + \sigma_-e^{-i(\mathbf{k}\cdot\mathbf{r}-\omega t+\phi)}) \quad (2.6)$$

where $\boldsymbol{\mu} = \mu_m\hat{\sigma}/2$ is the magnetic dipole operator and $\mathbf{B} = B_x\hat{x}\cos(\mathbf{k}\cdot\mathbf{r}-\omega t+\phi)$ is the magnetic field applied, which propagates in the \hat{r} direction and is polarized in \hat{x} . This Hamiltonian is written more suggestively in the second line as the Rabi frequency $\Omega = -\mu_m B_x/2\hbar$ times the oscillating portion. For the case of an electric dipole transition, the interaction Hamiltonian would be $-\boldsymbol{\mu}_d\cdot\mathbf{E}$, giving $\Omega = -\mu_d E/2\hbar$.

In the interaction picture we can treat the motional and internal states together. We define the Hamiltonian $H_0 = H_{int} + H_{motion}$ and the interaction Hamiltonian as above so that we can eliminate the high frequency $(\omega + \omega_0)$ terms using the rotating wave approximation. We are then left with the wave function:

$$\Psi = \sum_{n=0}^{\infty} C_{\uparrow,n}(t) |\uparrow, n\rangle + C_{\downarrow,n}(t) |\downarrow, n\rangle \quad (2.7)$$

with the corresponding interaction picture Hamiltonian [24]:

$$H'_I = e^{iH_0 t/\hbar} H_I e^{-iH_0 t/\hbar} \quad (2.8)$$

$$= \frac{\hbar\Omega}{2} \left(\sigma_+ \exp(i(\eta(ae^{-i\omega_z t} + a^\dagger e^{i\omega_z t}) - \delta t + \phi)) + h.c. \right) \quad (2.9)$$

where $\eta = k_z z_0 = (\mathbf{k} \cdot \hat{z}) z_0$ is the Lamb-Dicke parameter and $\delta = \omega - \omega_0$. As before, the \hat{z} direction is along the weak axis of the trap. The Lamb-Dicke parameter η is a measure of the spread of the ion's ground state wave function compared to the wavelength of light interrogating it.

Here we will consider only resonant transitions, where $\delta = \omega_z(n' - n)$. The population in the $|\uparrow\rangle$ and $|\downarrow\rangle$ levels will then evolve according to:

$$\dot{C}_{\uparrow,n'} = -i^{1+|n'-n|} e^{i\phi} \frac{\Omega_{n',n}}{2} C_{\downarrow,n} \quad (2.10)$$

$$\dot{C}_{\downarrow,n} = -i^{1-|n'-n|} e^{-i\phi} \frac{\Omega_{n',n}}{2} C_{\uparrow,n'} \quad (2.11)$$

where

$$\Omega_{n',n} = \Omega |\langle n' | e^{i\eta(a+a^\dagger)} | n \rangle| \quad (2.12)$$

$$= \Omega e^{-\eta^2/2} \sqrt{\frac{n_{<}!}{n_{>}!}} \eta^{|n'-n|} L_{n_{<}}^{|n'-n|}(\eta^2) \quad (2.13)$$

$$= D_{n',n} \Omega \quad (2.14)$$

Here L_n^a is the generalized Laguerre polynomial and $n_{<}$ is the lesser of n' and n (and visa versa). In the Lamb-Dicke limit ($\eta n^2 \ll 1$), $\Omega_{n,n} = \Omega$, $\Omega_{n,n-1} = \Omega\eta\sqrt{n}$, $\Omega_{n,n+1} =$

$\Omega\eta\sqrt{n+1}$. The $D_{n',n}$ term is the Debye-Waller factor, which is more familiar in the context of attenuation of X-ray scattering due to dephasing as a result of thermal motion. The same principal applies here, however, as ion motion results in a decrease of the Rabi frequency due to dephasing. Now we can simplify equation 2.10 to:

$$\begin{aligned}\Psi(t) &= \begin{bmatrix} C_{\uparrow,n'}(t) \\ C_{\downarrow,n}(t) \end{bmatrix} \\ &= \begin{bmatrix} \cos(\Omega_{n',n}t/2) & -ie^{i(\phi+\frac{\pi}{2}|n'-n|)} \sin(\Omega_{n',n}t/2) \\ -ie^{-i(\phi+\frac{\pi}{2}|n'-n|)} \sin(\Omega_{n',n}t/2) & \cos(\Omega_{n',n}t/2) \end{bmatrix} \Psi(0)\end{aligned}\quad (2.15)$$

It is apparent from this derivation that by tuning our laser to $\omega_0 + \omega_z(n - n')$ we can transition between any state $|\uparrow, n'\rangle$ to $|\downarrow, n\rangle$. We can also see how to measure the heating of the ion from measuring the transition frequency. In the case of the GaAs trap we measure the suppression of the spin flip from $|\uparrow\rangle$ to $|\downarrow\rangle$ due to temperature, and in the needle trap we measure the heating rate by looking at the asymmetry in the spin flip rate depending on whether $n \rightarrow n + 1$ or $n \rightarrow n - 1$.

2.2.3 Microwave transitions

In the Lamb-Dicke limit, the Debye-Waller factor can be calculated to first order (similar to the Rabi frequency) as $D_{n,n} = 1$ (the carrier transition, since n is constant), $D_{n+1,n} = \eta\sqrt{n+1}$ (the first red sideband), and $D_{n-1,n} = \eta\sqrt{n}$ (the first blue sideband). As seen here, the sideband strengths go to zero as the Lamb-Dicke parameter goes to zero. A strong sideband is necessary for changing the motional state of the ion, for instance during a sideband cooling experiment or an entanglement experiment. In the case of microwave transitions, where the radiation frequency corresponds to the hyperfine splitting, $k = 2\pi \cdot 14.5 \times 10^9 / c$, the Lamb-Dicke parameter will also be small. Considering a Cd ion in an $\omega_z/2\pi = 1$ MHz trap gives $\eta = 2 \times 10^{-6}$, corresponding to a very weak transition. Physically this corresponds to the microwave photons not having enough momentum to excite the motion of the ion.

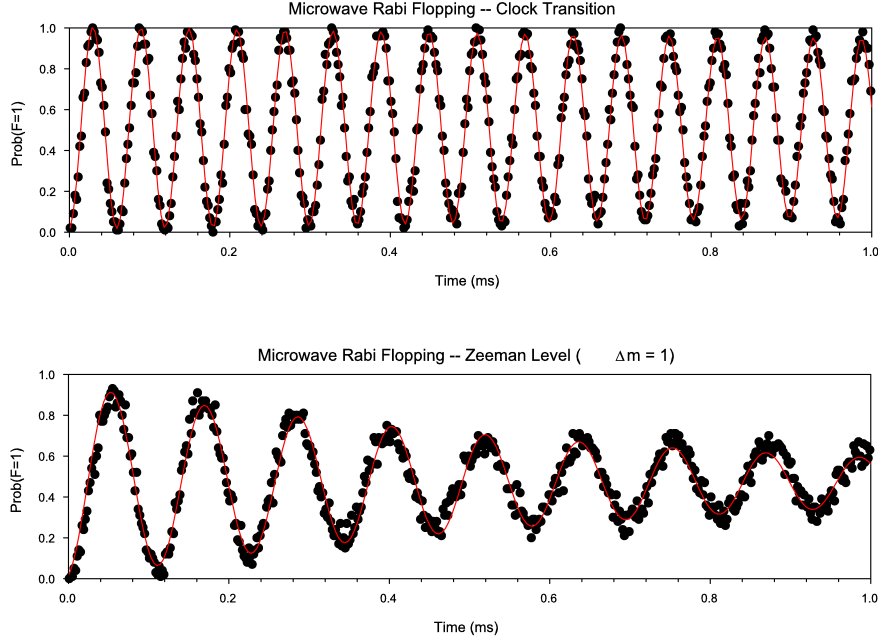
A strong transition would therefore require a magnetic dipole transition with higher, optical frequencies, and since $^{111}\text{Cd}^+$ does not have such a magnetic dipole transition, we can use microwaves only for changing the spin state of the ion, and not its motional state. An example of this is seen in figure 2.3, where Rabi flopping on the carrier transition was performed with microwaves. For this experiment a microwave horn with 1 watt of amplified power from a signal generator was used to drive the transition. Besides not being able to induce motional transitions, microwaves also have the disadvantage that they cannot be focused down to individual ions, as a laser can. The transitions in the figure occurred between the $|0,0\rangle \leftrightarrow |1,0\rangle$ states (top graph) and the $|0,0\rangle \leftrightarrow |1,1\rangle$ states (bottom graph). The $|0,0\rangle \leftrightarrow |1,0\rangle$ transition is called the clock transition because it is between two magnetic field insensitive qubits (to first order), so decoherence due to dephasing does not cause the signal to decay, as in the magnetically sensitive $|0,0\rangle \leftrightarrow |1,1\rangle$ transition.

In the experiments discussed in this thesis, the primary concern is temperature measurement. For traps in which the heating rate is low enough and sideband cooling can be used to bring the ion to its ground state of motion, we are able to measure the heating rate by measuring the sideband asymmetry after different delay times. For the case of a hot trap, like the GaAs trap, in which we cannot cool to the ground state, we measure the suppression of the Raman transition rate due to the Debye-Waller factor as a result of the temperature increase of the ion. This requires using the next order term of the carrier, $D_{n,n} = 1 - 2\eta^2$.

2.2.4 Stimulated Raman Transitions

To induce strong transitions on the motional sidebands of the radiation field discussed above, we use two photon stimulated Raman transitions (SRT). This technique achieves a higher field gradient and subsequently stronger sideband transitions by coupling the qubits to the excited $^2P_{3/2}$ state (see figure 2.4).

These electric dipole transitions are detuned from the excited state by Δ and have electric dipole operators μ_1 and μ_2 . The laser beams $\mathbf{E}_1(\mathbf{r}, t) = \hat{\epsilon}_1 E_1 \cos(\mathbf{k}_1 \cdot \mathbf{r} -$



*Rabi frequency is slower for the Zeeman level transition due to the polarization of the microwave.

Figure 2.3: Rabi flopping on the carrier transition using microwaves: In this figure, the top graph shows Rabi flopping on the carrier transition between the $|0,0\rangle$ and $|1,0\rangle$ states, and the bottom graph between the $|0,0\rangle$ and $|1,1\rangle$ states. The top graph shows little decay compared to the bottom one because the states are magnetic field insensitive to first order, whereas the $|1,1\rangle$ state fluctuates as $\delta\nu = 1.4 \text{ MHz/G } \delta B$. This magnetic field fluctuation could come from an external source, but more likely comes from fluctuations in the Helmholtz magnetic field coils that are used to define the quantization axis \hat{z} .

$\omega_1 t + \phi_1)$ and $\mathbf{E}_2(\mathbf{r}, t) = \hat{\epsilon}_2 E_2 \cos(\mathbf{k}_2 \cdot \mathbf{r} - \omega_2 t + \phi_2)$, where $\omega_2 - \omega_1 = \omega_{HF} + \Delta n \omega_z$. Ideally the beams would be co-propagating, with the $\Delta \vec{k}$ along the trap axis, so as to maximize the Lamb-Dicke parameter. This however is not possible with many of our ion trap geometries, so we use either a 90° or 70° co-propagating geometry, from both sides (see figure 2.5). Therefore $\Delta \vec{k} = \vec{k}_1 - \vec{k}_2$ ranges from $\sqrt{2}k$ to $1.1k$. For the 90° geometry in $^{111}\text{Cd}^+$, $\eta = \Delta k_z z_0 = \frac{700}{\sqrt{\omega_z}}$. For $\omega_z/2\pi = 1 \text{ MHz}$, $\eta = .28$.

We can calculate the new Hamiltonian and Raman transition rate similarly to the

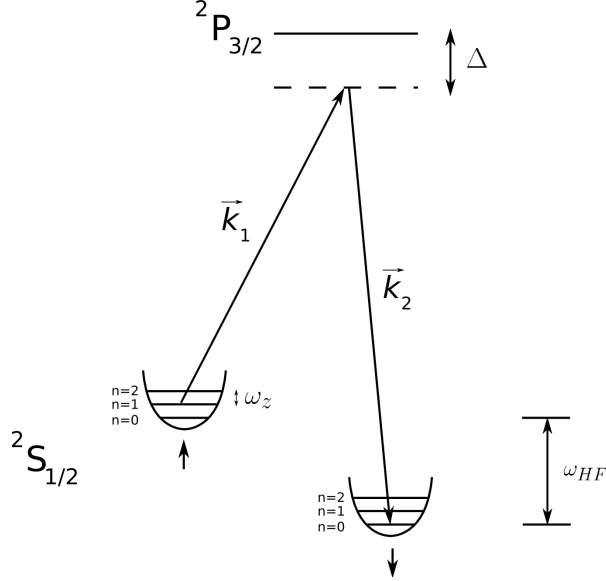


Figure 2.4: Raman transition diagram: This diagram shows Raman transitions between different motional levels, in particular the blue sideband transition which couples the $|\uparrow, 1\rangle$ and $|\downarrow, 0\rangle$ states.

way we did for microwaves. Our new interaction Hamiltonian looks like

$$H_I = -\boldsymbol{\mu}_d \cdot (\mathbf{E}_1 + \mathbf{E}_2) \quad (2.17)$$

$$= -\frac{\hbar}{2} \left(g_1 e^{i(\mathbf{k}_1 \cdot \mathbf{x} - \omega_1 t + \phi_1)} + g_2 e^{i(\mathbf{k}_2 \cdot \mathbf{x} - \omega_2 t + \phi_2)} \right) \quad (2.18)$$

where $g_{1,2} = \frac{\mathbf{E}_{1,2} \cdot \boldsymbol{\mu}_d}{2\hbar}$ is the electric dipole coupling strength corresponding to each beam. The details of this derivation can be found in [6], but in general it involves making the rotating wave approximation and then adiabatically eliminating the excited state. This is allowed because the Raman beams are far detuned from the excited state, so that the excited state population is always small. The transitions are also AC stark shifted, by an amount proportional to $g_1^2/2\Delta$ and $g_2^2/2\Delta$. If these are different, the transition frequencies must be tuned to the Stark shifted resonance. The generalized Rabi frequency is:

$$\Omega_{n,n'} = \frac{g_1^* g_2}{2\Delta} \langle n | e^{i\eta(\hat{a} + \hat{a}^\dagger)} | n' \rangle \quad (2.19)$$

Figure 2.5 shows that the Raman beam traveling parallel to the quantization

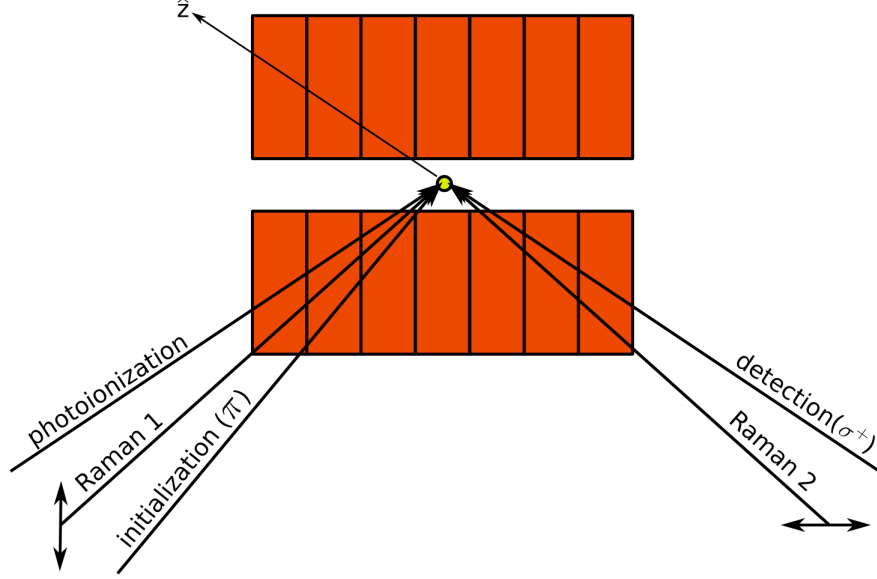


Figure 2.5: Schematic of the laser beams used in the detection, initialization, and motional coupling of an ion: This schematic shows the various laser beams used in the detection, initialization, and Raman transitions of an ion. The \hat{z} direction here corresponds not to the trap axis but the the quantization axis, as defined by magnetic field coils.

axis set by the external \vec{B} field is \hat{x} polarized, whereas the other Raman beam is \hat{y} polarized. It is necessary to use circularly polarized light, because there is no excited state with $m_f = 0$ which couples to both $|\uparrow\rangle$ and $|\downarrow\rangle$. Also, from the figure we see that the Clebsch-Gordan coefficients have a sign difference for the σ^- transition compared to the σ^+ transition. Since the transition rate depends on the product of E_1 and E_2^* , we need to chose the polarization such that $\frac{1}{3}E_{\sigma^+,1}E_{\sigma^+,2}^* - \frac{1}{3}E_{\sigma^-,1}E_{\sigma^-,2}^* \neq 0$, where the $\pm\frac{1}{3}$ correspond to the Clebsch-Gordan coefficients. Therefore we need to introduce a π phase shift in one of the beams so that the amplitudes add rather than cancel. This is accomplished by rotating the beam parallel to the quantization axis to have a \hat{x} polarization. Finally, we also see that since the absorbed photon has the same angular momentum as the emitted one, the total angular momentum is conserved and $\Delta m_f = 0$.

In addition to the AC Stark shift mentioned above, other decoherence mechanisms limit the theoretical performance of our qubit. The “theoretical” qualifier is used here because ultimately our qubit is sensitive to phase fluctuations, and without an

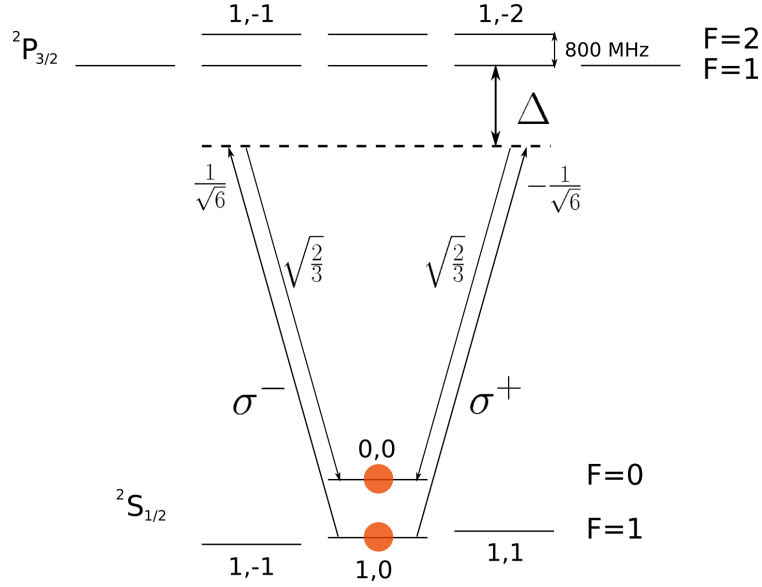


Figure 2.6: Energy level diagram of Raman transitions and Clebsch-Gordan coefficients: This energy level diagram shows the Raman transitions and corresponding Clebsch-Gordan coefficients. It is necessary to rotate the polarization of one of the beams so that the transitions do not cancel out.

atomic clock to lock our laser to, these phase fluctuations present more of a practical problem than strict atomic physics limitations of the decoherence rate. Nonetheless, it is important to realize the theoretical limitations of the Cd qubit. With regards to Raman transitions (initialization and detection fidelities were discussed previously in 2.1), the amount of errors due to spontaneous emission (γ_p) from the briefly populated excited state can be parametrized by the ratio γ_p/Ω ; in other words, the probability of a state destroying spontaneous emission divided by the time necessary to make a spin flip. In the limit of $\Delta \gg \gamma_0$ (which is always the case), the spontaneous emission rate is $\gamma_p = s\gamma^3/(4\Delta^2)$. The Raman transition rate is $\Omega = s\gamma^2/\Delta$. Combining these two equations $\gamma_p/\Omega = \gamma/(4\Delta)$ reveals that the error rate can be decreased by increasing the detuning. For cadmium, this is restricted by the fact that the detuning cannot be increased without bound, since the Raman transition rate will become significantly reduced as the transition begins coupling to the $^2P_{1/2}$ manifold which is 74 THz below the $^2P_{3/2}$ manifold. As this detuning grows, the time for a spin flip increases, during which time other errors can become significant. This could be counteracted

by increasing the intensity of the laser, but for cadmium we are already using all the power available from our laser.

Recent work has also shown that not all spontaneous emission is equal [25]. Instead it can be distinguished into the internal state preserving Rayleigh scattering, and the state destroying Raman inelastic scattering. The case where the detuning from the excited state is much larger than the fine structure splitting is analyzed ($\Delta \gg \Delta_{FS}$), and it is shown that in this regime the transitions from coupling to the two excited state manifolds results in destructive interference of Raman scattering compared to Rayleigh scattering. So while the overall spontaneous emission rate scales as $1/\Delta^2$, the Raman scattering rate scales as $1/\Delta^4$.

2.2.5 Laser cooling

The idea of using lasers to cool an atom was originally proposed in 1975 by Wineland and Dehmelt for ions in a Penning trap and independently by Hänsch and Schawlow for neutral atoms in a gas. Wineland demonstrated the first radiation-pressure cooling of any species below ambient temperature in 1978 [26, 27], and since then the technique of laser cooling has been extended to a broad range of atomic species.

The idea of Doppler laser cooling is based on the principal of resonant absorption and Doppler shifting; when an ion (or other particle, for that matter) is moving towards a laser, the frequency of light it sees is shifted up in frequency. If the laser is slightly below a resonance transition for this particle, the Doppler shift will cause the particle to absorb more photons, which it then re-emits isotropically. The number of photons scattered from an atom with linewidth γ_0 at a saturation parameter s_0 and detuning δ is $\gamma_p = \frac{s_0/2}{1+s_0+(2\delta/\gamma_0)^2}$ [28]. An ion moving away from the direction of the laser, however, is Doppler shifted down, and so it absorbs fewer photons. The preferential absorption of photons moving towards it imparts a momentum on the ion which causes it to slow down, hence the name radiation-pressure cooling. The limit

to this cooling rate is given by

$$k_B T_D = \frac{\hbar \gamma_0}{2} = \hbar \omega \bar{n}_D \quad (2.20)$$

or $\bar{n}_D = \gamma_0/2\omega$. For cadmium in a trap with a 1 MHz secular frequency, $\bar{n}_D = 30$ quanta, or 1 mK. The trap geometry also plays a role in that the laser only Doppler cools in one direction, but as long as the laser beam is not perpendicular to a particular principal axis of the trap (see chapter 3), the motion in the other directions will be coupled and a single laser can cool all three directions.

To be within the Lamb-Dicke limit the ion must be further cooled using Raman sideband cooling. In this technique, an ion is first initialized in the $|\uparrow\rangle$ state. A blue Raman pulse is applied to flip the ion into the $|\downarrow\rangle$ state and change its motional state from n to $n-1$. Then the ion is optically pumped on the carrier transition back to the $|\uparrow\rangle$ state, and the process is repeated. This process can leave the ion in an average motional state $\bar{n} \ll 1$ [29].

2.2.6 Thermometry

An ion's motion is subject to a variety of uncontrolled influences, the most prominent being fluctuating electric fields on the nearby electrodes. While the source and importance of this anomalous heating will be discussed in greater detail in chapter 8, measuring the temperature and heating rate of an ion in a particular trap is an important experimental technique. The sideband thermometry method for measuring the heating rate requires cooling to close to $\bar{n} = 1$ and measuring the asymmetry in the red and blue sideband Raman transitions. The probability of making a red or

blue sideband transition to the $|\downarrow\rangle$ state is:

$$P_{rsb}(\downarrow) = \sum_{n=0}^{\infty} P_n \sin^2(\Omega_{n,n-1}t/2) \quad (2.21)$$

$$P_{bsb}(\downarrow) = \sum_{n=1}^{\infty} P_n \sin^2(\Omega_{n,n+1}t/2) \quad (2.22)$$

$$= \sum_{n=0}^{\infty} P_{n+1} \sin^2(\Omega_{n-1,n}t/2) \quad (2.23)$$

$$= \frac{\bar{n}}{1 + \bar{n}} \sum_{n=0}^{\infty} P_n \sin^2(\Omega_{n-1,n}t/2) \quad (2.24)$$

where the probability of being in the n th vibrational mode for a thermal state (Maxwell-Boltzmann distribution) with average vibrational level \bar{n} is $P_n = (\frac{\bar{n}}{1+\bar{n}})^n \frac{1}{1+\bar{n}}$. Since $\Omega_{n,n-1} = \Omega_{n-1,n}$, we can take the ratio of these to get:

$$\frac{P_{bsb}}{P_{rsb}} = r = \frac{\bar{n}}{1 + \bar{n}} \rightarrow \bar{n} = \frac{r}{1 - r} \quad (2.25)$$

The ratio r can be calculated after any time duration that the Raman beams are applied. A typical frequency scan can be seen in figure 2.7, showing the probability of being in the bright state. The ratio r is calculated by taking the ratio of the peak on the left to the peak on the right, from which \bar{n} can be calculated.

The heating rate in this trap is calculated by cooling the ion to near the ground state with Raman sideband cooling and then measuring the sideband asymmetry after different delay times without cooling. As mentioned above, another technique is used when calculating the temperature in the GaAs trap. This is necessary because the heating rate is so high in the trap and the ion cannot be cooled to near the ground state, so the sideband asymmetry is insignificant. Instead the suppression of the Raman carrier transition due to increasing temperature is measured. More details about this can be found in chapter 6.

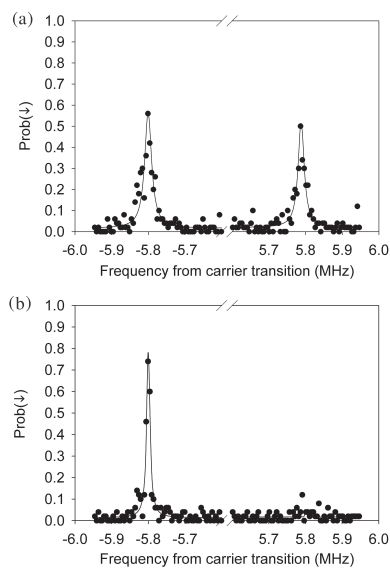


Figure 2.7: These graphs show Raman spectra which illustrate the sideband asymmetry for different \bar{n} . Both were taken in a $\omega_z/2\pi = 5.8$ MHz trap and show the probability of being in the $|\uparrow\rangle$ state. Part **a** corresponds to the temperature of the ion after being cooled to $\bar{n} = 5(3)$. Part **b** corresponds to $\bar{n} = .03(2)$.

CHAPTER 3

Ion trapping fundamentals

3.1 The ponderomotive potential

The technique of trapping ions using electric fields is based on the idea of creating a *time averaged* potential with oscillating electric fields, a method pioneered by Wolfgang Paul [1] for which he won the Nobel Prize in 1989. It is readily apparent that one cannot use static fields to contain an ion at a single position in space; from Gauss' law in free space, we can see that any field obeying Laplace's equations (such as an electric field) cannot have a point at which all of the field lines converge. This is equivalent to Earnshaw's theorem which states that such a field can never have a minimum in all directions, but instead gives rise to potential saddle points which have trapping and anti-trapping potentials in different directions for a snapshot in time. Oscillating fields, however, give rise to a pseudo-force called the ponderomotive force, constituting a harmonic trap for the ion with a characteristic frequency called the secular frequency. In the following sections we will show that this trap can be described as $\Psi(x, y, z) = \frac{1}{2}m(\omega_x^2 x^2 + \omega_y^2 y^2 + \omega_z^2 z^2)$, where ω_x , ω_y , and ω_z are the secular frequencies in the x, y, and z directions, and m is the mass of the ion.

3.2 The Mathieu equation

All ion traps, at least in a small region around where the ion is localized, generate a potential which can be generally described as: $V(x, y, z) = U_0(\alpha x^2 + \beta y^2 + \gamma z^2) +$

$V_0 \cos(\Omega t)(\alpha' x^2 + \beta' y^2 + \gamma' z^2)$. The derivations and formalism which follow are loosely based on derivations from [30] and [31], although here we apply the analysis for a few cases of particular interest. This equation includes a static term U_0 and an oscillating term with amplitude V_0 . Throughout this thesis, the static term will be referred to interchangeably as a static voltage, DC voltage, control voltage, or quasi-static voltage. In fact, it does not have to be completely static - later we will see that these are the voltages we change in order to shuttle an ion. But in comparison to the frequency of the RF voltage, it will be static. In all of these traps discussed here it is assumed that electrodes which do not have an RF voltage applied are RF grounded via large capacitors (see figure 3.3). The only condition on these coefficients is that they satisfy Gauss' law, that $\alpha + \beta + \gamma = 0$ and $\alpha' + \beta' + \gamma' = 0$. For the time being we will ignore the specific values of these constants, other than to note that the diversity of ion trap geometries gives rise to a diverse set of relationships. Given these potentials, the equation of motion for a positive, singly charged particle of mass m is:

$$\ddot{x} + \frac{2e}{m}(U_0\alpha + V_0 \cos(\Omega t)\alpha')x = 0 \quad (3.1)$$

$$\ddot{y} + \frac{2e}{m}(U_0\beta + V_0 \cos(\Omega t)\beta')y = 0 \quad (3.2)$$

$$\ddot{z} + \frac{2e}{m}(U_0\gamma + V_0 \cos(\Omega t)\gamma')z = 0 \quad (3.3)$$

These differential equations belong in the class of linear ODE's with periodic coefficients, which are generally solved using Floquet's theorem [32]. Specifically, the solution is expressed in the general form of Mathieu's equation [33], which was originally derived as a solution to the two dimensional wave equation describing the vibrational modes of a membrane stretched over an elliptical boundary. They take the forms of Mathieu's differential equation and Mathieu's modified differential equation,

respectively:

$$\frac{d^2v}{dz^2} + (a - 2q \cos(2z))v = 0 \quad (3.4)$$

$$\frac{d^2v}{dz^2} - (a - 2q \cosh(2z))v = 0 \quad (3.5)$$

The solutions are expressed as the sum of two linearly independent components, $v = C_1 v_1 + C_2 v_2$, where $v_1 = e^{\mu z} f(z)$ and $v_2 = e^{-\mu z} f(-z)$, and $f(z)$ is a function with period π and μ is a constant called the characteristic exponent. There are two general classes of physical applications which Mathieu equations can solve: the aforementioned two dimensional wave equation with fixed boundary conditions, and a class of equations of initial value problems, which includes ions in a Paul trap. For trapped ions, only the first equation in 3.4 is used. Adapting the analysis in ?? to our situation, we write a trial solution to this equation of the form:

$$r_i(\tau) = A_i e^{\mu_i \tau} \sum_{n=-\infty}^{\infty} C_{n,i} e^{i2n\tau} + B_i e^{-\mu_i \tau} \sum_{n=-\infty}^{\infty} C_{n,i} e^{-i2n\tau} \quad (3.6)$$

where μ_i and the coefficients $C_{n,i}$ depend only on a_i and q_i , $\tau = \Omega t/2$, and A_i and B_i ($i \in \{x, y, z\}$) are chosen to satisfy the initial conditions. The constant a_i depends on the static voltage U_0 applied, and q_i depends on the RF voltage V_0 applied. They are dependent on the geometry of the trap, and will be discussed later when discussing different trap types used. By inserting equation 3.6 into equation 3.4 and matching terms with the same τ dependence, the following recurrence relation is generated:

$$-\frac{a_i + (\mu_i + 2n)^2}{q_i} C_{n,i} + C_{n-1,i} + C_{n+1,i} = 0 \quad (3.7)$$

This can be expressed in matrix form for all terms:

$$\begin{bmatrix} 1 & -\gamma_{-2n,i} & 1 & & & & & \\ & \ddots & & \vdots & & & & \\ & & 1 & -\gamma_{-2,i} & 1 & 0 & 0 & \\ \dots & 0 & 1 & -\gamma_{0,i} & 1 & 0 & \dots & \\ & 0 & 0 & 1 & -\gamma_{2,i} & 1 & & \\ & & & \vdots & & & \ddots & \\ & & & & 1 & -\gamma_{2n,i} & 1 & \end{bmatrix} \begin{pmatrix} C_{-n,i} \\ \vdots \\ C_{-1,i} \\ C_{0,i} \\ C_{1,i} \\ \vdots \\ C_{n,i} \end{pmatrix} = \vec{0} \quad (3.8)$$

where $\gamma_{2n,i} = \frac{a_i - (\mu_i + 2n)^2}{q_i}$.

A non-trivial solution for the Floquet exponent μ_i requires that the determinant of the matrix in 3.8 be 0. From this solution a region of the parameters a_i and q_i can be found where the trap is stable (unstable solutions are those for which $r_i(\tau)$ increases without limit as $\tau \rightarrow \infty$) [31]. We therefore require $\mu_i = \alpha_i \pm i\beta_i$ such that $r_i(\tau)$ remains bounded as $\tau \rightarrow \infty$. By inserting μ_i into equation 3.6, it is apparent that the stability condition requires that $\alpha_i = 0$. In the case where μ_i is purely imaginary and an integer, the solutions are periodic but unstable. Therefore μ_i must be purely imaginary and not an integer, which we require by restricting ourselves to the lowest stability region, between $\beta_i = 0$ and $\beta_i = 1$. By manipulating equation 3.8 algebraically (see [30] for a detailed description) we arrive at the continued fraction relation:

$$\beta_i^2 = a_i - q_i \left(\frac{1}{\gamma_0 - \frac{1}{\gamma_2 - \frac{1}{\dots}}} + \frac{1}{\gamma_0 - \frac{1}{\gamma_{-2} - \frac{1}{\dots}}} \right) \quad (3.9)$$

Now insert $e^{i\beta_i}$ into 3.6:

$$r_i(\tau) = A_i \sum_{n=-\infty}^{n=\infty} C_{n,i} e^{i(2n+\beta_i)\tau} + B_i \sum_{n=-\infty}^{n=\infty} C_{n,i} e^{-i(2n+\beta_i)\tau} \quad (3.10)$$

Also inserting $\Omega t/2$ for τ we can see that the frequencies of oscillation are $\omega_{n,i} = (2n \pm \beta_i)\Omega/2$, for $n = -\infty \dots \infty$. The lowest order frequency is $\omega_{0,i} = \beta_i\Omega/2$, with

the next two being $\omega_{1,i} = (1 - \beta_i/2)\Omega$ and $\omega_{2,i} = (1 + \beta_i/2)\Omega$.

When $|a_i|, q_i \ll 1$ (which are typical experimental values) the matrix in 3.8 can be reduced to a 3 by 3 matrix with the values corresponding to $C_{-1,i}, C_{0,i}, C_{1,i}$. Solving this analytically gives the approximate solution $\beta_i \approx \sqrt{q_i^2/2 + a_i}$, which is also the lowest order solution from equation 3.9. Since this is actually the imaginary portion of μ_i , it is apparent that a stable solution of $\alpha_i = 0$ requires that $q_i^2/2 + a_i \geq 0$. Graphs of the stability regions will be shown later in discussions of the different trap types. Finally inserting the value for μ_i into the recursion relation and setting the initial conditions $A_i = B_i$, we arrive at the final solution in its simplest form to second order:

$$r_i(t) = r_{0,i} \cos(\omega_i t) \left[1 - \frac{q_i}{2} \cos(\Omega t) \right] \quad (3.11)$$

where $\omega_i = \beta_i \Omega/2$ and $r_{0,i} = 2AC_{0,i}$. This equation shows two different oscillatory components to the motion of the ion. The one corresponding to ω_i is called the “secular” motion and corresponds to the time averaged harmonic potential the ion experiences in the trap. The other faster term, Ω , corresponds to “micromotion” at the frequency of the RF voltage. The secular frequency can have a different value in each direction, depending on the applied static and RF voltages, as well as the geometry of the trap. Choosing to go to higher orders gives us terms with frequencies at $(2n \pm \beta_i)\Omega/2$; we will ignore them from now on because their amplitudes decrease in powers of q_i , and for the traps tested here we will usually operate in the regime $q_i \ll 1$.

The above equations assumed that at the location of the ion there is no spurious electric field pushing the ion away from the ponderomotive potential minimum. This condition is not often met in the lab without specifically applying DC electric fields with compensation electrodes to counteract stray fields from other sources. If we assume a bias field E_i in the \hat{r}_i direction, equation 3.1 and its solution become transformed to:

$$\ddot{r}_i + \frac{2e}{m}(U_0\alpha + V_0 \cos(\Omega t)\alpha')r_i = \frac{eE_i}{m} \quad (3.12)$$

$$r_i(t) = r_{0,i} \cos(\omega_i t) \left[1 - \frac{q}{2} \cos(\Omega t) \right] + \frac{eE_i}{m\omega_i^2} + \frac{\sqrt{2}eE_i}{m\omega_i\Omega} \cos(\Omega t) \quad (3.13)$$

The first additional term, $\frac{eE_i}{m\omega_i^2}$ is the positional offset that the ion experiences as a result of the bias field. The other term, $\frac{\sqrt{2}eE_i}{m\omega_i\Omega} \cos(\Omega t)$ is the increased micromotion due to the bias field, and differs from the other micromotion term in that it cannot be laser cooled. By laser cooling the ion we are able to reduce $r_{0,i}$, and therefore minimize both the secular amplitude and the micromotion amplitude. This, however, does not effect the micromotion due to the electric field bias. The way to eliminate this term is to make sure that any bias field is compensated with the DC electrodes surrounding the ion.

3.3 The pseudo-potential approximation

Before returning to the model of the hyperbolic electrodes, we briefly discuss another technique for finding the trapping potential of an ion trap. It is called the pseudo-potential approximation [34] and is calculated by considering the average force experienced by an ion in an inhomogeneous oscillating field. In the case of a spatially homogenize field oscillating in time, such as a parallel plate capacitor, the force is proportional to $\cos(\Omega t)$ and therefore averages to zero. However, if those plates become curved, then the ion experiences a different force depending on its location, and this force does not average to zero but forms a net trapping potential. Consider one dimension of an ion's motion in a trap with oscillating voltages, which trap the ion at one instant in time and 90 degrees later is anti-trapping. During the trapping portion of its phase, the ion moves inward slightly, such that during the anti-trapping portion it is pushed back out, but with slightly less force. This is due to the inhomogeneous field getting weaker closer to the trap center. The motion of the ion derived from this analysis is identical to that in 3.11, and the mathematical solution for its potential is:

$$\Psi(x, y, z) = \frac{e}{4m\Omega^2} |\nabla V(x, y, z)|^2 \quad (3.14)$$

This expression is very useful for finding the trapping potential of an ion in a complicated geometry where analytic solutions are difficult to obtain. In this case simulations are used to determine the potential due to a voltage applied to the electrode configuration, and the results are analyzed in Mathematica to determine the potential gradient and therefore the ponderomotive and static potentials.

3.4 The 3 dimensional hyperbolic electrode trap

Consider the simple case of a hyperbolic electrode which is rotated around the z axis, forming a “ring” electrode, and two hyperbolic endcaps above and below it (see figure 3.1). For simplicity, the voltage applied to the ring is $V_0 \cos(\Omega t)$, U_0 is applied to the top and bottom endcaps, and $2z_0^2 = r_0^2$ relates the ring diameter to the endcap separation.

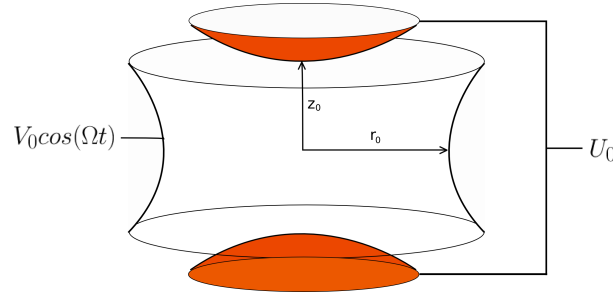


Figure 3.1: The ideal hyperbolic trap consists of a ring and two endcaps on top and bottom. Although our analysis assumes the RF voltage is applied to the ring and a static voltage is applied to the endcaps, any combination of these will work.

The surface of the ring electrode satisfies the equation $x^2 + y^2 - 2z^2 = d_0^2/2$ and the endcaps satisfy $x^2 + y^2 - 2z^2 = -d_0^2/2$, where $d_0^2 = r_0^2 + 2z_0^2$. For these conditions, the potential on all of the electrodes can be written exactly as $V_{hyp}(x, y, z) = V_0 \cos(\Omega t) \left(\frac{x^2 + y^2 - 2z^2}{d_0^2} + \frac{1}{2} \right) - U_0 \left(\frac{x^2 + y^2 - 2z^2}{d_0^2} - \frac{1}{2} \right)$. Since this equation satisfies the Dirich-

let boundary conditions on all of the electrodes, it is a solution for the voltage at all points in space as well. The motion of the ion in one dimension can be found from solving the separable equation $\ddot{r}_i = -\frac{e}{m}(\vec{\nabla}V(r, t) \cdot \hat{r}_i)$, where e is the charge of the ion and r_i is any coordinate direction. This gives us an equation of motion in the \hat{x} , \hat{y} , and \hat{z} directions of:

$$\ddot{x} + \frac{2e}{md_0^2}(V_0 \cos(\Omega t) - U_0)x = 0 \quad (3.15)$$

$$\ddot{y} + \frac{2e}{md_0^2}(V_0 \cos(\Omega t) - U_0)y = 0 \quad (3.16)$$

$$\ddot{z} - \frac{4e}{md_0^2}(V_0 \cos(\Omega t) - U_0)z = 0 \quad (3.17)$$

By transforming the equation of motion to the Mathieu equation of the type expressed in 3.4, we arrive at the constants:

$$a_{x,y} = -\frac{8eU_0}{m\Omega^2 d_0^2}, \quad q_{x,y} = -\frac{4eV_0}{m\Omega^2 d_0^2} \quad (3.18)$$

$$a_z = \frac{16eU_0}{m\Omega^2 d_0^2}, \quad q_z = \frac{8eV_0}{m\Omega^2 d_0^2} \quad (3.19)$$

Based on the relationship between a_i and q_i a diagram of the lowest stability region can be generated (figure 3.2), where β_i is real valued and between 0 and 1.

3.4.1 Ring and Fork Trap

Experimentally, this trap takes a slightly different form than the perfect hyperbolic trap seen in figure 3.1, and is referred to as a “ring and fork” trap [35]. In our lab we make these out of 125 μm thick molybdenum sheets, one with a hole (forming the ring) and the other with a notch (the fork). This can be seen in figure 3.3. Molybdenum is a good material for building ion traps because it is stiff, is a good electrical conductor, and its native oxide has a work function which is very close to the work function of molybdenum itself. This helps suppress electric field noise on the electrodes, which we will be discussed in chapter 8.

As one can see from the figure, this trap departs radically from a perfect hyperbola

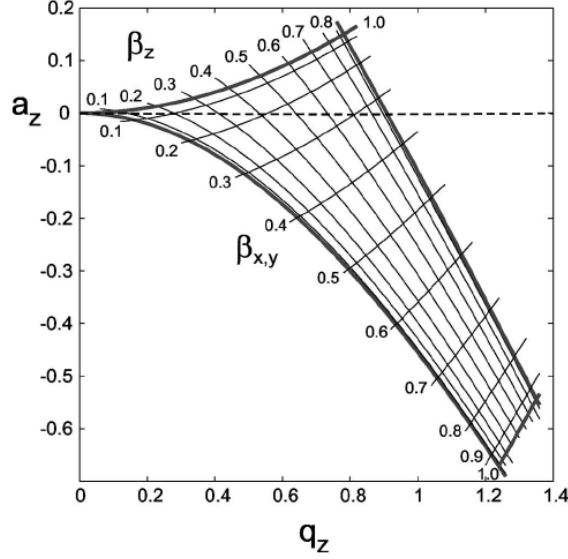


Figure 3.2: The boundary lines in this graph define the lowest stability regime for the ion trap, corresponding to $0 < \beta < 1$. This diagram is only valid for the geometry and dimensions of the example presented here, i.e. $2z_0^2 = r_0^2$, as that defines the relationship between $\beta_{x,y}$ and β_z .

in that the ring is essentially two dimensional and the end caps are not only not hyperbolic but are not even radially symmetric. Starting with the geometry of an ideal hyperbolic trap, with constants $a_x = a_y = a$, $a_z = -2a_x = -2a$, $q_x = q_y = q$, and $q_z = -2q_x = -2q$, we calculate the secular frequencies for a symmetric hyperbolic trap with an efficiency factor η (if the end caps are symmetric but not perfectly hyperbolic), and an asymmetric trap parametrized by α (where $\alpha = 1/2$ is ideal) with an efficiency factor η (such as the ring and fork trap):

$$\begin{array}{lll}
 \text{Ideal:} & \omega_x = \frac{\Omega}{2} \sqrt{a + \frac{q^2}{2}} & \omega_y = \frac{\Omega}{2} \sqrt{a + \frac{q^2}{2}} & \omega_z = \frac{\Omega}{2} \sqrt{-2a + 2q^2} \\
 \text{Symmetric, } \eta: & \omega_x = \frac{\Omega}{2} \sqrt{\eta a + \frac{(\eta q)^2}{2}} & \omega_y = \frac{\Omega}{2} \sqrt{\eta a + \frac{(\eta q)^2}{2}} & \omega_z = \frac{\Omega}{2} \sqrt{-2a\eta + 2(\eta q)^2} \\
 \text{Asymmetric, } \eta: & \omega_x = \frac{\Omega}{\sqrt{2}} \sqrt{\eta a \alpha + \frac{(\eta q)^2}{2} \alpha^2} & \omega_y = \frac{\Omega}{\sqrt{2}} \sqrt{\eta a (1 - \alpha) + \frac{(\eta q)^2}{2} (1 - \alpha)^2} & \omega_z = \frac{\Omega}{2} \sqrt{-2a\eta + 2(\eta q)^2}
 \end{array}$$

The last equation describes a ring and fork trap. First, notice that the efficiency factor η (where $0 < \eta \leq 1$) weakens the trap, as expected. This is an acceptable loss, as it can be offset by increasing the RF voltage applied. For a typical ring and fork trap, η is around .5; for more exotic geometries, like those consisting of three rings, this factor can drop to .1 [36]. In either case the RF voltage applied can be proportionately increased to compensate for the weakening of the trap. Additionally, ω_x and ω_y are now not degenerate due to the factor α , where $0 < \alpha \leq 1/2$. Since

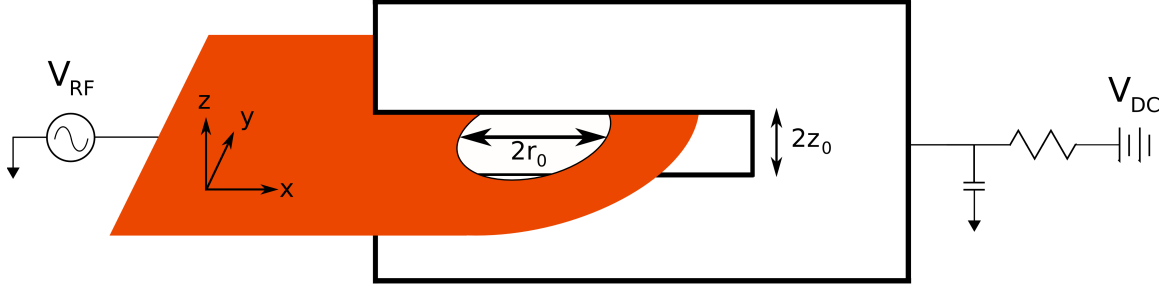


Figure 3.3: One easy experimental realization of a hyperbolic trap is the ring and fork trap, consisting of a flat sheet with a hole cut in it and surrounded on the top and bottom by “fork” endcaps. The voltages applied are shown in the diagram, with the low pass circuit on the fork electrode which serves to ground the RF potential but allow the application of a static voltage.

the fork end cap is straight, the axis parallel to the fork should be weaker in strength than the axis perpendicular, and therefore ω_x is designated as this direction. Breaking this degeneracy is actually beneficial because it allows Doppler cooling in all three dimensions with a single laser. As a simplified case, we see that the ring and fork trap with $U_0 = 0$ gives: $\omega_x = \frac{\sqrt{2}\epsilon\eta V_0}{m\Omega d_0^2}\alpha$, $\omega_y = \frac{\sqrt{2}\epsilon\eta V_0}{m\Omega d_0^2}(1 - \alpha)$, and $\omega_z = \frac{2\sqrt{2}\epsilon\eta V_0}{m\Omega d_0^2}$. The $\hat{x}, \hat{y}, \hat{z}$ directions define the principal axes of the trap, which are the directions along which the ion’s harmonic motion is uncoupled from the other directions. In the case of the ring and fork trap it is straightforward to determine the principal axes, but we will see later on that finding these axes in the case of two layer linear traps and surface traps can often require the use of computer simulations.

In our lab we have used a ring and fork trap with a $200 \mu\text{m}$ radius and the fork electrodes separated by $300 \mu\text{m}$. By applying ~ 400 volts of $\Omega/2\pi = 50$ MHz RF voltage to the ring, along with 30 volts on the endcaps, we can achieve a trap with $\omega_x/2\pi = 5.8$ MHz, $\omega_y/2\pi = 8.9$ MHz, and $\omega_z/2\pi = 9.7$ MHz. From an experimental standpoint, the static voltage is applied through a low pass filter to the endcaps. This way the RF voltage is grounded via a capacitor, and the static voltage source does not have a high, oscillating voltage being applied to its outputs. Additional compensating electrodes are placed about 1 cm away from the trap to offset any bias electric fields affecting the ion. Given they are so far away compared to the electrodes of the trap, a few thousand volts are typically required to offset the background fields.

3.4.2 Needle trap

Another type of 3-D hyperbolic trap which will be discussed in greater detail later in chapter 8 is the two needle trap (figure 3.4). This is like the hyperbolic trap but without the ring, and is equivalent to the case where $r_0 \rightarrow \infty$. It turns out that if the needles are made pointy (with a radius of curvature small compared to the needle to needle separation), the efficiency of this trap does not suffer too much compared to the hyperbolic trap with a ring electrode. For the experiments performed here with the needle trap, this efficiency was calculated to be $\eta \sim .17$ over a $2z_0$ separation of $100 \mu\text{m}$ to $250 \mu\text{m}$.

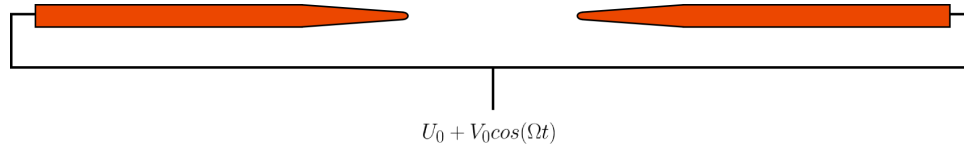


Figure 3.4: This geometry is related to the hyperbolic trap, where the endcaps are the needles and the radius of the ring $r_0 \rightarrow \infty$. This geometry is very open optically, and subsequently is also very susceptible to bias electric fields. An experimental realization of this might also include grounded sleeves farther back on the needles which serve to mitigate the problem of stray bias fields.

When there are multiple ions in a 3-D ion trap, they line up along the weak axis. This brings us to one of the main disadvantages of the 3-D hyperbolic trap for experiments which require multiple ions (such as demonstrations of entanglement or any other quantum computing application). When we have multiple ions, they cannot all be at the single RF node, and therefore those that aren't experience a higher degree of micromotion which cannot be cooled. This motivates the building of linear traps, which are discussed in the next section.

3.5 Linear traps

A linear ion trap refers to any ion trap in which the ponderomotive potential only traps in two dimensions such that the RF node is a line. Static voltages are used to confine the ions at specific points along this line. As mentioned above, this has the benefit that if the secular frequency along the static axis is lower than the ponderomotive secular frequency, then multiple ions will space themselves out along this linear RF node but not experience excess micromotion, since they are still all at the RF node. Three types of linear traps are shown in figure 3.5: a single layer trap (a), a two layer trap (b), and a three layer trap (c). In each case the trap is shown above, along with the static and RF potentials applied to the electrodes, and a plot of the ponderomotive potential for a transverse cross section of the trap.

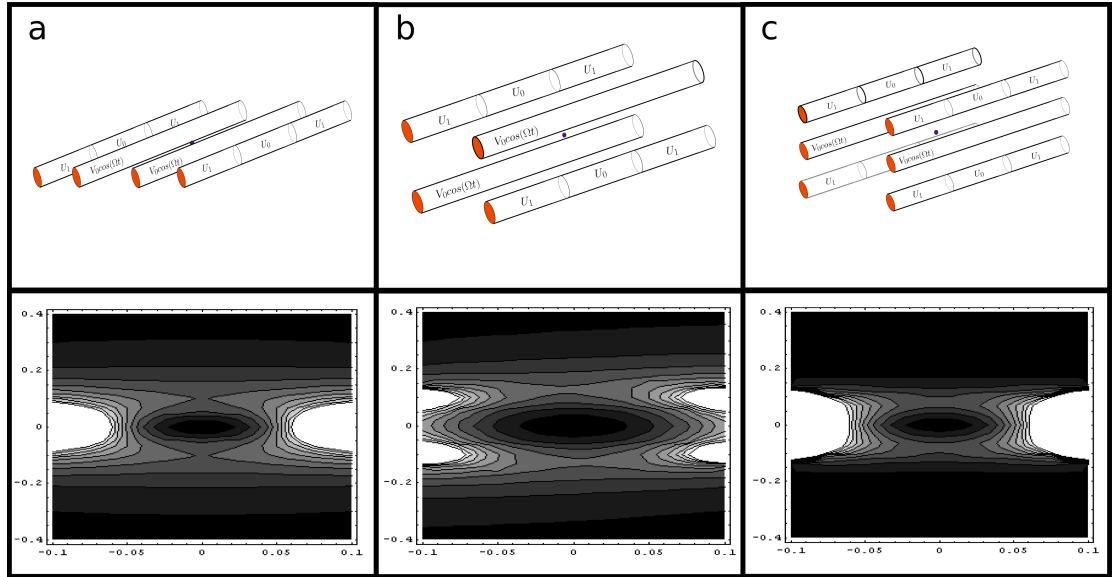


Figure 3.5: This figure shows three common types of linear trap: the ^a single layer trap, the ^b two layer trap, and the ^c three layer trap. The static (U_0) and RF (V_0) voltages applied to the electrodes are written on the top figure. Below each trap is a contour plot of the ponderomotive potential resulting from that trap, calculated in CPO 3D. The darker areas correspond to lower potential, and the white areas correspond to near the electrodes. The black dot in the middle of the electrodes corresponds to where an ion would be trapped.

3.5.1 Four rod trap

We will first look at the two layer trap, also referred to as a four rod trap, as it is the easiest to analyze mathematically. The ideal instance of this is comprised of four hyperbolic electrodes (see the cross section shown in figure 3.6).

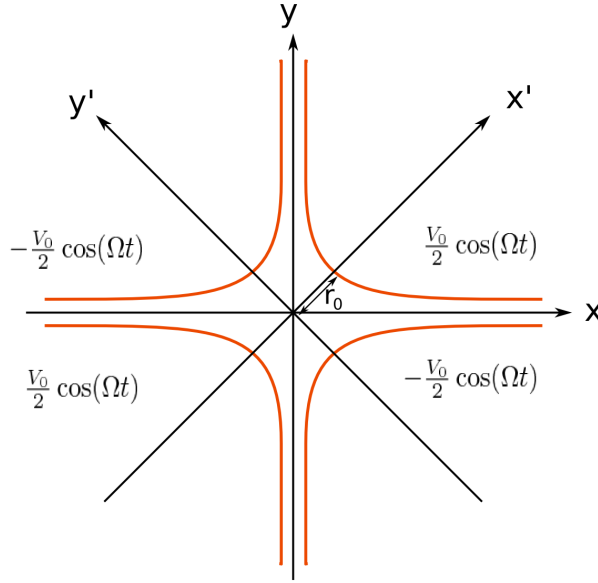


Figure 3.6: This figure shows the transverse cross section of a linear hyperbolic trap, as well as the potentials applied to the electrodes. The x' and y' axes correspond to the principal axes, in which the harmonic motion of the ion is uncoupled.

The potential of a four rod trap with only RF voltage applied, expressed in regular, rotated coordinates, and cylindrical coordinates is:

$$V_{hyp}(x, y) = -\frac{V_0}{r_0^2}(xy) \quad (3.20)$$

$$V_{hyp}(x', y') = \frac{V_0}{2r_0^2}(x'^2 - y'^2) \quad (3.21)$$

$$V_{hyp}(r, \theta') = \frac{V_0}{2r_0^2}r^2(\cos^2(\theta) - \sin^2(\theta)) = \frac{V_0 r^2}{2r_0^2} \cos(2\theta) \quad (3.22)$$

where r_0 is the distance from the ion to the nearest electrode and θ' is the angle from the positive x axis. Using the pseudo-potential approximation in equation 3.14 and calculating the resultant secular frequency gives:

$$\Psi_{hyp} = \frac{e^2 V_0^2}{4m\Omega^2 r_0^4} (x'^2 + y'^2) \quad (3.23)$$

$$\omega_{hyp} = \frac{eV_0}{\sqrt{2}m\Omega r_0^2} \quad (3.24)$$

The stability diagram for this trap is shown in figure 3.7.

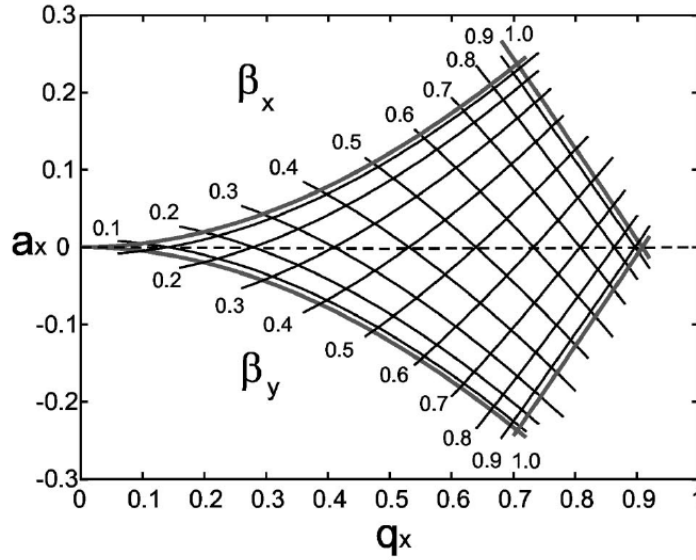


Figure 3.7: This graph shows the lowest stability region for a hyperbolic linear trap. The β_x and β_y regions are symmetric because of the trap's symmetry about the RF node.

Much of the effort for this thesis was spent working on two layer microtraps, which differ substantially from the ideal case in that the electrodes are not hyperbolic, but are flat planes in which the vertical electrode separation is much smaller than the lateral separation. Unlike the hyperbolic electrodes, they are not cylindrically symmetric, although they do have a mirror symmetry across both the $z=0$ plane and

the $x=0$ plane. The difference between this and the ideal case can be parametrized by decomposing the potential into an infinite series of cylindrical harmonics [37] and calculating the voltage for the linear microtrap, V_{lm} :

$$V_{lm} = V_0 \left[\sum_{m=1}^{\infty} C_m (r/r_0)^m \cos(m\theta') + \sum_{n=1}^{\infty} S_n (r/r_0)^n \sin(n\theta') \right] \quad (3.25)$$

Because the voltage is the same on diagonal electrodes and opposite on adjacent ones, we only need to keep the terms which are the same when $\theta' \rightarrow \theta' + \pi$ and opposite when $\theta' \rightarrow \theta' + \pi/2$, i.e. $m = 2, 6, 10 \dots$ and $n = 4, 8, 12 \dots$. These terms can be found using numerical simulations, with the amplitudes of C_n and S_n ($m, n \geq 2$) quantifying the anharmonicity of the trap. Defining the distance to the electrodes as $l = \sqrt{(a/2)^2 + (d/2)^2}$ (where a and d are defined in figure 3.8), and comparing the voltage of the linear microtrap to that of a four rod hyperbolic trap with $r_0 = l$, we define an efficiency factor and potential:

$$\eta = \frac{V_{lm}}{V_{hyp}} = \frac{2C_2 l^2}{r_0^2} \quad (3.26)$$

$$V_{lm}^{(2)}(x', y') = \frac{V_0 \eta}{2l^2} (x'^2 - y'^2) \quad (3.27)$$

The resulting ponderomotive potential and transverse secular frequency is:

$$\Psi_{lm}^{(2)} = \frac{e^2 V_0^2 \eta^2}{4m\Omega^2 l^4} (x'^2 + y'^2) \omega_{lm} = \frac{eV_0 \eta}{\sqrt{2}m\Omega l^2} \quad (3.28)$$

This equation shows that the ponderomotive potential at the trap axis is circular; from numerical simulations we have found that it is approximately circular up to a distance of $\frac{a}{8}$, at which point C_2 becomes significant. We have used several different finite element modeling (FEM) packages to determine the trap's anharmonicity, including a 2-D solver in Matlab, Maxwell 3D from Ansoft, and Opera 3D from VectorFields. For these simulations the geometry and voltages of the electrodes (and sometimes the electrode material properties, such as permittivity and conductivity) are defined, and a volume region of interest is defined which includes the trap location.

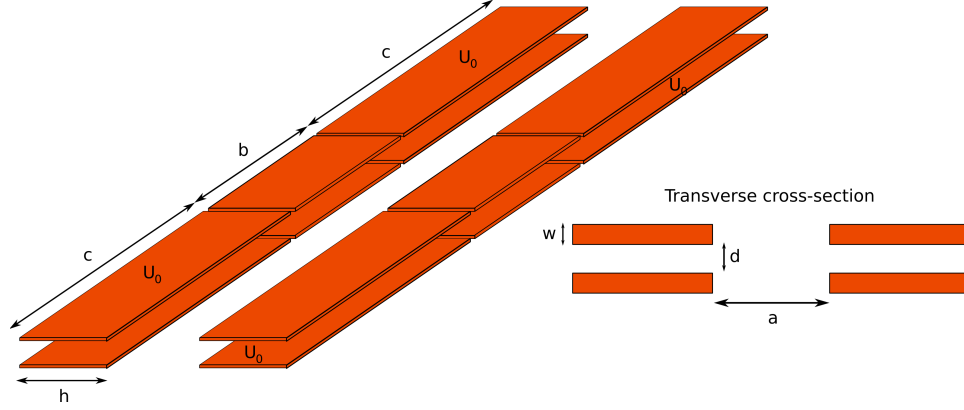


Figure 3.8: This trap is an experimental realization of a two layer linear trap, behaving to first order like the hyperbolic trap described above. The picture of the electrodes shows different important dimensions. Below it is a transverse cross section superimposed on a diagram of the ponderomotive potential.

This region of interest is divided into tetrahedra, and the potential at each vertex is calculated in an iterative process until they are internally consistent and consistent with the boundary conditions set at the beginning. More recently we have used CPO 3D from Electronoptics, which is a boundary element modeling program (BEM) in which the defined electrodes are divided into segments, and surface charges which are evenly distributed over each segment are calculated to satisfy the boundary voltage conditions. The potential at points in the region of interest are then simply calculated by summing the Coulomb potentials for each segment. This technique is much faster and more accurate than the FEM solvers, and furthermore the potential can be quickly recalculated when changing the voltage on an electrode by simply rescaling the distributed charge.

In the specific case of the two layer gallium arsenide trap, whose fabrication details will be discussed in section 6, we were initially concerned that the high aspect ratio $\alpha = a/d$ would lead to a much weaker trap. This was investigated first with numerical simulations using Maxwell 3D. From figure 3.9a, which graphs the efficiency factor η as a function of α and for different values of $\delta = d/w$, we see that the efficiency decreases steeply after $\alpha = 1$ but asymptotically approaches $1/\pi$. The graph also shows that the trap gets weaker for geometries with thinner electrodes. A similar plot (figure

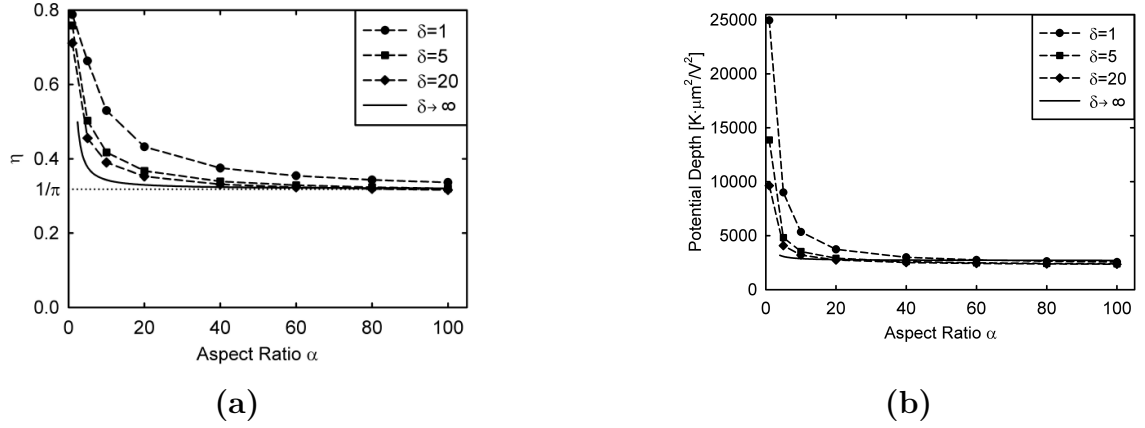


Figure 3.9: The graph in part **a** shows how the trap strength decreases as the aspect ratio α (lateral separation of electrodes divided by the vertical separation) increases. This quantity is parametrized by η , which equals 1 for an aspect ratio of 1 and asymptotically goes to $1/\pi$ as $\alpha \rightarrow \infty$. In part **b** we see that the maximum potential along a line perpendicular to the surface of the trap decreases with α , and see that it too approaches an asymptotic value.

3.9b) shows how the potential depth in and out of the plane of the trap depends on α . In traps which an “open” geometry, such as the two layer geometry shown here with an open \hat{y} direction and a confined \hat{x} direction (because of the presence of an electrode), the direction with lowest trap depth (not necessarily lowest secular frequency) will be the open direction. While having a high secular frequency is good for tightly confining an ion and performing fast gate operations (as will be described later), from the standpoint of just trapping ions the important metric is the value of the shallowest potential in a particular direction. Traps have been successfully operated with minimum trap depths of between .08 eV (3 times room temperature) and several eV (hundreds of times room temperature).

3.5.1.1 Modelling a two layer trap using conformal mapping

One can also calculate the effect of using planar electrodes instead of perfect hyperbolas using conformal mapping. This technique is generally useful for transforming two dimensional problems in space to problems in the complex plane, as long as a

suitable mapping can be found. For our problem we adapted an analysis of fringe fields in a parallel plate capacitor [38, 37] for a two layer ion trap with infinite plane, zero width electrodes. In the complex plane this can be described as lines parallel to the real axis starting at $(\pm a/2, \pm d/2)$ and extending to $(\pm\infty, \pm d/2)$. These electrodes then get mapped to a parallel plate capacitor, as seen in figure 3.10, and obey the relationship:

$$\pm \frac{2w\pi}{d} + \frac{a\pi}{d} - 1 = z + e^z \quad (3.29)$$

where the positive value of the first term is used for the electrodes on the left and the negative value for the equations on the right. This transformation maps the original electrodes to two infinite planes separated by 2π , where the potential in between is that of a parallel plate capacitor, $V = \frac{V_0}{2\pi} \text{Im}(z)$. Different mapping functions must be used so that the same voltage is applied on one side of the parallel plate capacitor. To find the potential in the original problem the inverse of equation 3.29 must be solved using the Lambert W function $W_k(x)$, which obeys the equation $z = W_k(z)e^{W_k(z)}$. The inverse mapping is then $z_{\pm} = \zeta_{\pm} - W_k(e^{\zeta_{\pm}})$, where $\zeta_{\pm} = \pm \frac{2w\pi}{d} + \frac{a\pi}{d} - 1$. The k subscript in the Lambert W function signifies that we have to choose the appropriate branch in the complex plane, and is given to us by [38] as $k = \lceil \frac{\text{Im}(\zeta) - \pi}{2\pi} \rceil$. Now we have z (the coordinates in the transformed, parallel plate capacitor frame) as a function of w (the coordinates in the original two layer ion trap problem).

In the case of the GaAs trap discussed later, $a \gg d$, which allows us to add the solutions corresponding to the two different inverse transforms z_{\pm} independently, as we assume that since the opposite electrodes are so far away that they minimally affect each other. Therefore we can write the original potential as a linear sum of the two different sides of the ion trap, $V = \frac{V_0}{2}(\text{Im}(z_+) + \text{Im}(z_-))$. The high aspect ratio also allows us to make an approximation for the Lambert W function, since $\zeta \gg 1 \rightarrow W_0(\zeta) \approx \ln \zeta - \ln(\ln \zeta)$. Inserting this into the mapping function above, and we get $z \approx \ln(\zeta_{\pm})$. The resulting function can be expanded about $w = 0$ to:

$$z_{\pm} = \ln\left(\frac{a\pi}{d} - 1\right) + \sum_{n=0}^{n=\infty} \frac{1}{(-2)^n} \left(\pm \frac{2\pi w}{a\pi - d}\right)^{n+1} \quad (3.30)$$

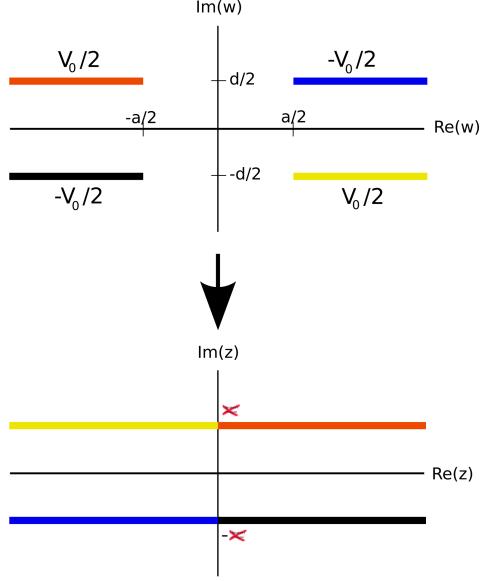


Figure 3.10: Using the technique of conformal mapping we can map the geometry of a two layer trap in the complex plane to a parallel plate capacitor, in which the voltage is known. The colors of the electrodes show how they get mapped to the parallel plate capacitor.

When we plug this into the equation $V = \frac{V_0}{2\pi}(Im(z_+) + Im(z_-))$, we see that all even n terms cancel, and that the first term disappears because it is real valued:

$$V = \frac{V_0}{\pi} \sum_{n=0}^{n=\infty} -2 \left(\frac{-\pi}{a\pi - d} \right)^{2n+2} Im(w^{2n+2}) \quad (3.31)$$

Evaluating the above expression at $w = x + iy$ gives:

$$V = -\frac{4\pi V_0}{(a\pi - d)^2} (xy + [3(x^5y + y^5x - 10x^3y^3)] + \dots) \quad (3.32)$$

We can see from this that near the trap it is only necessary to keep the first term, as the r^2 term is large compared to the r^6 term. Using the pseudo-potential approximation (section 3.3), we find that:

$$\Psi = \frac{e^2}{4m\Omega^2} \left(\frac{4\pi V_0}{(a\pi - d)^2} \right)^2 (x^2 + y^2) \quad (3.33)$$

$$= \frac{e^2 V_0^2 \eta^2}{4m\Omega^2} (x^2 + y^2) \quad (3.34)$$

$$\eta = \frac{4\pi}{(a\pi - d)^2} l^2 = \frac{\pi(\alpha^2 + 1)}{(\alpha\pi - 1)^2} \quad (3.35)$$

where $l = \sqrt{(a/2)^2 + (b/2)^2}$ is the distance to the nearest electrode. Remember that we assumed $\alpha \gg 1$, in which limit $\eta \rightarrow 1/\pi$ and agrees with the simulations above as $\alpha \rightarrow \infty$. In [37] the trap depth is also calculated from this conformal mapping solution, and the maximum trap depth is found at: $r_{max} = \frac{a}{2}(1 - \frac{1}{\pi a})$:

$$\Psi(r_{max}) = \frac{e^2 V_0^2}{4m\Omega^2} \frac{1}{a^2 \pi^2 (1 - 1/a\pi)^2} \quad (3.36)$$

where in the limiting case $\Psi(r_{max}) \rightarrow .23 [\text{eV} \cdot \mu\text{m}^2/\text{V}^2]$ as $\alpha \rightarrow \infty$.

3.5.1.2 Evaluation of the harmonic deviations

Returning to the analysis of the anharmonicities in the linear microtrap, we concern ourselves primarily with the values of the first terms in the expansion 3.25 at the trap center. This is plotted in figure 3.11, and it is apparent that for relatively high aspect ratios (for the GaAs trap we demonstrated in chapter 6, $\alpha = 15$), the anharmonicity is below a few percent. Also in the linear microtrap, the anharmonicities grow at points farther from the center of the trap. This can be seen in figure 3.12.

One last concern with the ponderomotive potential is that linear traps are not perfectly linear - real world implementations require gaps between adjacent electrodes that can give rise to axial rf fields, and result in slightly trapping or anti-trapping potentials along the rf node. While static fields will completely dominate this axial potential, it is still a deleterious effect since the DC and RF axial minima might not coincide, in which case the axial micromotion is non-zero. This effect can be quantified by adding the term σ_z into the pseudo-potential equation $\Psi_{lm}(x, y, z) = \frac{e^2 V_0^2 \eta^2}{4m\Omega^2 l^4} (x^2 + y^2 + \sigma_z z^2)$. From [37] this term was calculated for typical values of the gap and electrode size, and found to be on the order of 10^{-13} , and is therefore neglected in future analysis.

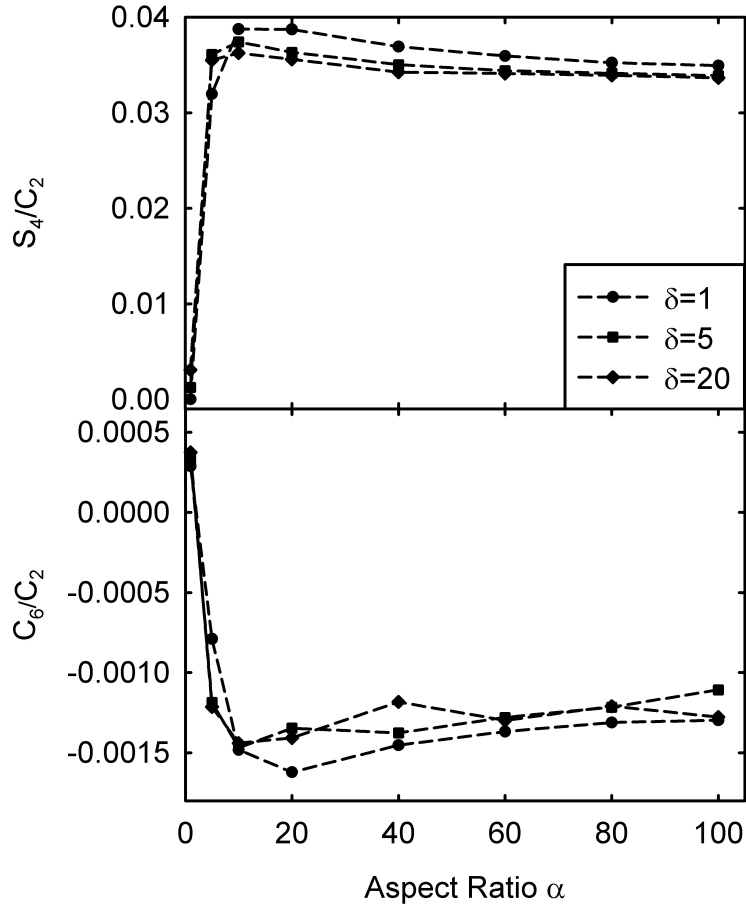


Figure 3.11: This graph shows the first two anharmonic terms in the cylindrical expansion of the two layer trap, S_4 and C_6 , as a function of the aspect ratio α . We can see that at worst they have a 4% and .2% effect. The coefficients are calculated for different values of $\delta = d/w$.

3.5.1.3 Static confining potentials

Since linear traps require static fields in order to confine ions along the RF node, we want to include those potentials in our analysis. It might seem that the effect of static electrodes only needs to be analyzed along the axial direction, but by Gauss' law we know that those electric field lines that converge at the trap center must be radially anti-trapping, and therefore they partially cancel the ponderomotive potential. Therefore it is important to have a feeling for their effect in all directions so that the competing interests of a having a strong radial trap and a strong axial trap are

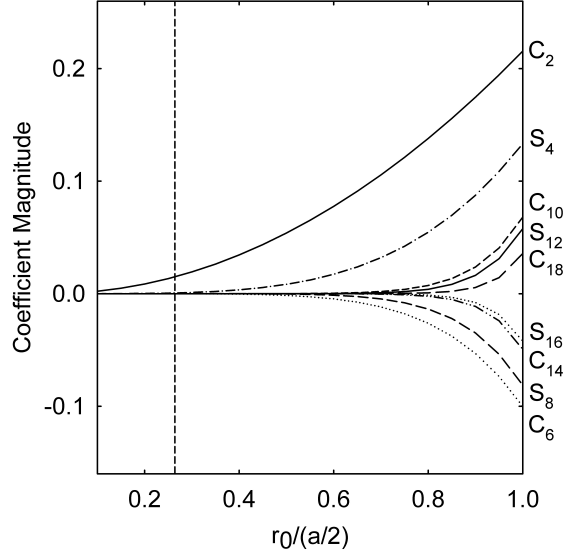


Figure 3.12: This graph shows how the trap gets more anharmonic farther from the center of the trap, parametrized as $r_0/(a/2)$, where $a/2 \approx$ the distance from the ion to the electrode for high aspect ratio traps.

met.

From figure 3.8, we simulate a trap with U_0 volts applied to the end cap electrodes, and then find the potential $U(x, y, z)$ around the trap center $(0, 0, 0)$. The static potential can then be parametrized by

$$U_{lm} = \frac{U_0}{2}(D_x x^2 + D_y y^2 + D_z z^2) \quad (3.37)$$

where

$$D_x = \frac{1}{U_0} \frac{\partial^2 U_{lm}}{\partial x^2}(0, 0, 0) \quad (3.38)$$

$$D_y = \frac{1}{U_0} \frac{\partial^2 U_{lm}}{\partial y^2}(0, 0, 0) \quad (3.39)$$

$$D_z = \frac{1}{U_0} \frac{\partial^2 U_{lm}}{\partial z^2}(0, 0, 0) \quad (3.40)$$

These constants obey the relation that $D_x + D_y + D_z = 0$, and since we know that $D_z > 0$, we know that either $D_x < 0$ and/or $D_y < 0$. Along the axial \hat{z} direction

we see that the secular frequency will be $\sqrt{\frac{D_z U_0 e}{m}}$. The total potential and secular frequency in each direction is then:

$$\Phi_{lm} = \Psi_{lm} + U_{lm} \quad (3.41)$$

$$= \frac{e^2 V_0^2 \eta^2}{4m\Omega^2 l^4} (x^2 + y^2) + \frac{U_0}{2} (D_x x^2 + D_y y^2 + D_z z^2) \quad (3.42)$$

so that

$$\omega_{lm,x} = \sqrt{\frac{e^2 V_0^2 \eta^2}{2m^2 \Omega^2 l^4} + \frac{D_x U_0 e}{m}} \quad (3.43)$$

$$\omega_{lm,y} = \sqrt{\frac{e^2 V_0^2 \eta^2}{2m^2 \Omega^2 l^4} + \frac{D_y U_0 e}{m}} \quad (3.44)$$

$$\omega_{lm,z} = \sqrt{\frac{D_z U_0 e}{m}} \quad (3.45)$$

3.5.1.4 Principal axes

Finding the principal axes of the two layer linear ion trap require the use of simulations. We can see that for the case where $U_0 = 0$, when only the ponderomotive potential plays a role, the transverse principal axes are degenerate. A small static voltage applied (such that $\omega_{x'} \approx \omega_{y'}$) to the RF electrodes would break this degeneracy, resulting in principal axes in the \hat{z} , $\frac{1}{\sqrt{2}}(\hat{x} + \hat{y})$, and $\frac{1}{\sqrt{2}}(\hat{x} - \hat{y})$ directions. This can be seen from considering the perfect hyperbolic four rod trap which would have the same transverse principal axes at angles 45° and -45° from the \hat{y} direction, and realizing that it is a first order approximation to the linear microtrap at the RF node.

To find the principal axes when we apply larger static voltages, we calculate the Hessian matrix at the center of the trap from simulations, and then find the eigenvalues of the matrix, which denote the principal axes. We show this by example. If static voltages are applied which break the degeneracy, the potential contours are elliptical. For the case of principal axes in the \hat{x} and \hat{y} directions, an equation of the form $\Phi \propto \frac{x^2}{a^2} + \frac{y^2}{b^2}$, where $a > b$, would describe a trap with $\omega_x < \omega_y$. If we rotate

this counterclockwise by θ , we would have $\Phi \propto \frac{(\cos(\theta)x + \sin(\theta)y)^2}{a^2} + \frac{(-\sin(\theta)x + \cos(\theta)y)^2}{b^2}$. The Hessian matrix is defined as:

$$\begin{bmatrix} \frac{\partial^2 \Phi}{\partial x^2} & \frac{\partial^2 \Phi}{\partial x \partial y} \\ \frac{\partial^2 \Phi}{\partial y \partial x} & \frac{\partial^2 \Phi}{\partial y^2} \end{bmatrix} = 2 \begin{bmatrix} \frac{\cos^2(\theta)}{a^2} + \frac{\sin^2(\theta)}{b^2} & \sin(\theta) \cos(\theta) \left(\frac{1}{a^2} - \frac{1}{b^2} \right) \\ \frac{\cos^2(\theta)}{a^2} + \frac{\sin^2(\theta)}{b^2} & \sin(\theta) \cos(\theta) \left(\frac{1}{a^2} - \frac{1}{b^2} \right) \end{bmatrix} \quad (3.46)$$

The eigenvectors of this matrix are $(\cot(\theta), 1)$ and $(-\tan(\theta), 1)$, which correspond to the rotated axes of the ellipse (see figure 3.13). As one looks at the potential farther from the center of the trap, these potential contour lines rotate away from the principal axes. We can ignore this because a trapped ion does not stray that far from the center of the trap; a cool ion remains confined within a region of ~ 10 nm.

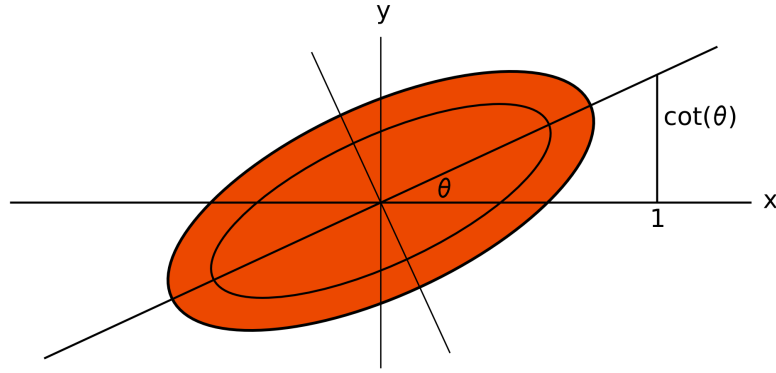


Figure 3.13: Finding the principal axes of a novel trapping structure requires simulating the combined ponderomotive and static potentials and then finding the eigenvectors of the Hessian matrix at the trap center. For these traps the transverse potential will be elliptical to varying degrees.

3.5.1.5 Two layer junction

When two layer junctions meet, their RF nodes intersect. Unfortunately, the trapping potential in the \hat{y} direction becomes severely weakened at the junction,

so as to make an unmodified two layer trap impractical as an architecture for an array of traps in which shuttling ions is possible. This can be seen qualitatively by modeling a two layer junction as a hyperbolic electrode in each of the 8 octants of three dimensional space, with (0,0,0) being the junction, and each neighboring electrode having the opposite RF voltage. The potential in the trap is then $\Phi \propto xyz$, so the ponderomotive potential at the junction is $\Psi \propto |\nabla\Phi|^2 = (xy)^2 + (yz)^2 + (xz)^2$. Along any of the axes the potential is a constant 0, and so there is no trap preventing the ion from escaping out of the top and bottom. This is an obvious result; in the case of the hyperbolic junction the vertical axis is equivalent to the two lateral axes, which don't have axial pseudo-potentials either. It should also be noted that this is not necessarily a good approximation to a two layer trap with flat electrodes. Indeed, if we run a computer simulation we see that there is a non-zero trapping potential in the vertical dimension due to the anharmonicities of the potential, and so in principal we could have a junction trap with this geometry. As we will see in a later chapter about the T-trap, the task of shuttling an ion through a junction is difficult enough without the trap being really weak in addition.

One solution to this problem is to add bridges between the RF electrodes in the junction region, a technique which is being tried by the NIST group [39]. By “plugging” the RF hole (see figure 3.14) with bridges, they are able to maintain a strong trap even in the junction region. Their trap is fabricated by electroplating gold on an alumina substrate, and then aligning the vertical layers together. While this is a good way to extend the two layer trap for shuttling purposes, it is mostly limited to manually assembled traps, as the criss crossing bridges cannot be implemented in most lithographically fabricated traps (an exception is the polysilicon trap discussed later).

3.5.2 Single layer trap

The single layer trap is similar to the two layer trap, but with all of the electrodes moved into the same plane (figure 3.15). One nice feature of this trap is the ease

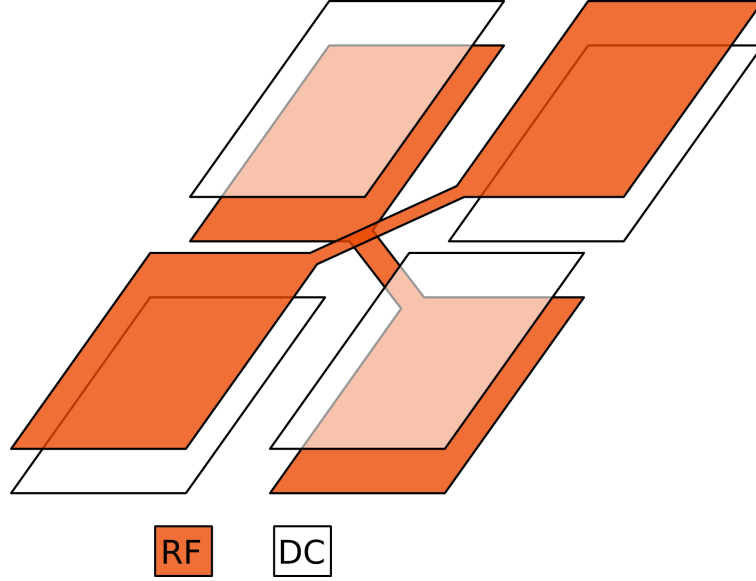


Figure 3.14: Two layer traps do not have a ponderomotive vertical trapping component at a junction. A solution to getting around this problem is to connect diagonal RF electrodes with bridges at the junction. This technique of capping the ponderomotive hole in the vertical dimension is being tried at NIST for a trap with a junction and extended linear region.

of fabrication. Many fabrication woes arise from having multiple layers - such as increased capacitance and voltage breakdown problems. Also, the traditional strength of semiconductor fabrication lies in the lateral flexibility of lithography, while vertical structure and machining tend to be more difficult. Another nice feature of this trap is that it maintains a ponderomotive trap at a junction, as opposed to its two layer relative. This particular layout will be discussed in more detail in section 7.2.

The single layer four rod geometry can be implemented with either two RF wires surrounding the center of the trap or with an RF and a DC on either side, as seen in the transverse dimensions in figure 3.15. In the first case, the trap center lies symmetrically between the RF electrodes, while in the second case there are two trap centers, one above the plane of the trap and one below, as determined by the wire diameter and spacing. This second case is compared with a two layer trap in [39] using complex variables and line charges to arrive at an analytic solution for the ponderomotive potential.

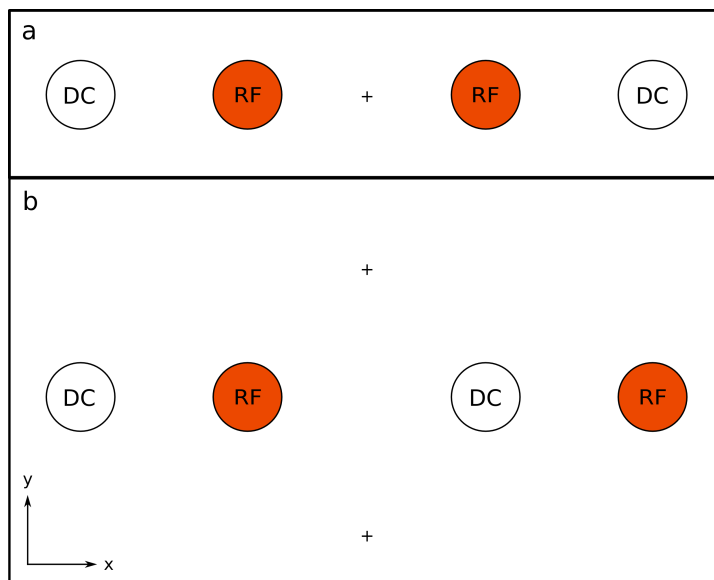


Figure 3.15: In this figure we see two different types of single layer trap geometries. In part **a** we see one with RF electrodes surrounding the RF nodal axis, denoted by an “x”. The Sandia trap discussed in section 7.2 is of this type. In part **b** there is a trap with the same geometry, but with alternating wires of RF and static voltages. In this case there are two nodal axes, above and below the plane of the trap. This is similar to the surface trap which will be discussed later, but with two allowed RF nodes.

3.5.3 Three layer trap

The three layer trap (figure 3.16) has been used extensively in my lab for a variety of experiments, from demonstrating Grover’s algorithm to shuttling an ion around a corner. From a geometric point of view, the three layer trap has the advantage that junctions are possible with it and that micromotion can easily be compensated in all three directions for each individual set of electrodes. The downsides are that compared to a two layer trap the trap depth is weaker given the same voltage and distance from the ion to the electrode, and it is slightly more difficult to build, due to the extra layer. This geometry will be discussed more extensively in chapter 5.

3.6 The surface trap

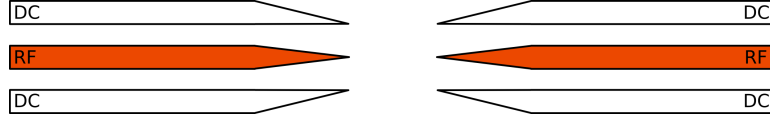


Figure 3.16: This cross section shows a three layer trap with angled electrodes, similar to the gold-on-alumina T trap. The middle electrodes have RF applied to them and the top and bottom electrodes are RF grounded and segmented so they can have static voltages applied. The three layer trap is particularly suited for compensating micromotion in each segment of the trap.

A special type of linear trap is the surface trap. It differs from the three types of linear traps listed above (except the single layer wire trap with alternating RF and DC electrodes) in that its electrodes are not placed symmetrically about the linear RF node. As seen in figure 3.17, the RF node lies above the plane of electrodes, requiring that either backside holes be etched for laser access or lasers be brought across the surface. It offers the possibility of easy fabrication and also eliminates a topological problem with “through traps” in which the laser is brought through a hole in the substrate. The problem with through traps is that if they are part of a large array with many junctions, there will be islands of disconnected trap electrodes. A possible solution for through traps would be to etch areas under the electrodes which allow for ion trapping but do not have a through hole allowing laser access. The surface trap gets around this by trapping the ions above the surface. As a downside, however, one must be more careful not to illuminate ions other than the intended ones. One design consideration for the surface trap is that the principal axes must be rotated so that one axis is not perpendicular to the surface of the trap (see figure 3.17). In the case where laser cooling beams come across the surface of the trap, the ion cannot be cooled if one of its principal axes is perpendicular to the surface and therefore the cooling beam.

3.7 Computer simulations of electric fields from electrodes

As mentioned previously, CPO 3D was used for most of the simulations performed in the course of this thesis research. While the design interface is somewhat clunky

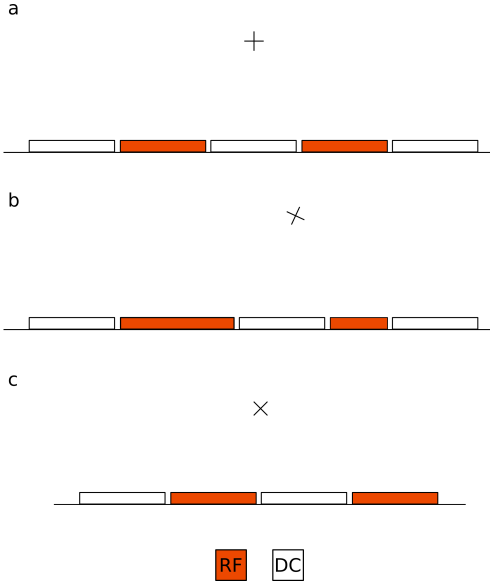


Figure 3.17: Surface trap

Three types of surface traps are shown here, along with the position and principal axes directions denoted by an “X”. In part **a** the trap comprises two RF electrodes placed on either side of a center DC electrode, around which are two more DC electrodes. With zero volts on the DC electrodes this would give us a principal axis perpendicular to the surface of the trap, but this can be rotated by applying an appropriate amount of DC voltage. Part **b** offers another solution to the principal axis problem by making the RF electrodes different widths. Part **c** solves the problem by having four electrodes instead of five, breaking the symmetry and therefore having principal axes at 45 deg to the perpendicular of the trap.

until one gets used to it (see figure 3.18), the speed and accuracy of the simulations makes up for this deficiency. A few examples of simulations are shown in figures 3.19, 3.20, and 3.7. While analytic solutions are available in many cases of linear and surface traps [39], the flexibility of a simulation often makes it more practical for complicated geometries which lack symmetry. Analytic solutions, on the other hand, are particularly useful for problems which require minimizing a certain parameter, such as the change in the secular frequency with ion position ([40], section 7.1). Otherwise a simulation would require a trial and error approach to find a solution.

CPO can output the electric field or electric potential on a 2D or 3D grid. We typically used two dimensional arrays of data in the transverse plane and one of the axial planes. A set of “basis” static potentials for each electrode was compiled by applying one volt to a particular electrode, grounding the rest, and outputting the potential

in the plane of interest. This was repeated for each electrode (taking advantage of symmetry to reduce the number of simulations when possible), allowing a total static potential to be calculated from the linear sum of these, with coefficients depending on the voltage applied. The ponderomotive potential was calculated by applying one volt to the RF electrodes in the simulation and then outputting the electric field on a grid and solving the pseudo-potential equation 3.14 (the micromotion component is ignored). This was then scaled by V^2 for the case of different voltages and added to the static potential solution to find the total potential of the ion. Intermediate potential values between the grid point are determined using Mathematica's Interpolation function. A more detailed description of how the CPO data is actually used can be found in section 7.1.

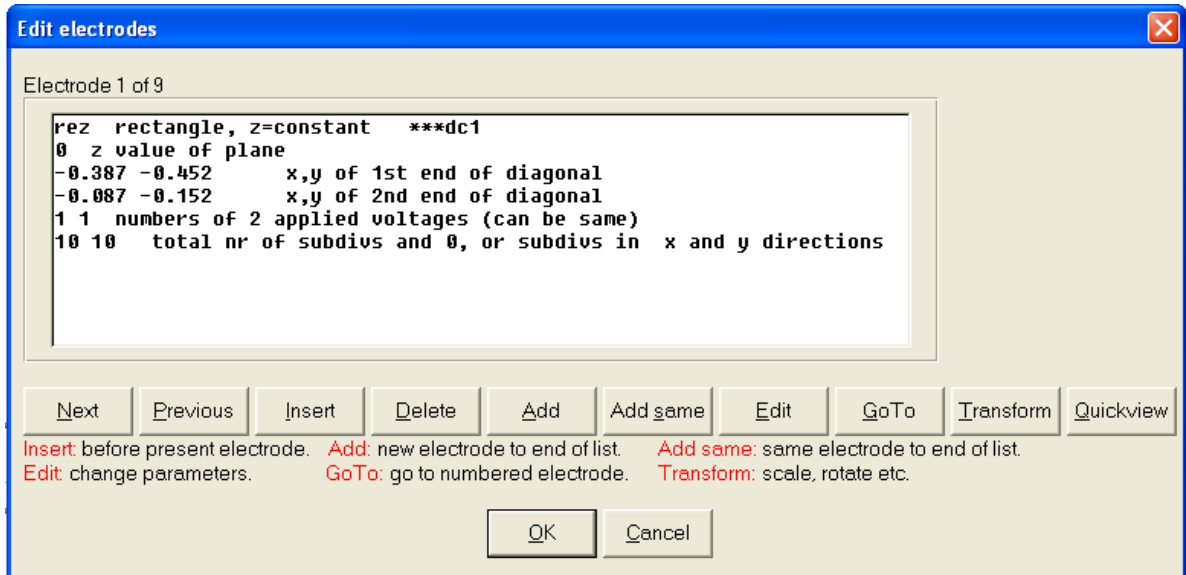


Figure 3.18: The CPO user interface for defining electrode geometries consists of a library of standard three dimensional shapes (including two dimensional surfaces) which can be tailored to a particular electrode geometry. This example shows a flat electrode parallel to the z plane, with the (x,y) coordinates of two corners specified. The "numbers of 2 applied voltages" line specifies the address of the voltage applied to the entire electrode, which is defined in another dialog box. The "total nr of subdivs" line specifies how CPO should subdivide the electrode into regions; each of these regions will have a distributed charge. Having more regions increases the accuracy of the simulation, but also increases the computing time required to arrive a solution.

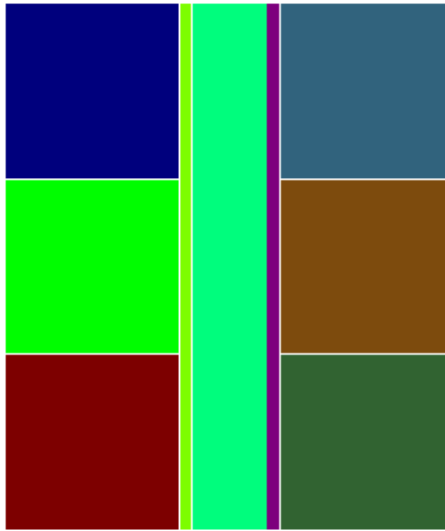


Figure 3.19: This is an overhead view of a surface trap modeled in CPO. The outside squares are static control electrodes, the long rectangular electrodes are the RF electrodes (which are raised $10\text{ }\mu\text{m}$ above the surface of the trap, and the central electrode is for applying static voltages.

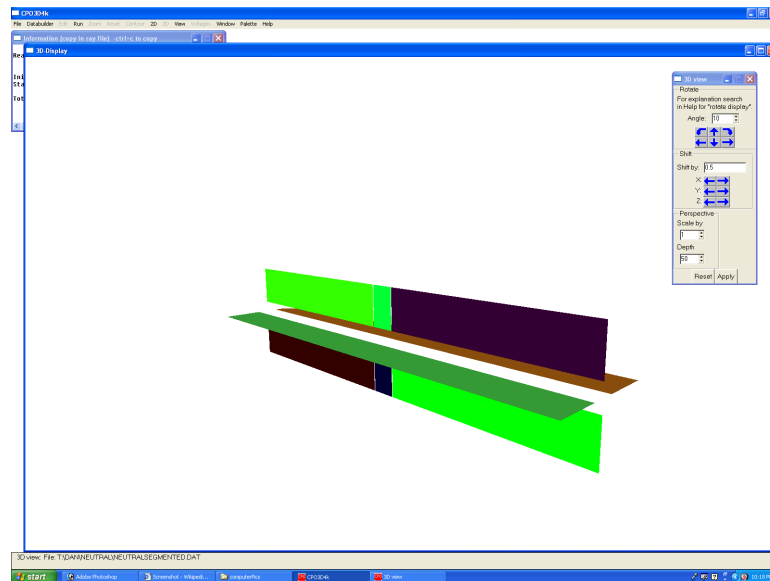


Figure 3.20: This linear ion trap consists of segmented rectangular electrodes at 90° to form a linear trap. The distance from the electrode edge to its neighbor is 2 mm , allowing for clear optical access for MOT cooling beams for a neutral trap. CPO was a useful tool in this situation because it gave an accurate prediction for the amount of RF and end cap static voltages necessary to have a particular strength trap.

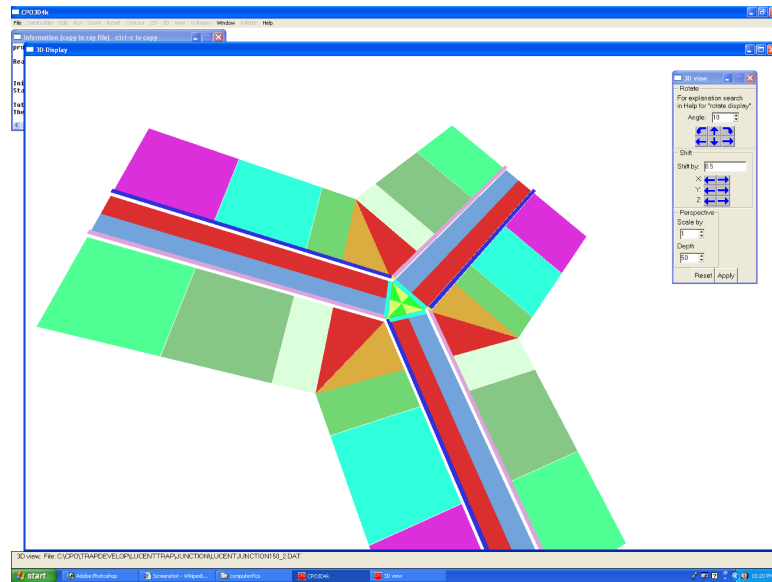


Figure 3.21: This trap is an example of a more elaborate design for a surface trap junction. Computer simulations are particularly useful in the cases of traps without a simple symmetry, as is the case here. In this idea, the triangular electrodes at the junction are static control electrodes which can be switched according to which way the ion is meant to turn. The three rectangular electrodes on the sides of the central triangle are switchable between DC and RF voltage depending on the direction the ion needs to be shuttled.

CHAPTER 4

Experimental setup

This chapter will detail the main components of our experimental setup, many of which are common to all trapped ion experiments.

4.1 Achieving ultra high vacuum (UHV)

Our vacuum chambers (see figure 4.1) are operated at UHV pressures, ideally below 10^{-11} torr. This level of vacuum is achieved by using only UHV compatible materials, primarily stainless steel (316 or 304), tungsten, oxygen free copper, gold, quartz, fused silica, kapton insulated wire, ceramics, Vespel SP3, and PEEK, along with a variety of other specialized materials. If screws with blind holes are used, notches are cut in the threads to prevent virtual leaks from the trapped volume. All of the parts are cleaned in an ultrasonic acetone bath and rinsed with methanol and sometimes isopropyl alcohol. Powder free latex gloves are used at all times when handling vacuum components that are going in the chamber. All solid stainless steel parts (not viewports or feedthroughs) are prebaked at 400 °C for a few days to form an oxide on the stainless steel which limits outgassing.

4.2 The bake

The pump-out occurs in multiple stages. First the air in the chamber is evacuated with a turbopump (Pfeiffer TSU 071) down to about 10^{-6} torr. All of the components which will have high current running through them during normal operation (such

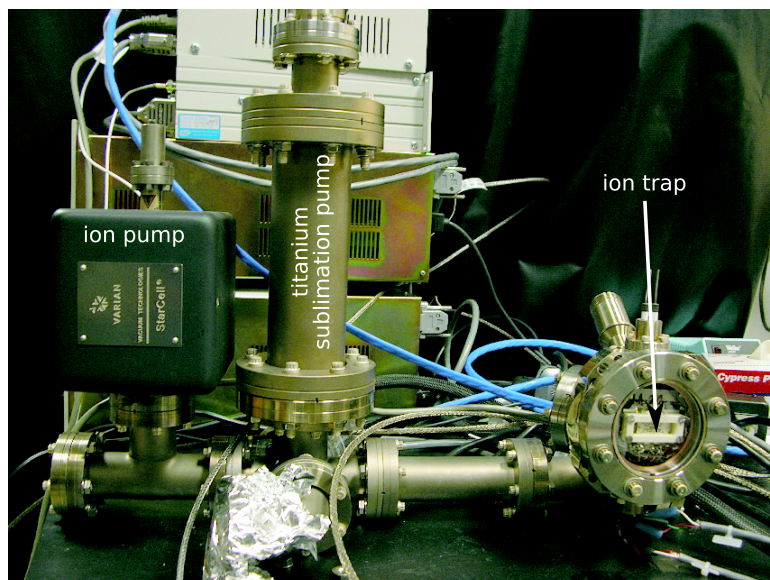


Figure 4.1: This picture shows a typical vacuum chamber consisting of a hemisphere (or spherical octagon) which holds the ion trap itself, a titanium sublimation pump, and an ion pump. Other components that are not labelled here include the bakeable valve, the viewports for laser beam access, and the feedthroughs for electrical interconnects.

as the oven filaments, the ion gauge filament, and the titanium sublimation pump filaments) are degassed at a lower current for a short period of time (for instance, the Ti-Sub pump filament is run at 35 amps for 20 minutes). After this we begin the bakeout in an industrial oven which allows for even heating of the chamber without using heater tape. The oven is initially turned on at 200 °F and brought up a maximum of 30 °F every three hours. At 230 °F the valve connecting the chamber to a 500 L/s ion pump (Perkin Elmer 500 STP) is opened, and the valve connecting the turbopump is then closed. The temperature ramp is continued at the same rate till 392 °F (200 °C is reached, and the pressure on the ion gauge monitored for the next few days. This maximum temperature is set by the maximum bake temperature on the fused silica/quartz windows (MDC 450020), and in particular the PbAg brazing used to seal the viewport to the stainless steel. These windows are chosen for their relatively high ($\sim 90\%$) transmission at 214 nm when anti-reflection coated. Otherwise sapphire windows which can be baked to 400 °C would have been used. When the pressure bottoms out (typically in the high 10^{-8} to low 10^{-7} torr), the 20 L/s internal

ion pump (Varian Starcell) is turned on, and the bakeable valve that connects both the 500 L/s ion pump and the turbopump is hand tightened. It is important not to tighten it so hard that it deforms the copper gasket inside. The 500 L/s pump remains pumping the other side of the bakeable valve. After a few more days at 392 °F the pressure bottoms out to the high 10^{-9} to low 10^{-8} torr and the temperature is ramped down by about 30 °C every three hours. Once the chamber reaches room temperature the bakeable valve is tightened to the prescribed torque with a torque wrench (the torque is increased 2 ft-lb's after every bake), with the 20 L/s pump left running continuously. Finally, the titanium sublimation pump is run usually 10 - 20 times for 2 minutes each at 45 amps till the pressure decreases to below 10^{-11} torr. The whole process typically takes a week.

If the chamber does not pump down to this level, there is either a non-UHV compatible part inside or a leak on the outside. The outside leak is the easiest to diagnose, and if the culprit can be identified to be a viewport (which it usually is) the offending part can be replaced quickly and the bakeout repeated in about half the time as before (as it was not exposed to the air for long). If the pressure is greater than $\sim 5 \times 10^{-10}$ torr, it can be found either by blowing helium around the chamber and looking for a spike in the pressure or squirting acetone around the gaskets and looking for a drop in pressure (as the acetone plugs the leaks). If the leak is lower than $\sim 5 \times 10^{-10}$, it might be necessary to squirt methanol around the gaskets and wait for 10 - 20 minutes to see if the pressure decreases. Leaks this small are difficult to see with the acetone and helium tests, as the acetone evaporates too quickly to see an effect and the helium would have to be directed at the same spot for several minutes to register on the pressure gauge.

4.3 The chamber

Our chambers are constructed with off-the-shelf confocal flat components from Kimball physics and viewports from MDC. Our machine shop has also made some custom pieces for us requiring titanium alloy welding. As mentioned above, each

chamber has a 20 L/s ion pump which runs continuously, and a titanium sublimation pump which is run intermitantly as needed. For the part of the chamber in which the ion trap is contained we have used a single Magdeburg hemisphere (MCF450-MH10204/8), a Magdeburg hemisphere plus a spherical octagon, and a single large spherical octagon (MCF600-SO200800) from Kimball physics. In all of these cases the largest available viewport was used for imaging and the others for laser access.

For traps which require fewer than ~ 30 DC control voltages, MDC multipin instrumentation feedthroughs are used, which can have between 2 and 35 pins which connect to push on connectors. A two pin high voltage version of this feedthrough is used for the RF electrodes in all of the chambers. For the semiconductor fabricated microtraps, more control electrodes are needed, and so the type D instrumentation series connectors were chosen, with PEEK ribbon connectors and Kapton coated wires used for connections inside the chamber.

The microtraps impose some fairly exotic requirements on the chamber, given the number of leads and the need to swap new traps in and out of the chamber. For this task we chose to use a 100 pin CPGA (ceramic pin grid array) from Global Chip Materials (PGA10050001) to attach the ion traps; 50 of those pins were hooked to DC control signals and 2 to RF. The other pins remained empty. The socket they were plugged into was made out of Vespel SP3, a UHV compatible plastic from Dupont, although other groups have had success with PEEK as well. This is an easily machinable material (see the technical drawing for this in figure 4.3) which offers good mechanical stability for the socket. Gold plated receptacles were used to connect to the pins on the CPGA (part number 0672-4-15-15-30-27-100 from PCS Electronics). Due to the initial difficulty of pushing the CPGA into them, each receptacle was “annealed” with a .016 inch diameter stainless steel wire in them at 450 °C for 1.5 minutes. They were placed on a ceramic plate which sat on a nichrome wire in a nitrogen purged box. After this process the receptacles were strong enough to make repeatedly good contact but not so hard that they were difficult to put on. They were then crimped to the Kapton coated wire with a Paladin PA1440 crimper. The entire socket and chip carrier assembly, along with its mounting block and ovens, can be seen in figure 4.3.

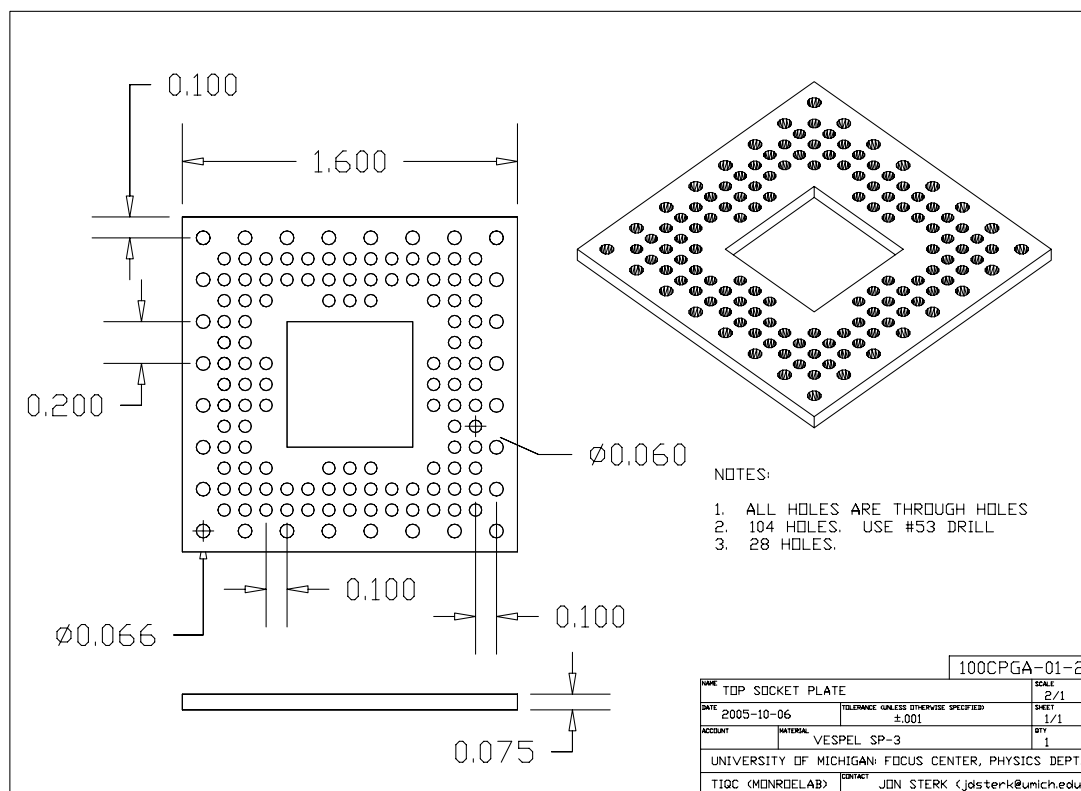


Figure 4.2: This figure (courtesy of Jon Sterk) shows the physical dimensions of the custom made socket used for connecting to the 100 pin CPGA chip carrier. It was fabricated out of Vespel SP3, which was chosen for its strength, flexibility, RF properties, and UHV compatibility. Two of these pieces would be used to sandwich 50 receptacles for contacting the CPGA pins (the other pins were not hooked up).

These components were mounted in the chamber with custom made brackets and groove grabbers from Kimball physics (see figure 4.3). The trap when attached to the CPGA sat less than 5 mm from the inside surface of the viewport. Depending on the trap, a hole could be drilled in the back of the ceramic chip carrier for optical access from the backside.

4.4 RF resonator

High voltage (100 V - 2000 V) is delivered to the trap via an HP 8640 function

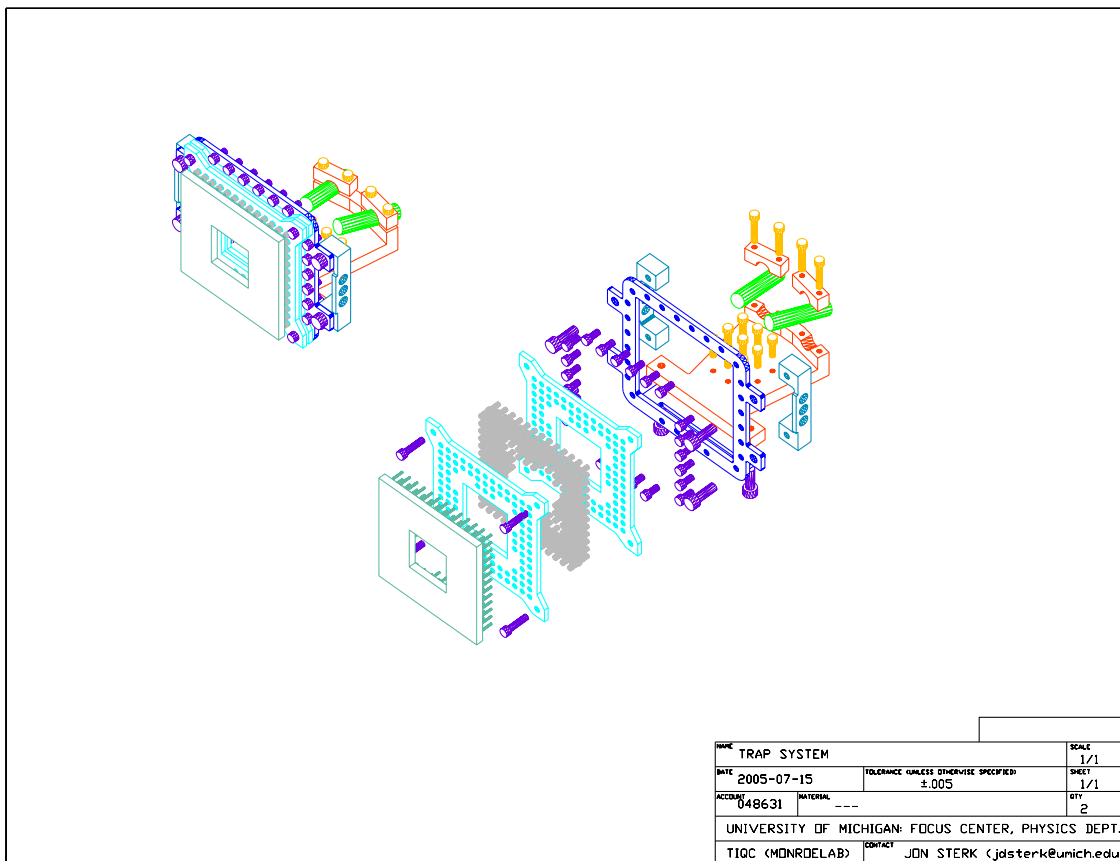


Figure 4.3: This figure shows the entire UHV compatible CPGA socket assembly and mounting block. The exploded view at the bottom right shows the chip carrier going into the vespel sockets, which sandwith 50 recepticles between them (shown in gray). The sockets connect to a mounting assembly which also holds the Cd ovens and mounts to the vacuum chamber via groove grabbers.

generator, an RF power amplifier, and an RF resonator used for impedance matching the trap (an open circuit with some capacitance to ground) to the power source. Since the circuit is open and there is little current flowing (depending on the capacitance), the loaded Q can be quite high, and so deliver a high voltage to the trap with minimal input power. There are multiple kinds of RF resonators, one of which is the coaxial variety consisting of a single wire in the middle of a conducting can. An antenna at the bottom (opposite the load) which is oriented so as to generate magnetic fields circularly about the central wire is used to couple RF power into the resonator. The resonant frequency of this apparatus is $\lambda/4 = \text{length of the inner wire}$. At 50 MHz, the

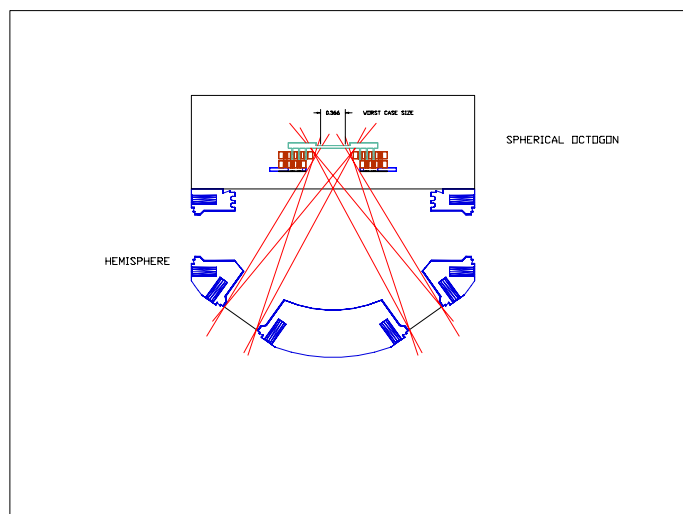


Figure 4.4: This overhead view of the vacuum chamber shows the laser access to the ion trap which is afforded by the 1 1/3 inch viewports that are at 60° to the large 4.5 viewports normal. A 4.5 inch spherical octagon is attached to the front (top in the picture) of the hemisphere so that the reentrant viewport used for imaging can be close to the trap, and to add extra room for mounting structures and wires.

frequency we usually operate our ion traps at, a 1.5 m inner wire would be required, which is unwieldy and impractical. Instead we use a helical coil, as described in [41] and figure 4.4. This uses a coiled inner copper wire with a copper outside can, where $\lambda/4$ is roughly the length of the coil, but also depends on a number of other parameters, such as the diameter of the coil, the gauge of the wire, and the diameter of the can. We typically use a 3 inch copper pipe for the can and make the helical coil out of 10 gauge copper wire, which is coiled about 10 times with a diameter of about 1.5 inches. Power is coupled into the can with an antenna at the top such that the magnetic field generated will circle around the wire coil. These resonators typically have loaded Q's of between 300 and 500, and the voltage on the trap is then $V = 20\sqrt{PQ}$, where the constant 20 is dependent on the exact geometry of the resonator. The Q can be increased by cleaning the inside of the copper can, as dirt inside increases power loss. The resonator is critically coupled to the trap by moving the antenna in and out till the reflection disappears on resonance.

Sometimes a DC bias needs to be applied to the RF. In that case, the top end of

the coil, which is usually capped with a BNC and grounded to the can, has a low pass π filter attached to it. At this point a static voltage can be applied without affecting the Q , as long as the capacitor is high enough $\geq .1\mu\text{F}$ that the RF is effectively grounded here. There are also times when two signals with the same RF but different static voltages need to be applied to the trap. In this case we make a bifilar resonator consisting of two coils which run right next to each other inside the resonator can. This is made easier if we use a piece of teflon with holes drilled in it to space out and support the two separate coils; otherwise it is difficult to keep them from shorting to each other. The teflon does not significantly hurt the Q of the cavity. We put a large ($\geq 1\mu\text{F}$) capacitor between them at the output to ensure that the phases of RF are the same. Two separate π filters can then be attached to the opposite ends of the coils.

RF power can also be coupled into the resonator capacitively. By attaching a variable capacitor near the output of the helical coil and applying RF voltage at the can's resonant frequency the trap can be impedance matched to the RF source. The resonator is critically coupled by tuning the variable capacitor. This type of resonator was used for the GaAs trap, with an additional variable capacitor attached across the output leads to allow for tuning the resonant frequency. The GaAs trap was unique in that it could only tolerate 10 - 15 volts RF and had high loss and a subsequently low (~ 50) unloaded Q . The RF could have been applied without a resonator, but it was useful because the trap was operating on the edge of its tolerable voltages, so that if the trap itself heated up from power dissipation the resistance of the GaAs changed and the cavity drifted off of resonance. This would reflect some of the power back to the RF source and lower the voltage across the trap, protecting it from catastrophic voltage breakdown.

4.5 Ovens

A vapor of neutral cadmium is generated by heating an atomic source (either a single isotope or natural source) in an oven which is generally pointed at the trap

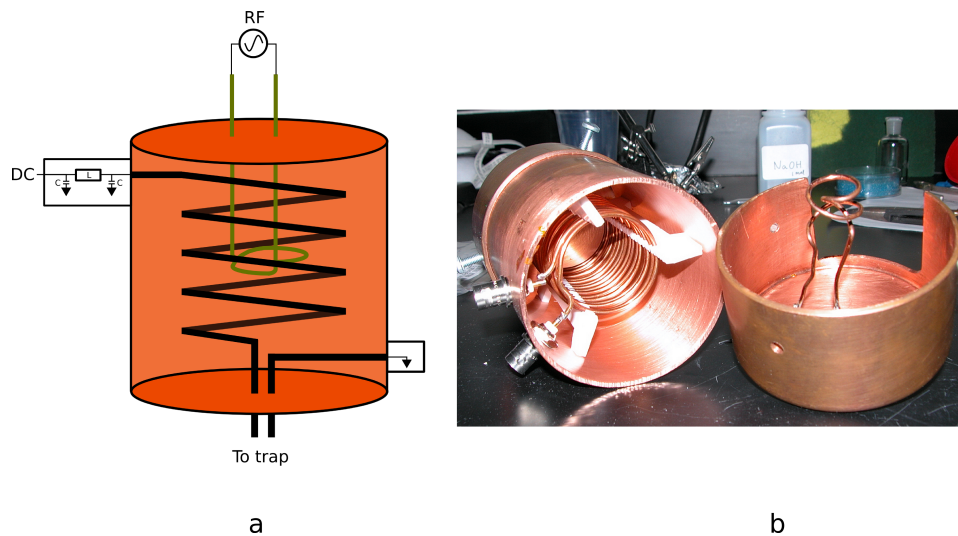


Figure 4.5: Part **a** diagrams a schematic of the cavity resonator used to impedance match the trap to the amplified RF source, without which most of the power would be reflected or go into heating a parallel $50\ \Omega$ resistor. In the schematic we see the RF source at the top driving a “pigtail” coil. The magnetic fields generated by this pigtail couple into the larger coil and produce high RF voltages at the bottom, when the drive frequency is on resonance. The outputs of the resonator are the RF high wire and a grounded wire, which is shorted to the outside of the resonator. The upper part of the main coil is RF grounded to the can. By attaching a π filter we can apply a DC bias to the RF hi which does not significantly effect the Q of the resonator. In part **b** we see an actual resonator, made from a section of 3 inch diameter copper pipe, endcaps, and a coil of 10 gauge copper wire. The copper should be polished with a brillo pad or stainless steel, or even chemically with hydrochloric or phosphoric acid, to improve the Q and minimize RF loss on the inside of the can. All open holes in the can should be covered with copper tape.

region. Our early experiments used metallic Cd packed in an oven made of a stainless steel tube with one end open. The tube was heated by running current through it, which was sufficient to vaporize the Cd (boiling point $769\ ^\circ\text{C}$ at 1 atmosphere). The downside to this method was that during the $200\ ^\circ\text{C}$ bakeout the metallic Cd would coat the inside of the chamber, giving the gold trap electrodes a dull metallic tinge. In the worst case this can short out electrodes, and is of a particular concern for small traps in which the distance between adjacent electrodes is short. It is also blamed for increasing the electric field noise coming from the trap electrodes [42].

Over the course of building several Cd traps it was realized that firing the ovens was not necessary for trapping. The room temperature partial pressure of Cd is $\sim 10^{-13}$ torr, just below the base pressure of the vacuum chamber. This is ideal from a trapping standpoint; for most of our strong traps, once we got them working the first time and aligned the lasers and imaging optics, we never had to fire the ovens again, relying on the background vapor pressure to load from. This made Cd well suited for testing shallow traps, since we did not need a directed source of Cd targeted at the trapping region which could contaminate or short the electrodes.

In more recent traps we have substituted metallic cadmium for cadmium oxide. With a much higher boiling point (1559°C), the CdO does not contaminate the chamber during the bakeout. It does require a hotter oven to generate the initial Cd vapor, but once that has been achieved, it is similar to the metallic sources in that we do not have to fire the ovens and can just load from the vapor. This hotter oven (see figure 4.5) consists of a ceramic tube about .1 in in diameter with tungsten filament wrapped around it. The CdO is packed in the tube, which is sealed at one end with either uranium glass or a ceramic paste, and a smaller aperture is pasted to the other end. This prevents the CdO from hardening while it is heated and shooting out of the oven like a bullet. By running about 1 amp through the 10 - 20 coils of tungsten wire we can get a significant amount of Cd vapor. The ovens (both metallic and oxide) were tested in a bell jar to find both the current which produces a visible spot on the glass and also the current at which the residual gas analyzer registers a noticeable increase in Cd vapor ($\sim 10^{-9}$ torr). When working with cadmium, particularly the oxide whose particulate constituents can easily be breathed in, it is important to wear personal protective equipment like gloves and a HEPA air filter mask. Cadmium is a known carcinogen which is highly toxic if one is exposed to high doses.

4.6 Photoionization

Before we used photoionization of the neutral Cd vapor, electron guns consisting of a negatively biased filament ($\sim 100\text{V}$) through which current was run and a grounded



Figure 4.6: This figure shows two cadmium ovens, made out of a ceramic tube with tungsten wire coiled around each tube for heating them. The red material seen on the inside is cadmium oxide. Typically an oven like this would also have a small ceramic aperture at the front to make sure the cadmium oxide does not fall out.

accelerator plate were used to direct a stream of ionizing electrons into the trapping region. While ultimately effective, this method was inefficient, ionized all particles including air molecules, and contaminated the system and raised the ambient pressure. Replacing this with a photoionizing laser improved performance in all these areas. By focusing the a pulsed photoionization beam in the trapping region, all isotopes and velocity classes of Cd can be ionized and the loading rate increased to above 1 s^{-1} [43].

In Cd, the ionization process requires a two photon transition from the $5s^1S_0 \rightarrow 5s5p^1P_1$ state and then to the continuum (see figure 4.6), where the photoionization excites the ion 1.84 eV above the threshold. This scheme can be generally applied to many of the other ion QC candidates, including Be, Ca, Sr, Ba, Mg, Yb, and Zn, with the exception of Hg which would require a 185 nm laser. The flux of photoionized atoms is determined from the number of atoms in the focus of the beam at the location of the trap, the size and depth of the trap, the time required for a π Rabi rotation from the ground state to the intermediate state due to the photoionization beam, and the probability of the transition to the continuum based on the cross section of the intermediate 1P_1 state. Both the pulsed beam and the detection beam can be used to excite the ion from the intermediary 1P_1 to the continuum, but the higher peak intensity of the pulsed laser makes it the dominant contributor. The final loading rate is calculated to be $\sim 4\text{ s}^{-1}$ for our laser setup, which is consistent with observations.

We use a mode-locked Ti-sapphire laser centered at ~ 915 nm with a ~ 10 nm bandwidth that produces 100 fs pulses at an 86 MHz repetition rate. The Ti-sapphire is pumped with 4.7 - 5 W of 532 nm light from a Spectra-Physics Millennia pump laser, and requires excellent thermal contact and cooling in order to run at this wavelength, due to the high gain in this region. A pair of Brewster cut fused silica prisms are used to compensate for the group velocity dispersion, and the laser is tuned by cutting off a portion of the separated spectrum after the prisms. The output light is frequency doubled first by focusing through a 7 mm long LBO crystal and then doubled again through a 5 mm long BBO crystal. Both are crytically phase matched through angle tuning. The final output power ranges from 4.5 mW to 6.5 mW. The output beam is highly astigmatic and slightly elliptical; we tried correcting for this with an anamorphic prism pair and cylindrical lenses, but found that the best way to get a tight focus at the trap was to minimize the distance from the doubling crystals to the trap.

4.7 Lasers and frequency modulation

While cadmium is an excellent qubit choice from an atomic physics perspective, it is technically difficult due to its short wavelength UV transitions. Most of that hardship therefore falls on the laser and frequency modulation systems. For the trap development experiments we need a detection/cooling beam at 214.5 nm, an initialization beam (which uses the cooling beam), a Raman transition beam (whose wavelength choice depends on the output power but which we detuned by 70 GHz from the $^2S_{1/2} - ^2P_{3/2}$ transition), and a photoionization beam at 228.9 nm, as described in the section above.

The detection and cooling beams come from the same laser (see figure 4.7); they differ only in the frequency applied to the AOM. The cooling beam is most efficient at a quarter linewidth below the atomic transition, while the detection beam is most efficient at the peak of the atomic transition. They both use the same AOM, and are switched via an RF switch that changes the frequency source from a 185 MHz source

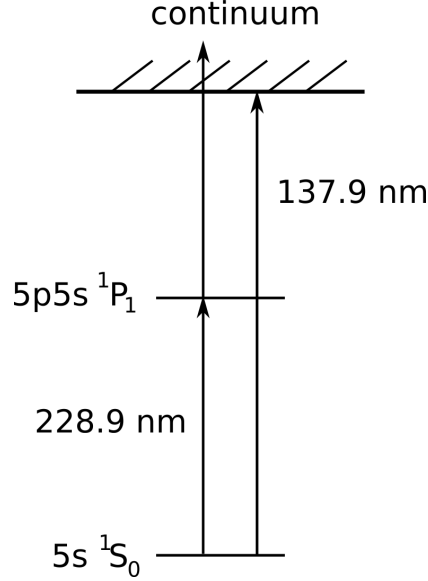


Figure 4.7: This diagram of the photoionization energy levels shows the two photon process which excites an electron from its ground state $5s\ ^1S_0$ ground state level to the intermediate $5s5p\ ^1P_1$ level and then up to the continuum. The first transition can be excited with the pulsed laser, while the second can be excited by either the pulse laser or the CW cooling laser, although the much higher intensity of the pulsed laser makes it the dominant contributor to this process.

(cooling) to a 200 MHz source (detection) as needed. The laser itself is a Toptica TA 100 continuous wave diode laser which goes through a tapered amplifier to produce ~ 700 mW of tunable power. This goes into a Toptica SHG 110 cavity which uses an LBO crystal for second harmonic generation, which puts out ~ 110 mW of 429 nm laser power. An EOM after the first doubler puts on 6.85 GHz sidebands, which are doubled to 13.7 GHz in order to pump the 111 isotope out of its dark state via the $^2P_{3/2}$ F=1 state. The last stage is a Wavetrain CW frequency doubling cavity from Spectra-Physics, which uses a temperature controlled BBO crystal to generate ~ 1 mW of 214.5 nm light. The output of this goes into a AOM which splits the beam into a cooling/detection part and an initialization part. Since the initialization beam is tuned between the $^2P_{3/2}$ F=2 and F=1 levels, it must go through a double pass AOM at 400 MHz; since it is already 200 MHz below the cycling transition, an additional 800 MHz puts it 600 MHz above the F=2 transition. This corresponds to the maximum initialization efficiency. The cooling/detection beam gets upshifted

by 185 or 200 MHz out of the AOM, depending on whether the cooling or detecting portion of the experiment is run. It also goes through a polarizer and quarter wave plate so that only σ^+ light is generated for the cycling transition.

In between the two doublers in the Doppler cooling beam path is a tellurium vapor cell used to lock the frequency of the doubling lasers, compensating for frequency shifts due to mechanical vibrations or temperature drifts. Locking this laser is important for accurate measurement of the cadmium lineshape and for having efficient detection of the qubit state. The $^{130}\text{Te}_2$ cell is wrapped in heater tape to keep the cell at $\sim 470^\circ\text{C}$ and further wrapped in insulation to minimize temperature gradients. About 5 mW of power from the blue light coming out of the first doubler is diverted into a double pass AOM (Brimrose TEF-1000-300-429) at 900 MHz to match the difference in the $^2S_{1/2} \rightarrow ^2P_{3/2}$ (the negative first order is used). This beam then gets split into a pump beam, a probe beam, and a reference beam, with about 90% of the power in the pump beam and the rest split between the other two. The probe and reference beams go in through the same side, with the difference that probe overlaps the pump beam. The pump beam goes through an additional AOM centered at 80 MHz and is swept ± 2 MHz about the center frequency at a 20 kHz modulation frequency. The reference beam and probe beams are then input into a New Focus Nirvana auto balancing photoreceiver. The output of the Nirvana detector is the error signal, which gets fed into external frequency scan of the Toptica laser.

The Raman beam path is similar to the previously described one. We use a Coherent MBR Ti:Sapphire laser, pumped by a 10 W Millennia Pro diode laser, to generate 1.5 W of 858 nm light. This gets doubled twice through two Wavetrains, with an EOM between the two. The EOM adds sidebands at half the hyperfine splitting, allowing Raman transitions between the $|\uparrow\rangle$ and $|\downarrow\rangle$ internal states. The first AOM deflects the first order of the beam into a photodiode which feeds back into the AOM via a mixer with the incoming RF in order to suppress power noise on the laser. The zeroth order goes through, and after an AOM becomes Raman beam 1. The zeroth beam also goes through an AOM and a pair of mirrors on a moveable mount, such that the path length of Raman beam 2 can be varied. This is the Mach-Zehnder

interferometer, and is required so that the contributions of the EOM sidebands do not interfere and cancel the Raman transition.

Before going further, let's calculate the affect of the EOM on the UV output of the laser [44]. The effect of an EOM (driven by an oscillating source of $V \sin(\omega_{HF}t)$) on an optical field of $E_0 \cos(kx - \omega_L t)$ is [45]:

$$E_1 = E_0 \cos(kx - \omega_L t + \phi \sin(\omega_m t)) \quad (4.1)$$

$$= \frac{E_0}{2} e^{i(kx - \omega_L t)} \sum_{n=-\infty}^{\infty} J_n(\phi) e^{in(\delta k \cdot x - \omega_{HF} t)} + c.c. \quad (4.2)$$

In the above equations the modulation index ϕ depends on the voltage amplitude V , $J_n(\phi)$ is the n th order Bessel function of the first kind, and $\delta k = \omega_{HF}/c$. In the doubling cavity, in which the free spectral range is carefully tuned to be $1/4$ of the modulating frequency $\omega_{HF}/2$, all the sidebands are allowed to resonate simultaneously. The nonlinear crystal in the cavity allows second harmonic generation equal to $E_2 = \chi^{(2)} E_1 E_1$, or inserting equation 4.1:

$$E_2 = \eta \frac{E_0^2}{4} e^{2i(kx - \omega t)} \sum_{n=-\infty}^{\infty} J_n(2\phi) e^{in(\delta k \cdot x - \omega_{HF} t/2)} + c.c. \quad (4.3)$$

where η is the harmonic conversion efficiency which absorbs the non-linear term $\chi^{(2)}$. Ideally we would be able to apply this optical field and drive stimulation Raman transitions (SRT) using all pairs of spectral components separated by ω_{HF} , but because J_n obeys the relation $J_{-n} = (-1)^n J_n$, all of these terms destructively interfere and the net Rabi frequency goes to zero. To solve this, we employ a Mach-Zehnder interferometer, in which one of the beams has a path length difference of Δx . The Rabi frequency then becomes:

$$\Omega = \frac{\mu_1 \mu_2 \langle E_2 E_2^* e^{i\omega_{HF} t} \rangle}{\hbar^2 \Delta} \quad (4.4)$$

$$= \Omega_0 e^{i\delta k(2x + \Delta x)} \sum_{n=-\infty}^{\infty} J_n(2\phi) J_{n-2}(2\phi) \cos(2k + (n-1)\delta k)\Delta x \quad (4.5)$$

where μ_1 and μ_2 are the matrix elements for the qubit states and the excited state,

and the base Rabi frequency $\Omega_0 = \mu_1\mu_2/(\hbar^2\Delta)|\eta E_0^2/4|^2$. For $\delta k\Delta x = (2j+1)\pi$, j an integer, the Rabi frequency can be a maximum of $\Omega = .487\Omega_0$ for $\phi = .764$. This is the reason for the moveable mirror pair seen in figure 4.7. One problem one can see from equation 4.4 is that because of the $k\Delta x$ term, interferometric stability is required to maintain a constant Rabi rate. This problem is solved by introducing a relative frequency shift of $\Delta\omega \gg \Omega$ between the two Raman beams, which is compensated for by tuning the EOM $\pm\Delta\omega/2$. The two AOMs in the Raman beams are responsible for this relative frequency shift (we use $\Delta\omega = 2\pi \times 4$ MHz). The resulting Rabi frequency is:

$$\Omega = \Omega_0 e^{-i(k\Delta x + 2\delta k \cdot \Delta x)} \sum_{n=-\infty}^{\infty} J_n(2\phi) J_{n-2}(2\phi) e^{in\delta k \cdot \Delta x} \quad (4.6)$$

This gives us a maximum SRT Rabi frequency of $\Omega = .244\Omega_0$ for integer j terms of the path length difference above. In essence this relative frequency shift causes the Raman beam to be a travelling wave, such that changes in the path length do not change the Rabi frequency. Since the wave is travelling, however, the Rabi frequency is now half what it would have been in equation 4.4. This is an acceptable loss in Rabi frequency however, in that it enables well controlled Raman transitions. From the perspective of quantum information, however, it is disappointing, since only about half the power of each Raman beam ($.5 \times .5 = .25$) contributes to the Rabi frequency, whereas all the power can contribute to spontaneous emission and AC stark shifting. For more information on the atomic physics of Raman transitions, see chapter 2.

4.8 Imaging system

We collect the fluorescence from the ion using the imaging system shown in figure 4.8. The objective lens is a triplet from CVI (UVO-20.0-10.0-193-248) coated for UV optics with $f/2.1$ and a 14.8 mm focal length. Simulations of our optical setup in Oslo have shown us that given the thickness of the viewport and the free space distances between the ion and the objective lens, we need to be $17 \pm .1$ mm from the ion to the objective in order to have a diffraction limited image in which 85% of

the emitted fluorescence is in the central spot of the Airy diffraction pattern. For instance, at 17.3 mm, the power in this spot goes down to 50% of the overall power, and resolving two ions in the same trap becomes more difficult. This issue does not affect data collection, however, since the PMT counts total power. We put a 400 μm pinhole after the lens to cut out scattering on the electrodes. A doublet lens is then used to focus the image on the CCD camera or PMT, which are about 60 cm away. The overall magnification of our system is ~ 250 and the resolution is about 1 μm , allowing us to distinguish between two ions in a trap, which for the case of a 2 MHz trap is about 3 microns.

We calculate the solid angle of the objective lens from the object distance and f number, and see that about 3% of photons are collected. When we are looking at the trap features or for the presence of an ion, we use a Princeton Instruments PI-MAX intensified CCD camera, with a quantum efficiency of $\sim 2\%$. While this is adequate for diagnostics, it is too slow (15 ms readout time) and the background noise too high for high fidelity experiments. This camera has been used, however, in an experiment requiring simultaneous detection of two ions in the same trap, recording 98% detection fidelity (compared to 99.7% fidelity for a single ion with a PMT) [23]). For typical data collection a Hamamatsu H6240-01 photomultiplier tube (PMT) was used, with a quantum efficiency of $\sim 20\%$ and 35 ns resolution. Factoring in other losses gives an overall collection efficiency for the PMT imaging system of $\sim .3\%$.

4.9 Instrument control and data collection

We use LabView to control and time all of the instrument instructions during the course of an experiment. By sending TTL pulses to RF switches (Mini Circuit ZFSWA-2-46) we can switch RF power on and off to the amplifiers that drive the AOM's and EOM's, and therefore switch beams on and off the ion, as well as quickly change their frequencies. The logic card that sends the TTL pulses is a National Instrument PCI-6534 pulser card with 32 channels and a 20 MHz clock rate. Its on board 16 MB of memory is more than sufficient for storing the heating measurement

experiments that we typically run. In addition to triggering the RF switches, the pulser card also signals the counter card (National Instrument PCI-6602) to count PMT photon counts during the specified window. Frequency scans are performed via a GPIB controlled Stanford Research Systems DS345 function generator. In some experiments [46], phase stability between Raman pulses in a Ramsey experiment is crucial, and this is accomplished by phase locking all of the relevant synthesizers with a single SRS function generator's 10 MHz clock signal. This stability is not necessary for the heating measurement experiments described later in this thesis.

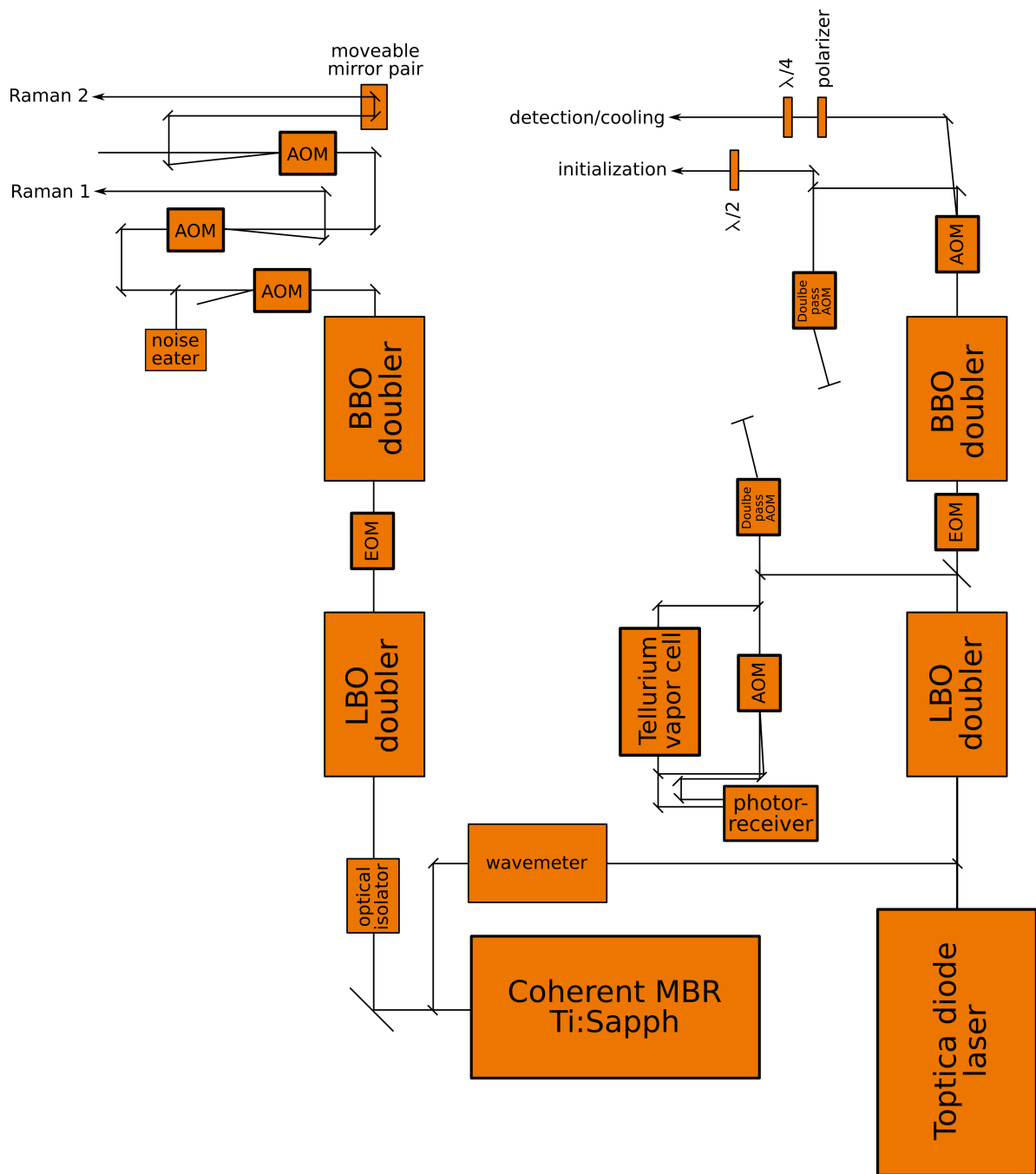


Figure 4.8: This diagram shows the entire laser setup for the experiments here, with a few optical elements (such as lenses) excluded for clarity.

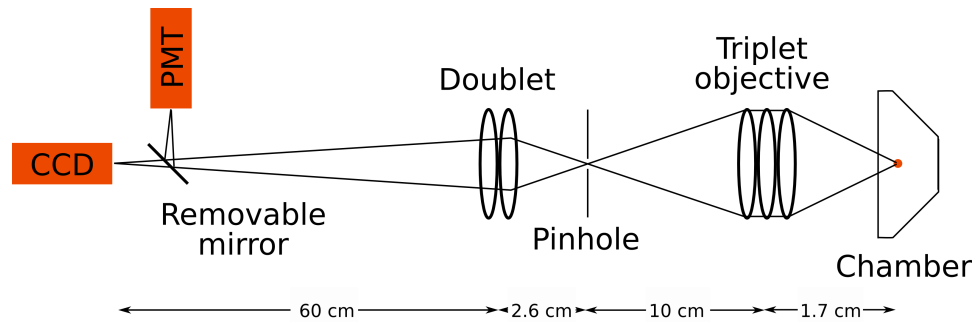


Figure 4.9: The imaging system of the experiment consists of a $f/2.1$ triplet lens which collects the fluorescence of the ion. This light gets focused through a pinhole (which is useful for eliminating background scattering from the electrodes) and then goes through a doublet lens which focuses the image on either the CCD camera or the PMT, depending on whether the flip mirror mount is up.

CHAPTER 5

Scalability: Demonstrating junctions in the T trap

One of the DiVincenzo criteria for a quantum computer specifies that the architecture must be scalable. This has different meanings for different QC implementations, and for some systems it is a selling point and for others it is a hurdle. For many of the solid state implementations, the scalability criteria is a natural extension of the lithographic fabrication methods used to make individual components, like Josephson junctions or quantum dots, for instance. There are plenty of considerations one would have to account for, like increasing noise or power dissipation with increasing component density, but the possibility of fabricating many components on the same structure is not difficult in principal. For trapped ion systems, scalability is an issue. The techniques used to fabricate traditional ion trapping structures are not amenable to making either large numbers of individual ion traps nor to making them small. To fulfill the DiVincenzo requirement, however, an ion trap array must be able to hold a large number of ions, and in addition must be capable of moving them around to interact with each other as part of controlled gate operations. This chapter will focus on the ability to shuttle an ion, specifically my research on the “T” trap [47].

Moving ions has already been demonstrated in an RF trap, where researchers at NIST [48] shuttled ions in a straight line with near unit efficiency a distance of 1.2 mm, as well as separated two ions in the same trap into separate traps. The shuttling was done with negligible motional heating while preserving the internal state of the ion. The separation introduced significant heating; as the voltages were changed in order to bring the potential up between the two ions, the trap frequency by necessity decreased. Since there is more electric field noise at lower frequencies, this led to

greater heating. In addition, just the act of changing the potential of the trap itself contributes to the motional heating of the ion. A possible solution to this is to make smaller electrodes, which allows for greater control over the potential at the ion such that the separating potential could be brought up faster and more precisely to minimize the change in trap frequency that the ion experiences.

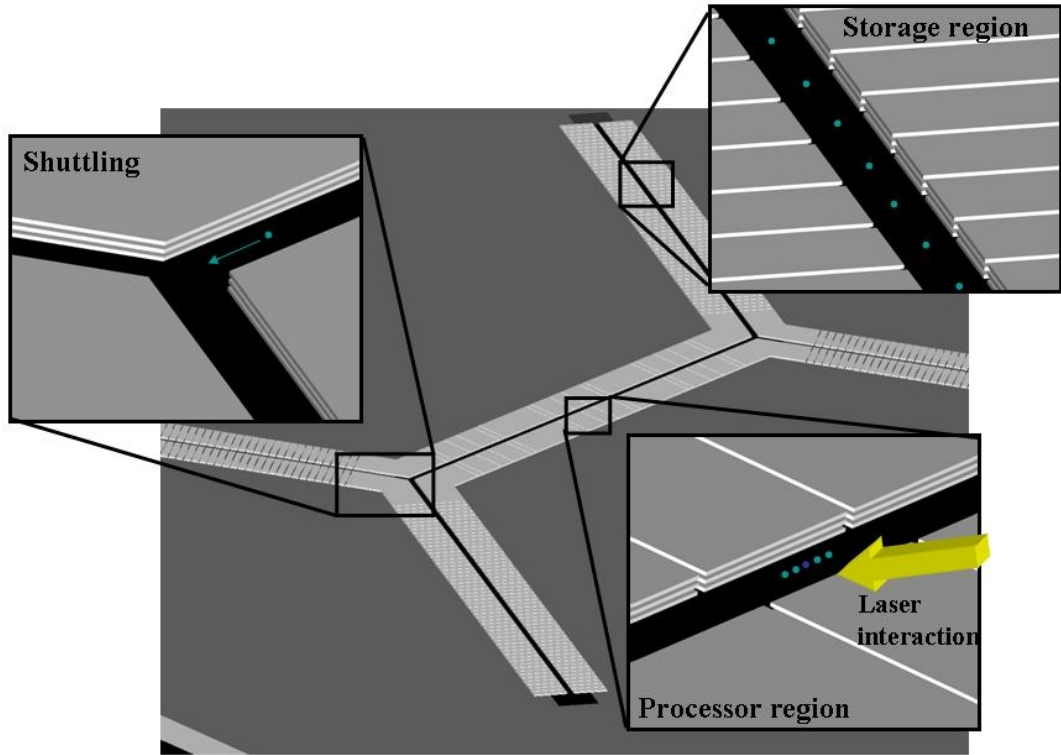


Figure 5.1: This schematic shows a portion of a large scale trap array, highlighting several different specialty regions. There is a storage region for holding the ion qubits, a processor region for laser interaction and gate operations, and a shuttling region comprising a “Y” junction.

Transporting an ion along a line does not completely fulfill the requirement of being able to shuttle an ion to an arbitrary position in a trap array. In a two dimensional ion trap topology, junctions in which three or more RF nodes intersect are needed for moving ions around each other (see figure 5.1). From a technical standpoint this

is not a trivial problem, as often times junctions introduce axial RF potentials, manifested as humps which push the ion away from the intersection. Therefore larger quasi-static fields are needed to push the ion through the intersection, which must be tailored to minimize heating while in the junction [49]. Not only must the voltages be tailored, but the shapes of the electrodes in the junction region must be chosen so as to minimize this RF hump.

Our approach to this problem was to make a trap dedicated to demonstrating ion shuttling through a junction. We first considered a two layer trap geometry, with a cross junction. While this structure generates strong trapping potentials in the linear portions of the trap, in the junction region it does not trap in the direction perpendicular to the plane of the electrode layers. This problem can be overcome by connecting one RF electrode to its diagonal neighbor with another electrode, both on the top and bottom [39]. This solution works in the case of the gold on alumina traps, which are hand assembled, but since the bridge goes in a different direction on the bottom layer this would not be possible to fabricate lithographically. Since we wanted this experiment to serve as a proof of principal shuttling experiment, we wanted the geometric shape to be realizable in a microfabricated trap, even though we were going to use conventional gold on alumina structures. This led us to settling on a three layer design, as seen in figures 5.2 and 5.3.

Figure 5.2 shows an overhead view of the whole T Trap. The ceramic layers are gold coated to form the electrodes, and all three layers are held together via rectangular alumina mount bars. Chip capacitors and resistors are ribbon-bonded onto a gold coated quartz plate. To suppress electric noise on the control electrodes a low pass filter consisting of a 1 nF capacitor and 1 k Ω resistor is connected to the leads coming off the trap. Figure 5.3 shows a zoomed in view of the junction, with an inset of an RF hump, or axial RF force, which impedes the ion from moving into the junction region. All three of these humps have $\Delta E \sim .1$ eV, therefore requiring that the control electrodes push the ion into and out of the junction region.

5.1 T trap fabrication

In order to make the ceramic T trap, we had to be able to get thin gold wires out from the cantilevers back to the bond pads. Since physical masks cannot be made small enough for this, we used physical masks to coat the cantilevers up till the grooves (so they didn't short) and photolithography and a liftoff to bring the wires out to bond pads. After multiple failed attempts at doing the photolithography with conventional photoresists, a solution using dry film photoresist was discovered.

5.1.1 Photolithography

There were a few competing problems in laying down the gold with photolithography. For one, it was difficult to prevent gold from sticking to the insides of the laser machined grooves and shorting adjacent cantilevers. One attempted solution was to spin a thick layer of photoresist first to fill the grooves and a second layer of photoresist to do the lithography on top. This first photoresist is baked for a long time and then squirted with acetone briefly, followed by methanol and isopropyl. Squirted acetone for a short time only removes the photoresist on the surface of the ceramic, not in the grooves. This technique is successful in that the photoresist stayed in the grooves, but it didn't really solve the problem since Au bridges on top of the photoresist still shorted adjacent cantilevers.

Another problem is the second photoresist. For one thing, the photoresist tends to be thicker right where the cantilever goes from sloped down to flat (figure 5.4). The problem with this is that the sample has to be left in the developer longer than normal to get rid of the thick part, and then other parts which need to stay but are thinner come off. Also, there is an edge bead (figure 5.5) around the sample that prevents wires from being within about 2 mm of the edge. These problems can be somewhat alleviated by spinning the photoresist on faster. This, however, introduces the problem that the photoresist is now not thick enough where the grooves meet the surface, so that shorts will develop there (figure 5.6).

Setting the acceleration of the spinner is also difficult. If accelerated too fast, "rays" of photoresist form that radiate from the holes used to line up the ceramic

pieces (Figure 5.7). These rays are ripples in which the thickness of the photoresist varies, and it is hard to develop it evenly without leaving it in the photoresist too long. If accelerated too slow, however, edgebead problems tend to arise.

5.1.2 Dry film photoresist

After using liquid photoresist and failing to evaporate the electrodes without shorting them, a process using a dry film resist was finally determined to eliminate the problem of shorting Au bridges in the laser machined grooves. The dry film resist we chose was a 100 μm thick resist called Riston, from DuPont. It consists of a peel layer for protection, under which is a UV curable viscous film that can be developed in an alkaline solution. In general the advantage of dry film resists over liquid resists is that they can be quite thick (up to a few hundred μm), they can be applied to large surfaces without the need for spinning and with achieving a uniform thickness over the entire wafer, they have a relatively long shelf life, they require low exposure intensities, and they can be developed without the use of environmentally hazardous solvents. The downside to using these photoresists is that the minimum feature size achievable is significantly lower, as dry film resist are usually thicker than 25 μm .

Dry film photoresist was used here because it could be laid over a ceramic structure with vertical features (the grooves and angled edge of the trap electrodes) without becoming too thick or too thin. This is not a feature normally required in other dry film photoresist applications, as the surfaces they protect are generally flat. The downside to the dry film photoresist is that it tends to leave a residue behind after being developed. Cleaning in acetone, with a plasma asher, or in acids did not totally eliminate the residue. To solve this problem, a layer of ebeam resist was first spun on top of which the dry film resist was placed. The ebeam resist could be easily removed with acetone, and so would not leave a residue behind.

The first processing step was to spin on 950 AZ ebeam resist at 4000 rpm onto the ceramic substrate. A piece of blue tape was used to hold it to the vacuum chuck, since the holes in the ceramic prevented it from being held with vacuum pressure.

The ebeam resist was then baked at 180 °C for 7 minutes. Then the dry film resist was laid on top of this; any air bubbles that got trapped underneath had to be pushed out with a qtip. The sample was then be exposed to a mercury lamp (12 W/cm³) for 1.3 seconds. This time is critical, as the dry film resist is so thick that diffraction of the exposing light can cause erosion of the edge of the dry film resist. The sample was developed in 1.5% NaCO₃ for 75 s, and rinsed in DI water and acetone to remove the exposed ebeam resist.

In any evaporation it is critical that the surface be clean. Dirt will prevent the Ti and Au from sticking to the surface, and prevent a nice smooth metal surface. Using an ebeam evaporator (see section 6.5.5), 150 angstroms of Ti followed by 4000 angstroms of Au were deposited. The Ti is important for getting the Au to stick. A rotating planetary orbital was used so that the metal was evaporated onto the surface at different angles, covering the edges of the electrodes. The thickness of Au is not too important, as long as it covers the entire surface. The liftoff process requires an overnight soak in hot acetone, after which it should be cleaned with methanol and IPA.

At this point it was necessary to test for shorts with visual inspection and a multimeter. Most shorts could be removed by laying down a piece of tape over the surface and peeling it off. Any gold that was not attached to the surface (like a shorting bridge) would likely come off with the tape. Of course, there are occasional irreconcilable defects. In this case, the Au was removed with aqua regia and the Ti with HF. The remaining clean alumina was reused and the process attempted again.

5.2 Trap layout and electronics

The T trap dimensions were restricted by the minimum gap that could be laser machined in the trap corner, since multiple leads had to come out of this region. This gap spacing of 25 μm as well as the length of the gap, set a minimum size of the corner electrode of 800 μm . The rest of the dimensions of the T trap can be seen in figure 5.8.

The voltages applied to the T trap were controlled with three National Instruments cards (NIC 6733) whose -6 to +6 volts output were sent to operational amplified circuits (Apex PA85A) with a maximum slew rate of 10 V in 1 μ s. The voltages could be switched from 0 V to the maximum in about 10 μ s. As in other experiments, a National Instruments pulser card was used for triggering the PMT to collect shuttling and separation statistics. An example of a voltage file used can be seen in figure 5.9, which shows the voltage routine corresponding to shuttling an ion from trap zone d to zone i. Moving the ion into the junction region involves simultaneously raising the voltage on electrodes 6, 7, 26, and 27 to 200 V, lowering 9 and 16 to -2 V, and raising 8 and 17 to 0 V. The shallow potential in the junction requires minimal heating of the ion, and so the voltages are varied relatively slowly ($\sim 20\mu$ s). The last step requires raising electrodes 16 and 17 to 10 V while lowering 8 and 9 to -10 V, trapping the ion in zone i.

5.3 Shuttling results

Shuttling an ion around the corner, from the stem to the top of the T, could be repeated with nearly 100% success (881/882 attempts), but when the ion came around the corner it was sufficiently hot that it does not crystallize till the Doppler beam cooled it down. Simulations show that the ion acquires about 1.0 eV of kinetic energy going through the junction. A recipe for the voltages applied to actually shuttle the ion can be seen in figure 5.9, with the electrode layout shown in figure 5.8. A reversed voltage sequency took the ion back to its original starting point with 98% fidelity (out of 118 attempts). The whole sequency took 20 ms.

Our primary proof of principal experiment was reversing the position of two ions, which can be distinguished if they are different isotopes. We did this by trapping two ions in the same trap, separating them, shuttling one around a corner, shuttling the other to the other corner, and then moving them back in the reversed order. To split the ions, we had to lower the axial secular frequency to ~ 20 kHz, and then raise the middle electrodes up to split them apart. This took about 10 ms and only had

58% fidelity in 64 attempts because the middle electrodes were too big to accurately and repeatedly split the ions apart. As a comparison, at 20 kHz the ions are about $50\text{ }\mu\text{m}$ apart from each other. However, the central electrodes used to split them are $400\text{ }\mu\text{m}$ wide. The recombination fidelity was also not perfect, and so the whole ion switching routine only achieved 24% fidelity (51 attempts).

5.4 T trap lessons

The results of the T trap point to several important lessons. For one, the necessity of making lithographically fabricated chips with on board filtering circuits is a necessity for hosting a large number of ions. Manually constructing filter circuits is prohibitive in its space requirements. Secondly, a lithographically fabricated structure would be well aligned, as opposed to the manually aligned T trap. Our manual alignment resulted in the center electrode being about $50\text{ }\mu\text{m}$ off from where it should have been. While this did not prevent trapping, it did introduce an asymmetry into the corner turning problem, as evidenced by the fact that we could only shuttle the ion in one direction. If we wanted to go in the other direction, a left turn, say, we would have had to make a right turn and then shuttle the ion through the junction. Finally, the low success probability of the splitting component shows that we need smaller electrodes to be able to manipulate an ion as precisely as is necessary. When the ratio of the ion separation to the electrode width is small, splitting two ions apart is a low fidelity process, as the T Trap showed.

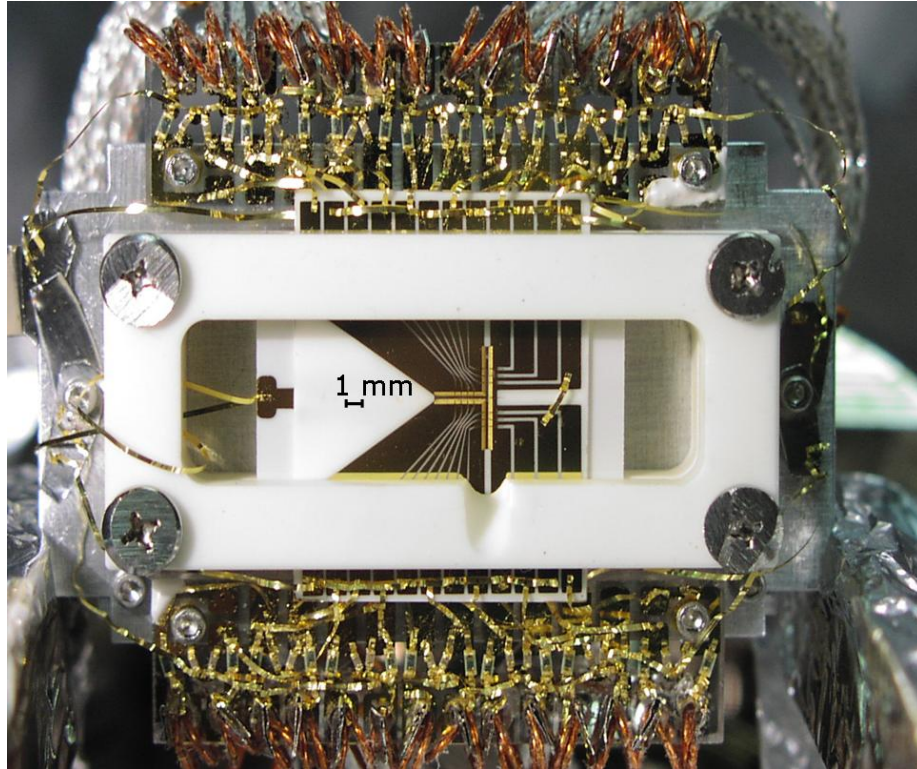


Figure 5.2: The T trap electrodes are gold sputtered onto a laser machined, polished alumina substrate, with two segmented substrates (the quasi-static electrodes) sandwiching a continuous RF electrode. There are four sets of electrodes in the stem of the T (each $400\ \mu\text{m}$ wide), a larger corner electrode ($800\ \mu\text{m}$ wide), and three more electrodes ($400\ \mu\text{m}$ wide) on each side of the “T” (which is laying on its side). Each set of electrodes consists of 2 quasi-static electrodes on each side of the trapping node, with an RF electrode in between them. The gap between electrodes is $200\ \mu\text{m}$. Above and below the trap itself are gold ribbons which connect to filtering circuits, and then connect to outside, Kapton insulated leads.

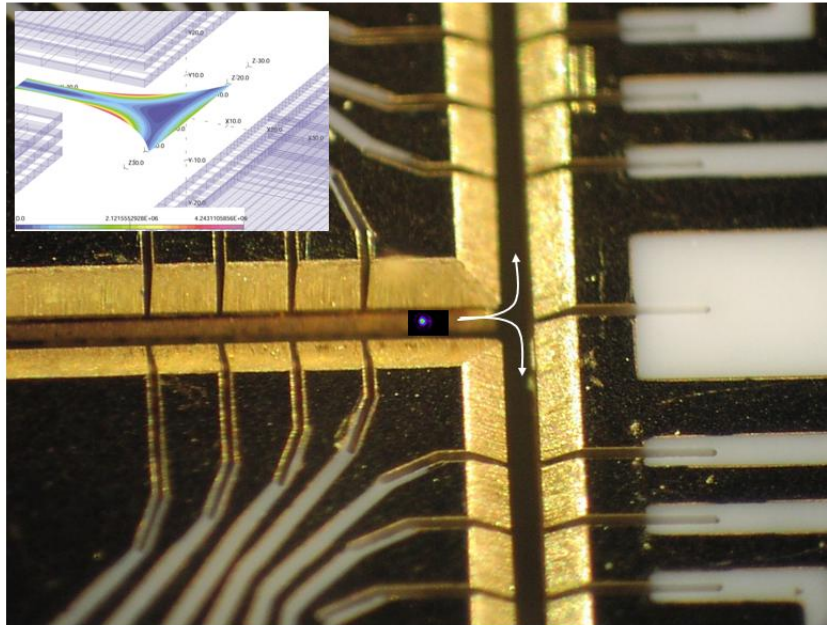


Figure 5.3: This picture shows a zoomed in view of the T trap junction. The inset region shows a simulated potential for the junction region, displaying the RF hump through which the ion must travel to get from the stem of the T into the junction.

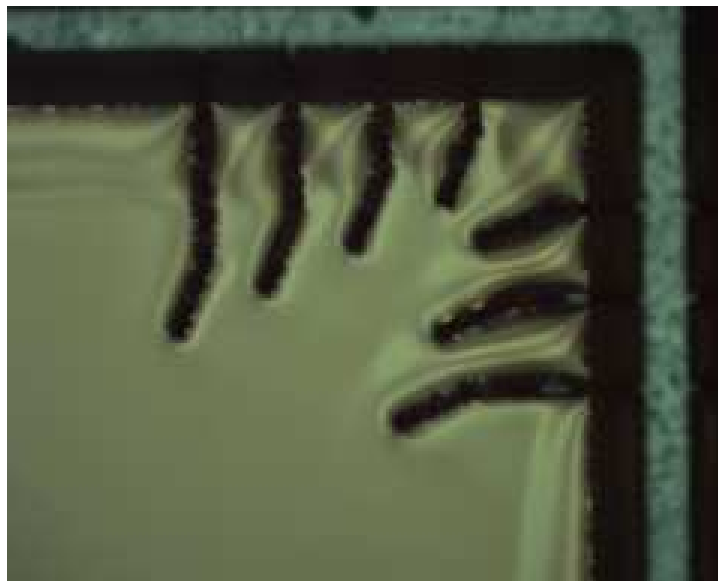


Figure 5.4: This picture shows how the photoresist does not evenly coat the cantilevers, but has thicker photoresist near the edges.

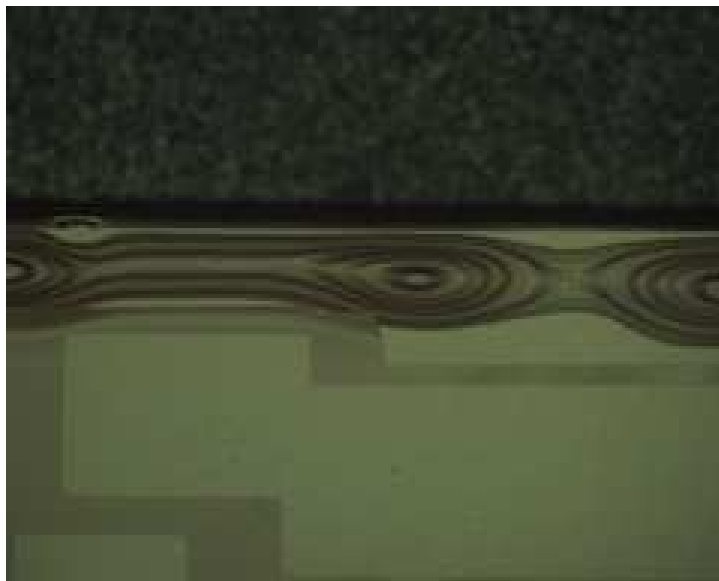


Figure 5.5: Because of the thicker edgebead, photoresist that should have been developed off remains (the ovals at the top).



Figure 5.6: Since the photoresist had to stay in longer to develop the edges and cantilevers (you can still see some on the right corner cantilever), some of the photoresist between two wires came off (see the left corner cantilever).

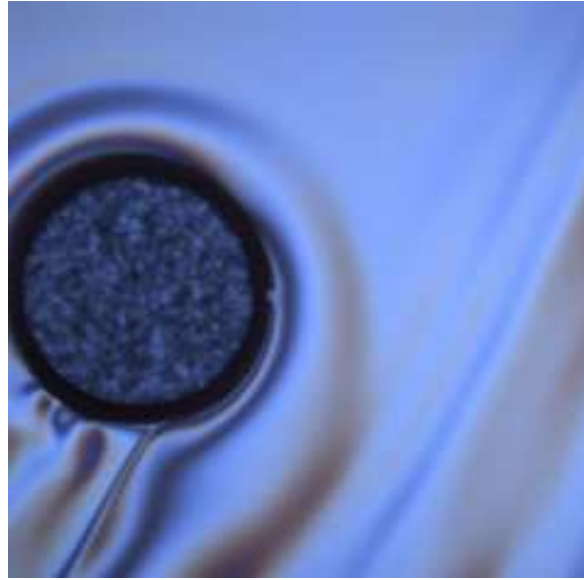


Figure 5.7: The photoresist radiating to the bottom left of the hole has uneven thicknesses.

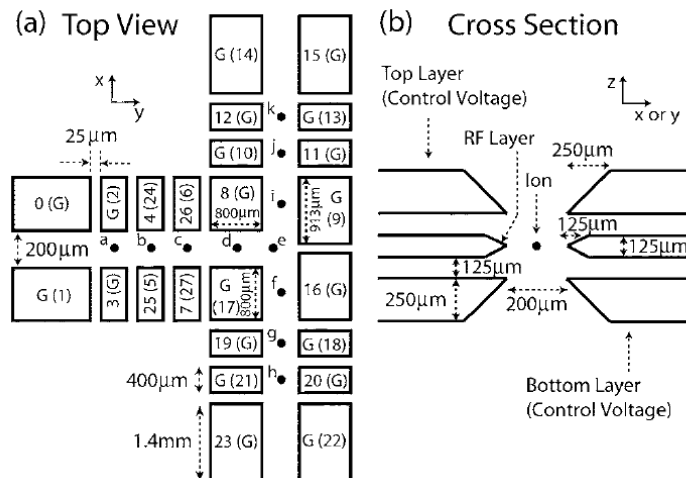


Figure 5.8: T Trap dimensions

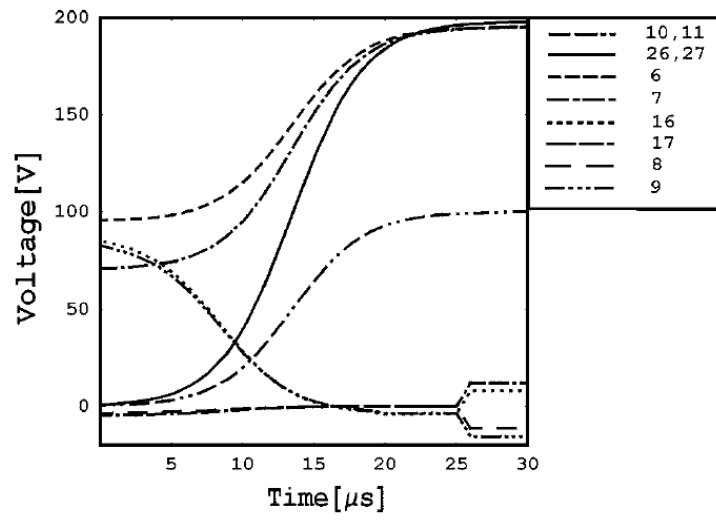


Figure 5.9: T Trap voltage

CHAPTER 6

Scalability: Demonstrating a microfabricated gallium arsenide trap

There are multiple factors one has to consider in the design and fabrication of a semiconductor ion trap. By virtue of the size and materials used, many of these considerations are not relevant for more conventionally fabricated traps. Some of these conventionally fabricated traps are constructed out of metal sheets or rods at least a hundred microns thick, with air gaps and ceramics insulating the high voltage RF from the RF grounded electrodes. Others use gold deposited on alumina as the electrodes. In each of these the conducting electrodes have little resistive loss, the capacitance between the electrodes and ground is low and therefore little current is drawn, and the insulating layers are thick and well suited to holding off large voltages. In contrast, many of the microfabricated traps use less than ideal conductors, either by virtue of their thickness or the material properties. The resistive losses in these traps can be significant, especially given that the current flowing can be considerable if the capacitance is high between the RF electrodes and the RF ground. This is not an unusual situation given that many fabricated devices have limited vertical dimensions, due to the restrictions on oxide or nitride growth, or MBE deposition. Electrodes that have a large ratio of lateral dimensions to their vertical dimension tend to have large capacitances. These smaller vertical dimensions also lead to higher electric fields across insulators, making voltage breakdown more of an issue compared to conventionally fabricated traps.

6.1 Mechanical characterization

The first consideration in the fabrication of these devices is their mechanical stability and the bending of the cantilevers under the applied voltage [37]. Based on the dimensions shown in figure 6.2, the spring constant of each cantilever can be calculated [50]

$$k = E \frac{t^3 w}{4d_s^3} \quad (6.1)$$

where E is the Young's modulus of the GaAs, t is the thickness of a cantilever, and d_s is the length of the cantilever which is suspended ($d_s \ll d$). The force on the cantilever due to an applied voltage can be calculated by considering the force between two plates of a parallel plate capacitor:

$$F = -\frac{\partial U_{capacitor}}{\partial d} \quad (6.2)$$

$$= -\frac{\epsilon_0}{2} \frac{\partial}{\partial d} \left(\frac{w d_s V_0^2}{h} \right) \quad (6.3)$$

$$= \frac{\epsilon_0}{2} \frac{w d_s V_0^2}{h^2} \quad (6.4)$$

An upper bound for this deflection can be calculated by assuming that all of the force occurs at the tip of the cantilever, which is treated as a spring with spring constant given by equation 6.1. The maximum tip deflection x_d is

$$x_d \approx \frac{2\epsilon_0 d_s^4 V_0^2}{E h^2 t^3} \quad (6.5)$$

Plugging in the typical dimensions for our GaAs cantilevers ($E = 85.5$ GPa, $h = 4 \mu\text{m}$, $t = 2.3 \mu\text{m}$, $d_s = 15 \mu\text{m}$, and $V_0 = 10$ V), gives $x_d \approx 5$ picometers, a negligible amount compared to the vertical separation h .

Another concern is the resonant frequency of the cantilever; even if its motion is minimal, it can still have a large effect if it is resonant with the secular frequency of

the ion. The resonant frequency for a cantilever is

$$f_{vib} = .162\sqrt{E/\rho}\frac{t}{d_s^2} \quad (6.6)$$

where ρ is the density of the material (5.31 g/cm^3 for GaAs). The resonant frequency of the single layer cantilever suspended out by d_s is $f_{vib} \approx 6 \text{ MHz}$. If the two layers are considered as a whole, where they are suspended out a length $d_s \approx 100 \text{ }\mu\text{m}$ from the anchoring substrate, this resonant frequency is $f_{vib} \approx 600 \text{ kHz}$.

While these frequencies are potentially troublesome if they overlap with the secular frequency, they are ignored due to the expected high Q of the resonator. From similar measurements of a GaAs/AlGaAs cantilever [51] conducted in vacuum (eliminating air dampening), we expect $Q > 10^3$. The likelihood of the secular frequency and a mechanical resonance overlapping is therefore extremely low.

6.2 Power dissipation

The effects of power dissipation in GaAs, and more broadly that of a voltage breakdown dependence on frequency, are topics beyond the scope of this thesis. The important criteria to note are that the band gap of AlGaAs decreases with increasing temperature [52], as well as the observation that voltage breakdown increases exponentially with frequency [53] in other materials. This last reference investigates silicon nitride as opposed to AlGaAs, but the electronic hopping mechanism used to explain the frequency dependence of voltage breakdown could also apply to AlGaAs. If the power dissipation in a trap becomes significant enough to increase the temperature of the electrodes, the resistance of the electrodes can increase, causing a further increase in resistance, and eventual breakdown of the insulating layers. Given the multiple mechanisms related to power dissipation in the electrodes which could lead to breakdown, we consider power dissipation carefully in this section. As an aside, it could also be argued that current flowing in the insulating $\text{Al}_{.7}\text{Ga}_{.3}\text{As}$ layer is the important parameter, in which case a modified argument with qualitatively similar

but slightly different scaling laws would follow.

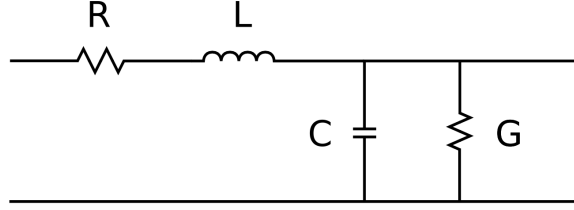


Figure 6.1: The GaAs electrodes can be modelled as transmission line with distributed resistance and capacitance. The self inductance and parallel conductance are small enough to ignore.

The power dissipation in a trap can be calculated from the distributed resistance, inductance, and capacitance of the electrodes. We model this as a completely general transmission line (see figure 6.1). For the GaAs case, the self inductance of a single electrode is $\sim .5$ nH. The resistance (described in more detail later) is $R_e \sim 20 \Omega$ from the bond pad to the electrode tip. The capacitance per electrode is $C_e = 2.6$ pF. Finally, the parallel conductance is $\sim 10^{-9}$ siemens. Calculating the distributed per length values shown in the figure and plugging them into the attenuation and impedance formulae for a transmission line [54]:

$$jk = \alpha + j\beta = \sqrt{(j\Omega L + R)(j\Omega C + G)} \quad (6.7)$$

$$Z_0 = \sqrt{(j\Omega L + R)/(j\Omega C + G)} \quad (6.8)$$

where $j = -i$ follows the electrical engineering convention and the correct roots are the ones with postive real values. In the case of the GaAs trap, for a trap operated at $\Omega \sim 15MHz$, $\Omega L \ll R$ and $\Omega C \gg G$, allowing us to make the simplifications:

$$\alpha = \sqrt{R\Omega C/2} \quad (6.9)$$

$$Z_0 = \sqrt{R/(2\Omega C)} \quad (6.10)$$

The power dissipated over the electrode of length l is then:

$$P_d = \frac{1}{2} \left(\frac{V - Ve^{-\alpha l}}{Z_0} \right)^2 Rl \quad (6.11)$$

$$= \frac{V^2(1 - e^{-\alpha l})^2}{2Z_0^2} Rl \quad (6.12)$$

$$\approx \frac{V^2 \alpha^2}{2Z_0^2} Rl \quad (6.13)$$

$$= \frac{1}{2} V^2 \Omega^2 C_e^2 R_e \quad (6.14)$$

This gives a power dissipation of $\sim 200 \mu W$ per electrode pair. Comparing this with the Q of the cavity resonator on the trap (which has an unloaded Q of ~ 500 that is dragged down by the losses in the trap), we define $1/Q = R_s C_t \Omega + \tan \delta$, where C_t is the total capacitance and $\tan \delta$ is the loss tangent of $\text{Al}_{0.7}\text{Ga}_{0.3}\text{As}$ that is included for generality, although with a value of $\tan \delta \sim .0004$ this is not significant compared to the other terms. This gives us a total power dissipation of:

$$P_d = V^2 \Omega C_t / (2Q) \sim 1.7 mW \quad (6.15)$$

which is consistent with the per electrode pair power dissipation.

6.3 Power scaling laws

As mentioned in the previous section, the power dissipation in a trap is an important parameter to be aware of in that it may impose a limit regarding voltage breakdown. In this section we look at a few scaling laws of the trap, namely how the power dissipated scales with trap depth, secular frequency, and the distance from the ion to the nearest electrode. We will assume a high aspect ratio two layer trap geometry (like the GaAs trap), but this can easily be adapted to other geometries (often with more favorable power scaling laws).

First let's rewrite the secular frequency, trap depth, and stability parameter q :

$$\omega \propto \frac{V}{\Omega d^2} \quad (6.16)$$

$$\Psi_{max} \propto \frac{V^2}{\Omega^2} d^2 \quad (6.17)$$

$$q = 2\sqrt{2}\frac{\omega}{\Omega} \leq .92 \quad (6.18)$$

where V is the RF voltage amplitude, Ω is the voltage drive frequency, and d is the distance from the ion to the closest electrode. Substituting q in the above equations gives us:

$$\omega \propto \Omega q \quad (6.19)$$

$$\Psi_{max} \propto Vq \propto \Omega^2 d^2 q^2 \quad (6.20)$$

These are suggestive ways to write these equations because ultimately our limitation is the size of the stability region since the q parameter must always obey the inequality in equation 6.16. So let's assume that we are at the maximum q value. In this case if we want to increase the secular frequency, we have to raise the drive frequency; if we try to raise ω by increasing the voltage, we've increased the value of q , which is already at its maximum, thereby making the trap unstable.

Now let's say we want to make a smaller trap, and so we shrink the distance $d \rightarrow d/\alpha$, where $\alpha > 1$. In the case of the GaAs trap, this could be accomplished by changing the photolithographic mask to move the electrodes closer together, but keeping the same vertical structure. This would keep the resistance and the capacitance the same as before. In order to maintain the same trap depth, we must have $\Omega \rightarrow \alpha\Omega$, which has the effect of increasing the secular frequency by a factor of α , which is favorable. However, given the power dissipation formula in equation 6.11, we see that P_d has increased by α^2 . In a more realistic scenario, we would want to shrink all lateral dimensions by the same factor α . This would have the effect of $C \rightarrow C/\alpha^2$ and R remaining constant. This would have the effect of the power dissipation actually decreasing by $1/\alpha^2$, or the power dissipation per volume remaining constant.

This analysis assumes that we are in the high aspect ratio regime, where $\eta \approx 1/\pi$. From a technological standpoint, the limitations to this lateral shrinkage lie in the ability to separate adjacent electrodes with chemical and dry etching, and maintain a high electrode width to gap width ratio, so that the trap is truly nearly linear. This is not a trivial problem, as the relatively thick amounts of GaAs/Al_{0.7}Ga_{0.3}As make high aspect ratio etches difficult. Another limiting requirement is that of making interconnects (such as wirebonds) to the electrodes.

6.4 Gallium Arsenide properties and MBE Growth

The bulk of my research was spent designing and fabricating an ion trap built out of gallium arsenide (GaAs). This material was chosen because it was relatively easy to obtain in the desired size dimensions through molecular beam epitaxy (MBE). MBE is an evaporation technique performed in a UHV environment in which the substrate (a GaAs wafer in this case) is heated and the desired deposition materials are controllably evaporated onto it, with a resolution of nearly one atomic layer [55]. MBE growth is a very flexible technique in that nearly any epitaxial layer composition, thickness, and doping concentration can be produced, resulting in layers that are highly uniform across the wafer. The downsides of MBE are that it is expensive and slow; growth rates are typically 1 μm per hour. However, given our access to an MBE grower, we concluded that the flexibility offered and the relative accessibility of material made it the logical choice for fabricating an ion trap.

In our experiment, we started with a highly doped ($\sim 1 \times 10^{18} e/cm^3$) 3 inch diameter GaAs wafer (650 μm thick), on top of which was grown a 4 μm thick layer of aluminum gallium arsenide (AlGaAs), a 2.3 μm thick layer of highly doped GaAs ($\sim 3 \times 10^{18} e/cm^3$), another 4 μm layer of AlGaAs, and another 2.3 μm layer of GaAs. This was the second trap that we tested; the first version was identical but had 2 μm AlGaAs layers, and the trap experienced catastrophic voltage breakdown before an ion was observed in the trap. The silicon dopant levels were chosen to optimize electrical conductivity. The theoretical resistivity of the GaAs is $\rho = \frac{1}{n\mu e}$, where n is

the dopant concentration, μ is the mobility of GaAs, and e is the charge of an electron. The expected resistivity is $2.5 \times 10^{-4} \Omega \cdot \text{cm}$, giving a theoretical sheet resistance of $1.2 \Omega/\text{square}$. Using a four probe measurement (to factor out the contact resistance of the bond pad), the sheet resistance of the electrode was determined to be 7Ω per square. This discrepancy can be attributed to an overestimate of the mobility and defects in the conducting GaAs layers (which increase with higher dopant concentrations). For the final trap ($130 \mu\text{m}$ wide electrodes), the total resistance, including a small ($\sim 1 \Omega$) bond pad contact resistance, was measured to be $\sim 20 \Omega$ from the bond pad to the tip of the electrode.

The AlGaAs was composed of 70% Al, 30% Ga ($\text{Al}_{0.7}\text{Ga}_{0.3}\text{As}$), which was chosen for its insulating properties, its ability to be selectively etched, and its stability (too high a concentration of Al will oxidize in air and will eventually cause problems in the devices). The electrical permittivity for this composition is $10.9\epsilon_0$, giving a theoretical capacitance of the top electrodes to the grounded substrate of 1.25 pF and 1.72 pF for the top electrodes. The measured capacitance per electrode (based on the measured total capacitance) was 2.6 pF . The difference between the theoretical and measured values can be attributed to underestimates of the capacitance in the vacuum chamber feedthrough, as well as between the insulated Kapton wires and the chamber.

The resistance of the $\text{Al}_{0.7}\text{Ga}_{0.3}\text{As}$ layer was another area of concern for us, as it is the limiting breakdown voltage across this layer which determines the maximum strength and depth of our ion trap. On a separate chip, electrodes were tested with up to 70 V dc before breakdown occurred, and some were able to withstand significantly more voltage. The resistance was measured using a picoammeter (Keithly), and are measured to be $1 \text{ G}\Omega$ up till about 10 V . We observed that the current at a given voltage depends also on the polarity of the voltage applied as well as whether the room lights are on, though the effects are negligible below $\sim 40 \text{ V}$ of applied static potential. If these had been limiting to our applied voltage, we would have investigated them further and more methodically. However, the maximum RF voltage which could be applied was $\sim 11 \text{ V}$ at 14.75 MHz to a dummy sample. We attribute some of this disparity to the greater power dissipation and perhaps the subsequently higher

temperature when RF is applied. Most of this dissipation is in the lossy electrodes and is due to the current flowing as a result of the non-zero capacitance between RF and RF grounded layers. Other solid state effects could certainly be contributing to the breakdown problem.

6.5 GaAs trap fabrication

An overview of the GaAs fabrication process is shown in the schematic (figure 6.2) and the following sections detail specific aspects of the fabrication process. As shown in the figure, the GaAs structure is grown with alternating layers of GaAs and AlGaAs and the backside of the structure is etched up to the bottom layer of AlGaAs. Then the topside electrodes are etched with a plasma etcher and bond pads are laid down for electrical contacts.

6.5.1 Scribing, dicing, and thinning

Since this project was not a production level operation and material was not in infinite supply, I diced the wafers first into 1 cm x 1 cm squares before processing. This way each die was a single ion trap, and as I gained fabrication experience and figured out better processing techniques I was able to increase my yield rate, without at any time jeopardizing a whole GaAs wafer on a potentially failing process. In many ways the non-deterministic nature of fabrication, referred to by some as the artistic side, can be attributed to the need to be conservative with material, which precluded processing an entire wafer with multiple traps in a single run. The downside was that I had to individually spin photoresist, expose, and develop each die. It was important that I marked each die to determine the 110 crystal plane - we will see later on that this was crucial for choosing the orientation of the backside etch. After each die was separated (which is easy, since GaAs always breaks along its crystal planes), I mounted them MBE grown side face down onto a slightly larger silicon die with black wax. This was crucial for increasing the yield of the process - since the die had to be thinned to

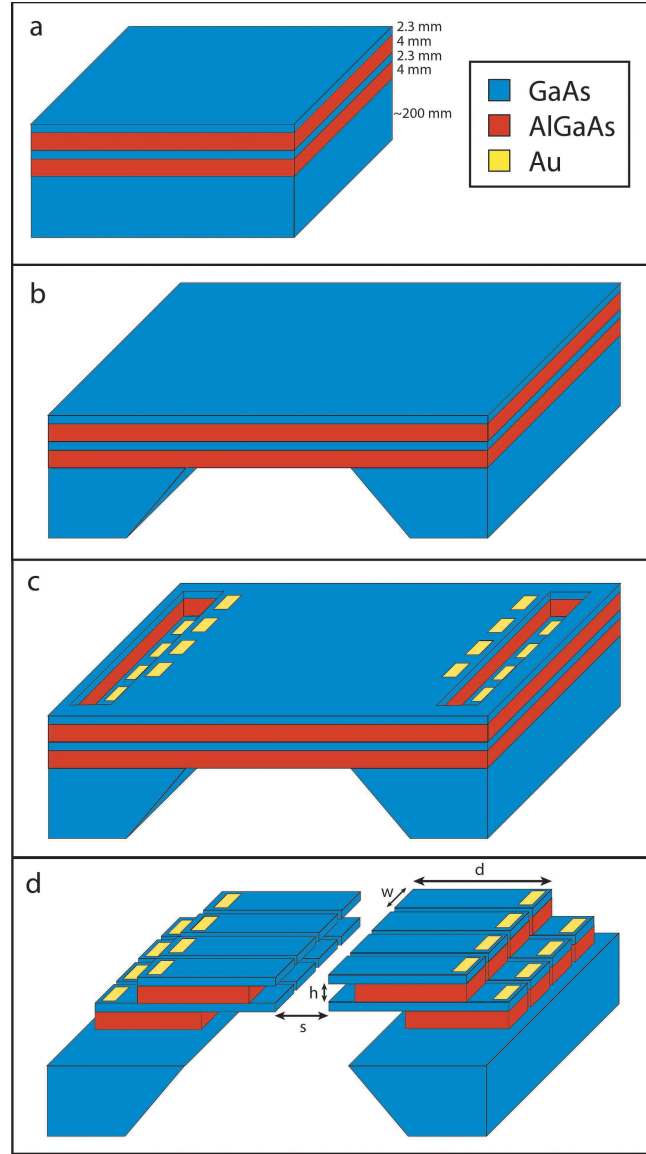


Figure 6.2: The fabrication process for a semiconductor ion trap. **a**, The structure grown by molecular beam epitaxy consists of alternating GaAs/ $\text{Al}_{1.7}\text{Ga}_{0.3}\text{As}$ membrane layers on a GaAs substrate. **b**, The back-side etch removes substrate material for clear optical access through the chip. **c**, The inductively coupled plasma etch through the membrane creates access to submerged GaAs layers, and gold/nickel/germanium bond pads are deposited for electrical contacts to the trap electrodes. **d**, A further inductively coupled plasma etch through the membrane defines and isolates the cantilevered electrodes, and a hydrofluoric acid etch undercuts the $\text{Al}_{1.7}\text{Ga}_{0.3}\text{As}$ insulator material between electrodes.

about 150 microns before performing the backside etch, by putting them on a silicon die I was able to avoid handling the actual GaAs, which risks breaking them in half or damaging their edges because they are so thin. Also, putting them face down protects their MBE surface from accidental scratches or damage from particulate material. The black wax has to be thinned with tetrachloroethylene (TCA) before spinning it onto the silicon handle at about 70 RPM for 60 s. This is then baked at 120 °C for 120 s, tapped down while the wax is still soft, and then baked at 90 °C for 120 s. After cooling for a few minutes the excess wax should be removed by squirting it with TCA and then baked again at 90 °C for another 120 s.

Now that the die are mounted (they should be relatively flat after pushing them down while the wax is still soft), each die was ground down to between 150 and 200 μm with a wafer grinder. The silicon handles were attached to the metal disk on the wafer grinder using crystal bond which is heated to 65 °C on a hot plate. I used a 9 μm grit aluminum oxide powder with a 1:4 ratio of powder to water which constantly dripped onto the wafer grinder. Depending on the amount of polishing solution and the weight pushing down on the GaAs die, it will take 30 to 60 minutes to polish the die down by about 300 μm . At the end the crystal bond can be removed by soaking the die in acetone. The nice feature about using crystal bond is that it melts at a lower temperature than the black wax and the acetone that removes it doesn't affect the black wax, so the GaAs die remain attached to their silicon handles.

6.5.2 Photoresist and standard procedures

At this stage we have individual, 1 cm x 1cm square GaAs die which are thinned down to a thickness of about 200 μm . We used the OiR 908-35 positive photoresist almost exclusively for the processing. It is available from Arch Microelectronics, and offers a good etching profile when used with the Inductively Coupled Plasma etcher (ICP) and holds up to the chemical etches used in this process. Before the photoresist is spun, the sample is cleaned with acetone, methanol, and isopropyl alcohol. Then it is attached to the sample holder and several drops of hexamethyldisilazane (HMDS)

are spun on it at 4000 RPM for 60 s. HMDS is a cleaner/solvent that prepares the surface and helps the photoresist adhere to it. Then the sample is covered in OiR 908-35 and spun at 4000 RPM for 60 s. The ramp acceleration should be above 2000 RPM/s to prevent a large edge bead from forming. The sample should then be soft baked at 90 °C for 60 s on a hot plate. Once the photoresist mask is aligned, the sample should be exposed for 13 s with a 12 W/cm² mercury lamp UV source. Then the samples should be hard baked in an oven at 105 °C for 60 s. After it cools off for a minute, develop the sample with OPD 4262 (supplied by Olin) for 60 s and rinse in DI water for 30 s. This should give a nice photoresist profile which is a few microns thick, holds up well to acid etching, and comes off easily with acetone.

6.5.3 Backside etching

This is the lowest yield stage; it involves chemically etching to the near the bottom MBE grown layer of Al_{0.7}Ga_{0.3}As with a fast etch and then switching to a slow selective etch to stop on that layer. The backside mask is a rectangle that is 200 – 400 μm wide and over a thousand μm long, depending on the width of the desired backside etch. The etch produces a hole over which the cantilevers will be suspended, allowing laser access to the trapping region. It is important that the primary flat of the wafer (exposing the 110 plane of the wafer) is parallel to the long axis of the backside rectangle (see figure 6.3). This gives an etch with vertical long sidewalls and a curve in the long direction. It is easier to get the selective etch to stop in this orientation because it typically hits at a low point in the middle and extends the width of the membrane at the same time (see figure 6.3). It is also easier to control the width of the membrane; if you have a 300 μm wide mask and are etching through 200 μm of GaAs, you will end up with a membrane that is about 200 μm wide. This width is dependent not only on the angle which the GaAs etches at, but also the amount of undercutting of the photoresist. If the etch is perpendicular to the flat (figure 6.4), you tend to get fat half ovals when you stop on the membrane, and you often have to leave it in the selective etch longer, which often results in punctured membranes.

This is apparent from figure 6.5, where you can see that the etch didn't really hit the bottom except for the tan part around the black hole at the top. Even if the etch hadn't gone through you can see that the membrane stop would be an irregular curved surface, as compared to the nearly perfect stop (green) in figure 6.3.

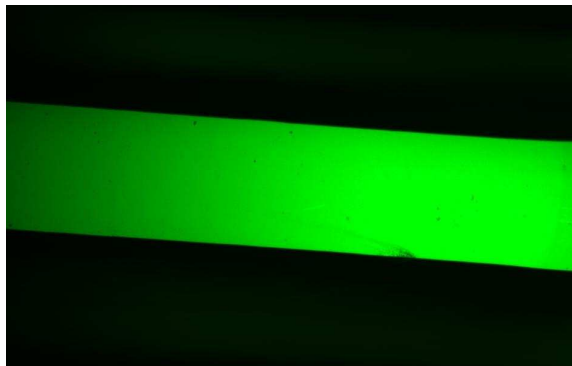


Figure 6.3: This top layer membrane was etched with its long axis parallel to the primary flat. This orientation results in straight the sides at the $\text{Al}_{0.7}\text{Ga}_{0.3}\text{As}$ intersection, which is advantageous for controlling the gap that the electrodes are suspended over.

After developing the photoresist the die is baked for several minutes longer at 105 °C just to make the photoresist harder. The descum procedure on the plasma asher is then used to clean off any photoresist which may not have been removed by the developer. This step is performed because there were a few times when seemingly exposed sections of GaAs did not etch during the chemical etch, or etched differently, and the culprit was determined to be a remaining residue of photoresist.

The piranha etch is fast and non-selective, and typically consists of a high ratio of sulfuric acid to hydrogen peroxide. The chemical reaction involves the peroxide oxidizing the GaAs which is then dissolved by the acid. In this experiment, a low weight ratio (1:3:16) of H_2SO_4 : H_2O_2 : H_2O was used (corresponding to a 1:4:5 volume ratio of 50% sulfuric acid solution and 30% peroxide solution). This gives a smoother surface, whereas a higher concentration of sulfuric acid produces a rougher

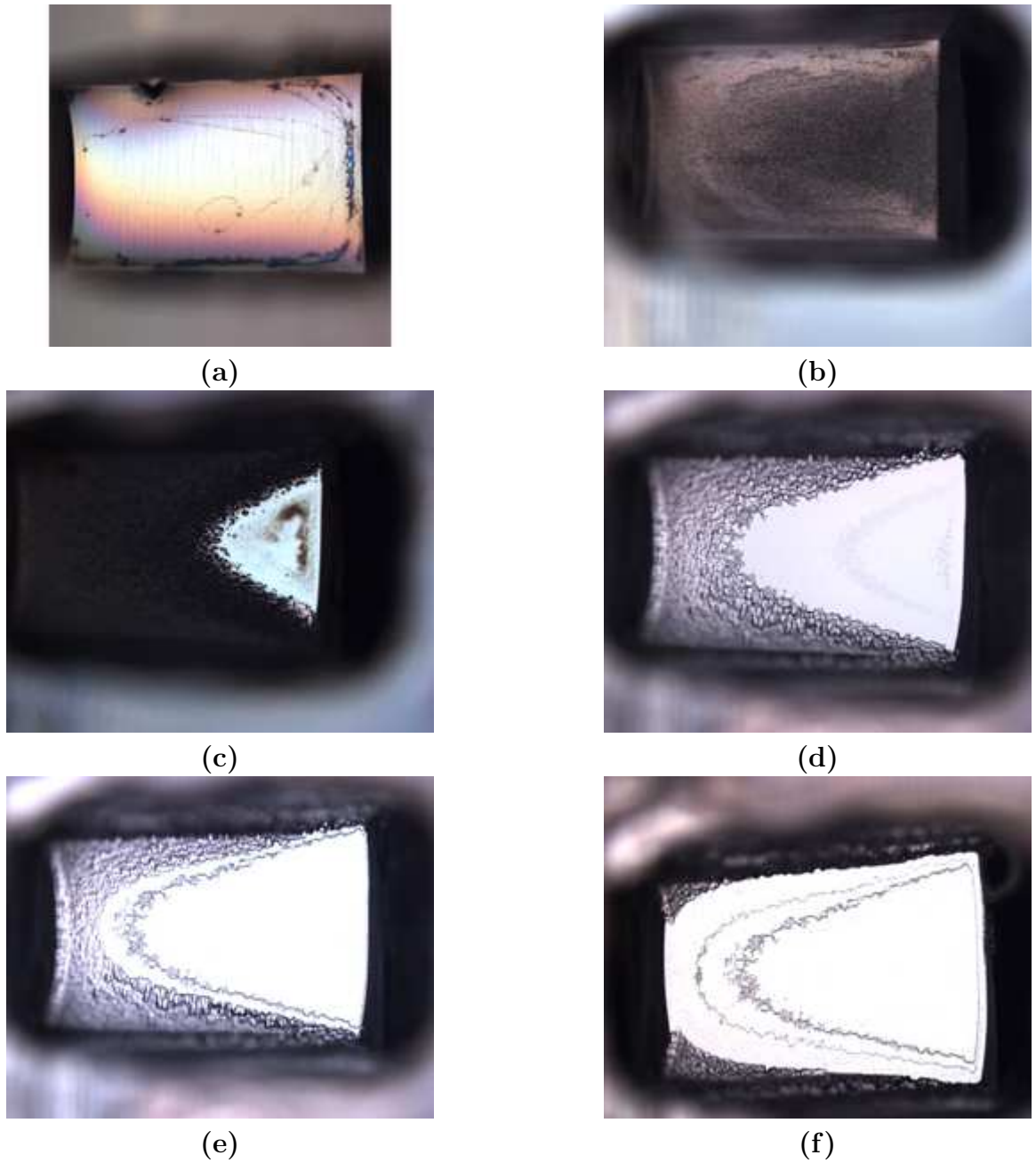


Figure 6.4: In this case the long axis of membrane was etched perpendicular to the primary flat. This series of pictures was taken at different stages of the backside etch, with **a** and **b** during the piranha etch and **c** through **f** during the citric acid etch. The half oval shape is characteristic of this direction of etch as it stops on the $\text{Al}_7\text{Ga}_3\text{As}$ (**c** - **d**); the irregularity of the width makes etching the cantilevers on the topside difficult to align. Some rings of GaAs remain even after the citric acid etch (**e** and **f**) (they will come off in the final HF etch).

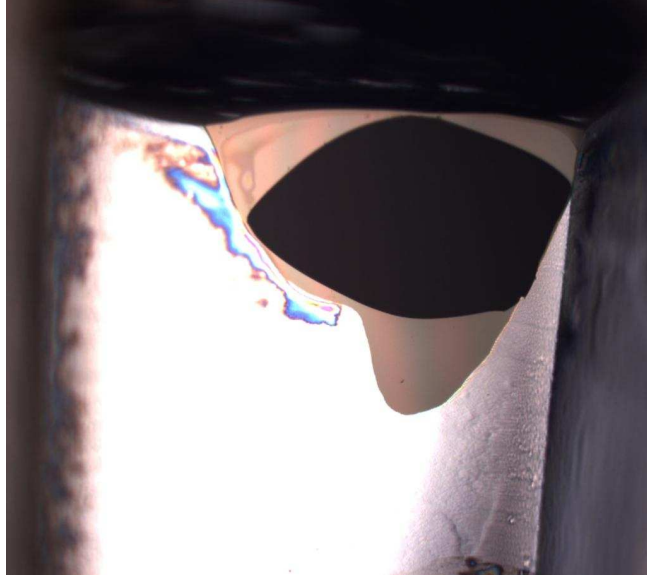


Figure 6.5: By etching too long (especially when etching perpendicular to the primary flat) there is a risk of puncturing the membrane, as seen by the black hole.

surface. It is important to minimize surface roughness and height variations so that the following selective etch reaches the bottom $\text{Al}_{0.7}\text{Ga}_{0.3}\text{As}$ layer at about the same time across the backside. The etch rate depends on a variety of factors, including temperature, whether the solution is continuously stirred or not, time, and freshness of solution. For consistent results, we used fresh solution which was not continuously stirred but was heated at $75\text{ }^{\circ}\text{C}$ to increase the etch rate. The starting etch rate was about $20\text{ }\mu\text{m}/\text{min}$ for the first two minutes, about $10\text{ }\mu\text{m}/\text{min}$ for the next four minutes, and bottoming out to about $6\text{ }\mu\text{m}/\text{minute}$ after that.

Variability in the thickness of the wafer as well as the changing rate of the piranha etch made it difficult to predict the amount of time necessary to get close ($\sim 20\text{ }\mu\text{m}$) to the bottom $\text{Al}_{0.7}\text{Ga}_{0.3}\text{As}$ layer. Therefore the sample was removed from solution after a certain period of time to measure the etch progress. The profilometer could only measure about $80\text{ }\mu\text{m}$ deep; to determine the total etch amount would require putting a dummy sample in at the same time and measuring etch steps in $80\text{ }\mu\text{m}$ increments. A simpler and suitably accurate method to use instead is to focus the microscope on the bottom of the etch and the photoresist protecting the substrate backside, taking the difference in heights.

The trickiest part is the selective citric acid etch, which can be 60:1 selective in its etching rate of GaAs over $\text{Al}_{.7}\text{Ga}_{.3}\text{As}$. Original tests used a sample with a different composition ($\text{Al}_{.3}\text{Ga}_{.7}\text{As}$), but we concluded that the selectivity of the citric acid etch was too low to stop on the bottom layer without puncturing it. We start with a 1:1 mass ratio of the anhydrous granular citric acid (FW 192.13) and deionized water. It should be heated and stirred to dissolve the acid when mixing it the first time, and then stirred each time before used to make sure it is well mixed. We found the most selective solution has a weight ratio of .36:.09:.55 of H_2CO_3 : H_2O_2 : H_2O (in volume this is a 2.5:1 ratio of 50% citric acid to 30% peroxide). It is crucial to get this exactly right: rinse the graduated cylinders with the liquid that will be measured in them and use an eye dropper to fill it with the exact amount. It should be stirred well before using. Place the sample in the beaker and check it under the microscope after 20 minutes. If the etch has stopped on the bottom of the $\text{Al}_{.7}\text{Ga}_{.3}\text{As}$ layer it will be apparent from the sharp edge between the nearly vertical wall and the smooth bottom of the $\text{Al}_{.7}\text{Ga}_{.3}\text{As}$, which should look uniform and all be at the same focus in the microscope. If it has not reached this point, the solution should be changed and the etch repeated. This can be a long process, as the etch rate for GaAs with this ratio of citric acid to peroxide is about .25 $\mu\text{m}/\text{min}$. If the sample were left in the citric acid for too long, it would eventually etch through the bottom $\text{Al}_{.7}\text{Ga}_{.3}\text{As}$ layer as well, ruining the sample.

At this stage the GaAs samples were taken off the silicon holders by soaking them in TCA overnight. It is possible to heat the wax on a hot plate at 120 °C and slide the sample off, but this is prone to breaking the newly created and extremely fragile membrane. This membrane should be visible once the silicon handle is removed, as it will be slightly buckled and the light will reflect off of it differently (see figure 6.6). The etches where the long direction of the backside etch is perpendicular to the wafer flat tend to buckle more. Etches in the parallel direction will typically just have one curved buckle, not convoluted veins like the one in the figure.

A possible future direction of the GaAs trap would be to make a three layer junction trap, which would require making “Y” shaped backside etches (figure 6.7).



Figure 6.6: This image of the MBE grown membrane after the back-side has been etched shows it buckling under the strain from the substrate. When the cantilevers are etched in the ICP this strain will be relieved and the cantilevers will be flat.

The difficulty of this lies in the directionality of the etch, since the GaAs etch shape depends on its orientation to the 110 crystal plane (see figures 6.5 and 6.3. Some initial masks for this used Y shapes which became narrower at the intersection (since the etch tends to round off the corners), but this doesn't seem like it will be necessary for thinner GaAs pieces (these used about 150 μm thick samples - much thinner and they become almost impossible to handle without breaking).

6.5.4 Bondpad etching

The first step in etching the bondpads is to spin photoresist, which requires putting a piece of tape on the bottom of the sample so that it can be held by the vacuum chuck of the spinner without sucking out the membrane. Use OiR 908-35 as before, but spin it at 3000 RPM, keeping everything else the same. The bondpad alignment is made difficult by having to align it with the backside etch, which is not visible under the mask aligner. Using an infrared light source the backside etch becomes visible from the top, and the bond pads can be aligned so that the membrane is right



Figure 6.7: Future trap designs might include junction regions (for a three layer trap, but not a two layer trap). This junction would require a “Y” shaped backside etch, complicated by the etching differences between the axis parallel and perpendicular to the substrate flat. By aligning one stem of the Y parallel to the flat and the other stems at a 60° angle, the membrane edges come out straight, similar to figure 6.3

in the middle of the two rows of pads. Making contact between the sample and mask should be done very gently using the fine tuning vertical knob. Pushing too hard can easily break the GaAs. Since the features are relatively large in this step it is not crucial to have great contact, so a conservative approach is justified here. The photoresist is then exposed and developed as described before.

At this stage the GaAs sample is remounted with wax on a silicon holder, this time with the membrane facing up. One should be careful not to push too hard on it (now that it is thin, has a really thin membrane, and has photoresist on top), but it is also important to make sure that it is mounted flat for mask alignment. The wax is applied the same as before, but the excess wax cannot be cleaned off because that would remove the photoresist too. The next step is to etch the GaAs bondpads in the ICP (from Plasma-Therm 770 SLR), which uses a plasma that is generated by electrical currents produced by oscillating magnetic fields ([55]). The plasma generates reactive species (introduced via gas lines) which chemically etch

the sample material. This has the advantage over other dry etching techniques that the process can be done at relatively low temperatures, which is critical for highly doped GaAs because high temperatures will allow the dopants to move around and redistribute themselves. The ICP selectively etches GaAs over the OiR photoresist at about a 4:1 rate, which allows for up to 10 μm of GaAs etching. It will also etch gold, so make sure any bond pads are covered with photoresist before you etch (this is important later).

To use the ICP, the sample is first mounted on a sapphire disc by smearing DOW vacuum grease on the disc and pushing the sample down so that it makes good thermal contact. The die should be arranged as close to the center of the disc as possible for uniform results, although for long etches like ours this is not a big effect. Scrape the excess grease off with a razor blade and mount the other samples the same way. Always put a dummy sample on the disc to check the etch rate, going about half way and taking it out to measure on the profilometer. This will result in an extra step which might seem unnecessary given the relatively consistent etch rates of the ICP, but given how much time has been invested up till now it requires relatively little extra work in comparison to the heartache that can come from ruining good samples. The speed of the ICP etch also depends on the number of samples; the more there are, the slower the etch rate. A typical rate is .75 $\mu\text{m}/\text{min}$ for 7 samples on the disc. The ICP used in these experiments uses a loadlock for fast sample turnaround time. The settings used are reported in table 6.5.4.

The ICP bond pad etch requires two etch distances, one to access the substrate ground and the other to access the bottom cantilever layer. In the ICP, the first step etches the substrate ground bond pad part way down, and the second step etches to the cantilever bond pad etch and the rest of the way to the ground bond pad at the same time. Given that the second layer of GaAs was between 6.3 and 8.6 μm below the surface, I aimed for etching 7 μm down, allowing for plenty of room for error but also a reasonably thick GaAs layer under the bond pad.

Once the ICP etch is done, the samples are removed from the sapphire and squirted with acetone and soaked in TCA, which is the only way to remove the vacuum grease.

Temperature:	25 °C
Pressure:	5 mT
Helium flow rate:	4 sccm
BCl ₃ flow rate:	12.5 sccm
Cl ₂ flow rate:	2.5 sccm
Ar, CH ₄ , O ₂ , SF ₆ flow rate:	0
RF 1 Inc power:	70 W
RF 2 Inc Power:	515 W (set to 500 W)
DC volt:	185

Table 6.1: ICP settings

Since the samples are mounted by wax on the silicon die, the die are only soaked for about a minute, not long enough to dissolve the wax.

6.5.5 Ohmic Contacts

Ohmic contacts are made with the common lift-off technique. OiR 908-35 is used again as the photoresist, and the bond pads are aligned in the mask aligner such that they fit totally within the etched areas. Given that the etch is fairly deep compared to the thickness of photoresist (which is about 3 μm), we check to make sure that the edge of the etch is properly covered with photoresist. Before putting the samples in the ebeam evaporator (CHA Mark series), the sample is descummed in the plasma asher for 30 s, dipped in a 10:1 water:HCl solution for 10 seconds to remove the oxide layer, dipped in water, and blown dry. This cleaning technique is important for removing any photoresist residue, which would prevent the bond pads from sticking to the GaAs. The samples should be loaded in the stationary (not planetary orbital) CHA holder. The deposition recipe is shown in table 6.5.5.

Once the bond pads are evaporated, the samples are soaked in hot acetone (88 °C) for an hour and left for a few hours in room temperature acetone. Sometimes the gold had to be squirted off with acetone before it started falling off in the places with photoresist. If any shorts remained between bond pads, blue tape (or scotch tape)

Material	Thickness
Ni	150 Å
Ge	800 Å
Au	400 Å
Ni	300 Å
Au	4000 Å

Table 6.2: CHA Recipe

was gently pushed down over the bond pads and peeled off. The tape was sticky enough to pull up the unsupported gold, but not so sticky that it pulled up the bond pads. Never ultrasonicate these to speed up the process - the membranes will break.

In some early experiments we had a problem covering up the vertical parts of the etch, and observed shorting between top and bottom electrodes. This can be seen in figure 6.8 with the gold coating the sidewall and shorting the two bond pads.

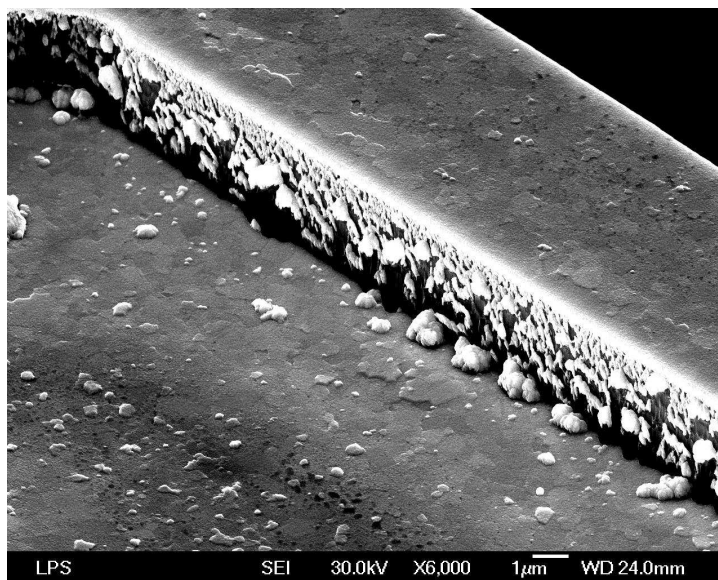


Figure 6.8: Gold bond pads deposited vertically shorted the top and bottom electrodes, as can be seen in this SEM of the inside edge of a bond pad. This problem was solved by covering the edges with photoresist.

6.5.6 Cantilever etching

The cantilever etching is the step when the trap geometry really takes shape. It uses the same ICP process as above, but because it is a longer etch we have to spin OiR 908-35 as slow as possible - about 2500 RPM - so that the resist is thick enough to protect the electrodes during the entire ICP etch. Besides having to go a long distance, the ICP etches more slowly in narrow regions, like the 10-15 μm gap between two cantilevers, so the etch must go longer than the actual 8.6 μm minimum. We could have solved this in future masks by having the part of the cantilever that is suspended close together (since the $\text{Al}_{0.7}\text{Ga}_{0.3}\text{As}$ will be etched away here anyway) but have the gap larger as it gets farther back from the electrode tips. This etch uses the same parameters as listed in table 6.5.4 with the difference that the pressure is lowered to 2.5 mT; when etching with plasma, low pressures etch better in narrow valleys, though the overall etch rate is slower.

6.5.7 Annealing

To make good ohmic contacts, the bond pads must be annealed. This has to be done after removing the silicon handles with TCA, as the black wax will contaminate the rapid thermal annealer. The temperature schedule for this process is shown in table 6.5.7.

The important aspects are that there is a beginning 250 $^{\circ}\text{C}$ phase that is held for about 30 s and a 450 $^{\circ}\text{C}$ phase that is held for about 60 s. The other numbers have to do with correcting for overshooting while ramping, and usually need to be adjusted. The down ramp at the end is slow enough that the last 250 $^{\circ}\text{C}$ hold is probably unnecessary.

6.5.8 $\text{Al}_{0.7}\text{Ga}_{0.3}\text{As}$ etch

HF is a very selective etch for $\text{Al}_{0.7}\text{Ga}_{0.3}\text{As}$. After cleaning off the sample after

		Time/Rate	Temp	T _{sw}	Gain	D _{Gain}	I _{Warm}	I _{Cold}
1	DLY	10						
2	RAMP	10	250					
3	SS	30	250	0	-200	-10	800	800
4	RAMP	20	450					
5	SS	60	450	50	-100	-5	1200	1200
6	RAMP	10	250					
7	SS	30	250	50	-100	-5	1200	1200
8	RAMP	50	50					
9	DLY	120	0					

Table 6.3: Annealing recipe

the ICP etch, a pointy q-tip is used to put globs of photoresist to protect the bond pad areas. They are then baked in the oven at 105 °C to prevent HF undercutting. Then put the samples are soaked in concentrated HF for 1 - 1.5 minutes, soaked in acetone for a few minutes, dipped in deionized water, and allowed to air dry. This time was found through trial and error as the longest period for which the cantilevers would be strong enough to not collapse together (see figure 6.9) after being pulled out of the HF solution. Another technique would be to use a supercritical drier after the HF etch, but we found that 1 - 1.5 minutes was sufficient to etch the Al₇Ga₃As back by about 15 μ m. After taking it out of the HF I put the sample in distilled water and then acetone and finally let it air dry. If you watch under a microscope while it is drying you can sometimes see the cantilevers flex back and forth due to the adhesive forces of acetone. After this, the “Strip” program on the plasma asher (which is a more powerful version of descum) was run to get rid of any residue on the bond pads left by the acetone. As usual, we had to be very careful with HF as it is highly dangerous; we always used gloves, a facemask, an apron, and Teflon containers when dealing with it, and disposed in the proper bottles.

6.5.9 Attaching to chip carrier

While attaching the chip to the chip carrier was the easiest part, great care was

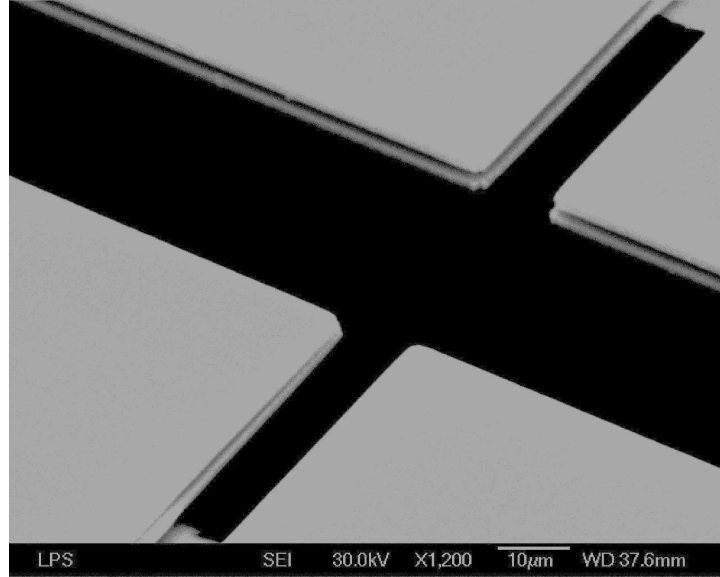


Figure 6.9: This image shows the effects of leaving the sample in the HF etch for too long. The bottom left cantilever tips have collapsed together; in an even longer HF etch, one of the cantilevers would typically fracture and stick to the other one or float off in the solution.

taken so as not to ruin a sample that had successfully made it through the process (which all told takes about a week). Towards the end of my processing I could expect about a 50% yield for the entire process. To attach the chip we used Sanereisen ceramic cement which provides just enough strength to hold the chip. Its main attractive feature is that it is UHV compatible and we had used it successfully in previous traps. The ceramic cement is mixed with water (20:1 cement to water ratio) to give it a smooth but solid consistency. The chip carriers (4.3) were cleaned in an ultrasonic acetone bath and rinsed with methanol and IPA before attaching the trap die to them. The ceramic paste should touch the both the top of the die (being careful not to get it on the bond pads or cantilevered electrodes) and the edge of the inside of the chip carrier - this makes the hold much stronger. Then the cement was allowed to dry for two or three days before putting it in the chamber.

6.5.10 Interconnects, RF grounding, and filtering

The bond pads were connected to the chip carrier (in this case a leadless chip

carrier from Global Chip Materials) using a K&S 4129 deep access wirebonder. The gold wires are $25\ \mu\text{m}$ in diameter and connect from the bond pads on the GaAs to an output lead on the chip carrier. The RF cantilevers are connected to their RF neighbors and then attached to the same RF output lead. Each DC cantilever is attached to its own DC chip carrier lead, which is then attached via a gold ribbon ($13\ \mu\text{m}$ thick $400\ \mu\text{m}$ wide) to a ceramic $1000\ \text{pF}$ capacitor. These capacitors are attached to the chip carrier with ceramic paste (see figure 6.10), with their other end connected to the RF grounding lead. This serves to RF ground each DC electrode, such that the ratio of RF on the RF cantilever to the RF on the grounding cantilevers is $2\ \text{pF}/1000\ \text{pF} = 500$, leaving about $20\ \text{mV}$ on each DC cantilever. Since these DC cantilevers are symmetric about the RF node, this undesirable RF is not of much concern given that it is significantly reduced.

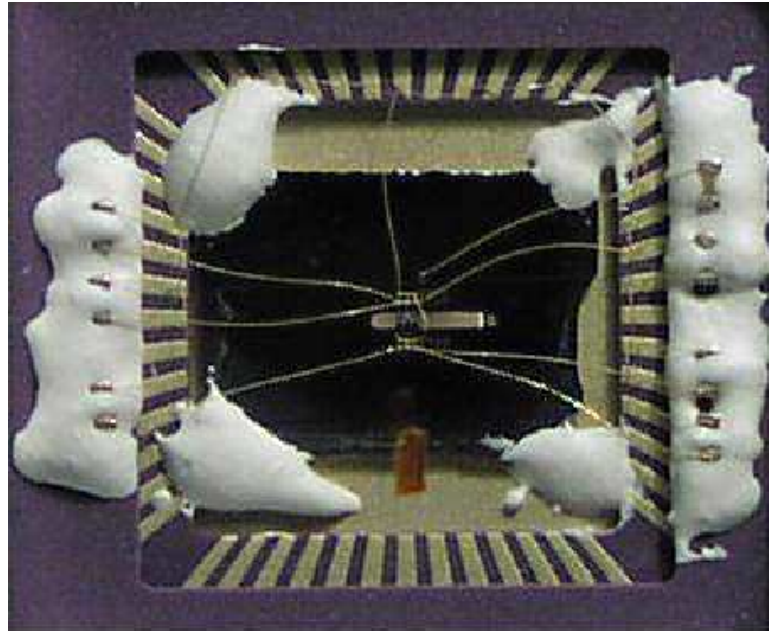


Figure 6.10: This figure shows a closeup of the GaAs mounted to a ceramic LCC. The wire connecting the DC and RF electrodes are visible, as are the ceramic capacitors which are attached to the LCC via a ceramic paste.

The chip carrier itself is connected to the chamber mount by pressing it (and its gold leads on the back of the LCC) against suspended tungsten rods which are held together in a boron nitride mount. A metal plate (see figure 6.11) with screws at each corner was placed over the outside of the LCC to apply pressure and contact the rods. Insulated Kapton wires connected these rods to feedthroughs on the vacuum chamber. This system was selected for its fast turnaround time and the ability to fabricate traps in another location and transport them mounted to chip carriers to the lab. The method of mounting the LCC was inconsistent in making electrical contacts, however, since the tungsten rods were relatively stiff. This made it difficult to contact each lead simultaneously. Ultimately another mounting technique using ceramic pin grid arrays was chosen for our next generation trap (see section 4.3).

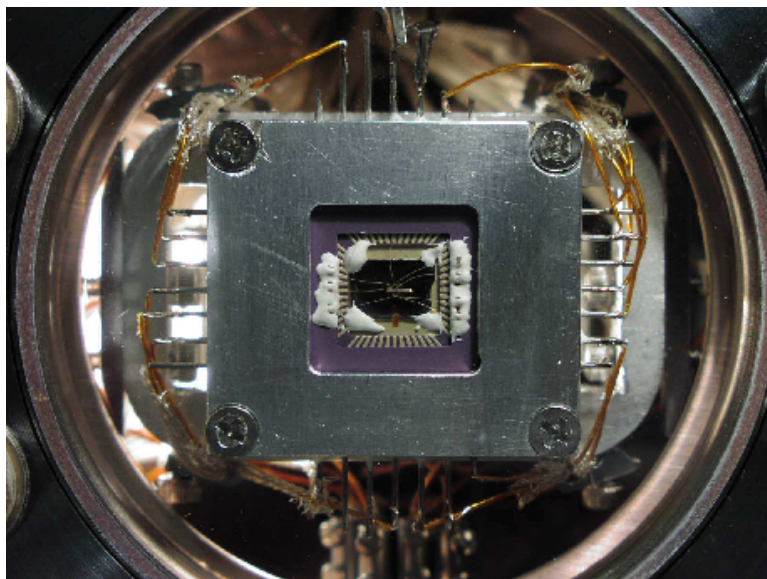


Figure 6.11: The LCC mounting structure consists of an aluminum plate with a square hole which is pressed down on the LCC against a set of suspended tungsten rods on the back of the LCC. The tungsten rods are visible sticking out from under the aluminum plate, with insulated Kapton wires attached.

6.6 Experimental results

Loading ions in the GaAs trap was a formidable task, as the maximum applicable RF voltage resulted in a trap depth of only a few times room temperature. The strategy employed was to search through a parameter space of applied DC voltages (to eliminate bias fields) for a particular RF voltage and frequency value, and if unsuccessful, repeat for a slightly higher RF voltage and frequency. During these tests the stability parameter q was held constant at $\sim .7$, which is below the maximum stability value of $.92$. If we wanted to increase the trap depth $\Psi \rightarrow \alpha\Psi (\alpha > 1)$ and yet maintain the same q , we had to increase the voltage $V \rightarrow \alpha V$ and drive frequency $\Omega \rightarrow \sqrt{\alpha}\Omega$. Since the power dissipation goes as $(V\Omega)^2$, $P_{dis} \rightarrow \alpha^3 P_{dis}$. This cubic increase in power dissipation for only a linear increase in trap depth required us to be cautious and methodical in increasing the voltage and drive frequency of the trap.

6.6.1 Operating parameters

Eventually we succeeded at loading a single cadmium ion, as seen in the CCD image capturing the ion's fluorescence in figure 6.12. A Doppler cooling laser tuned within one natural linewidth of the $^{111}\text{Cd}^+ {}^2S_{1/2} \rightarrow {}^2P_{3/2}$ transition near 214.5 nm was necessary for constant cooling of the ion. It had up to ~ 1 mW of power focused to a $\sim 15 \mu\text{m}$ waist. The photoionization laser had about 1 mW of average power focused to a $\sim 20 \mu\text{m}$ waist. With both beams aligned, a single $^{111}\text{Cd}^+$ could be loaded after a few seconds, at which time the photoionization laser was blocked. Storage lifetimes in excess of 1 hour were observed provided constant Doppler cooling, with a mean lifetime of 10 minutes (see figure 6.13). In the histogram a clear hump is seen at about 22 minutes. This is attributed to the pressure decrease immediately after trapping an ion. Often we had to aggressively fire the oven to trap in a reasonable time period, and the pressure remained high for the first few minutes after the oven was turned off. The short lifetime events seen in the graph were likely due to background collisions as a result of the increased pressure. The local maximum at 22 minutes reveals the

average time an ion can be expected to last in the trap before a normal background collision can be expected (ie not due to the oven). This lifetime, while lower than our other traps, is consistent with the expected time between elastic collisions [6] with a room-temperature background gas. In other deeper traps, the ion could potentially survive a collision or near collision, but in the GaAs trap such a collision was always fatal. This is also consistent with the fact that we never saw two ions in the same trap, a common occurrence in other traps we operated.

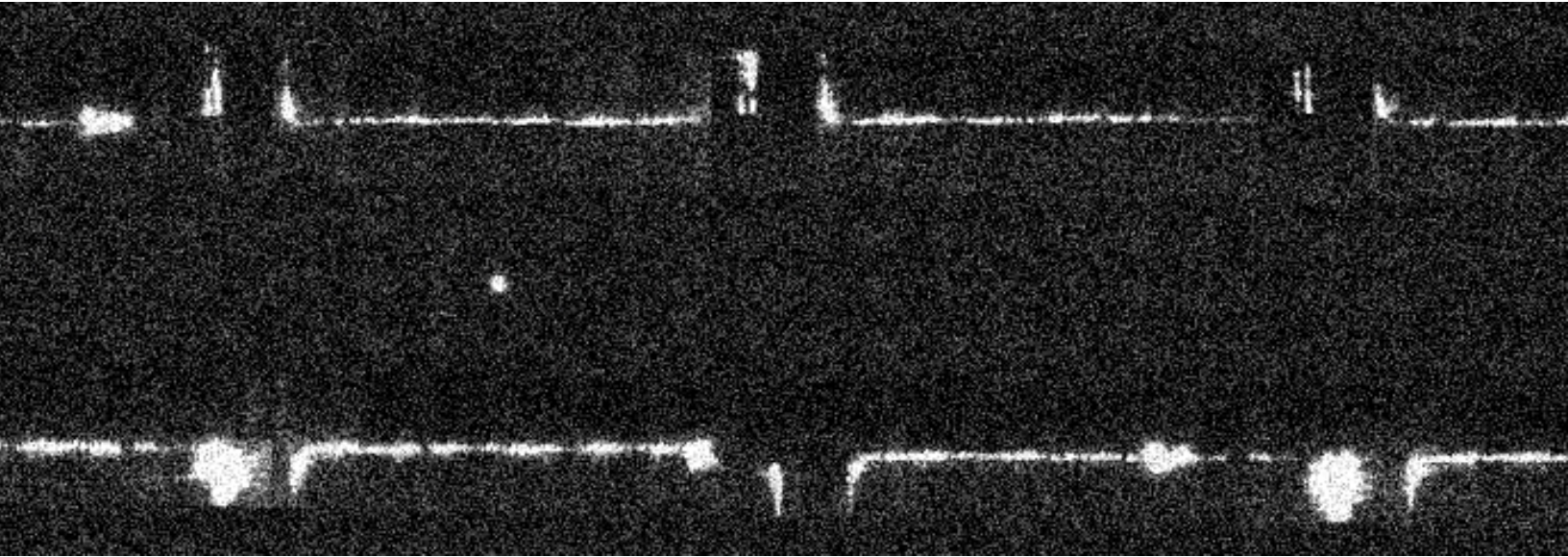


Figure 6.12: A composite image of a single trapped Cd^+ ion along a view perpendicular to the chip plane after ~ 1 s of integration time. The ion fluoresces from applied laser radiation directed at a 45° angle to the chip surface and nearly resonant with the $\text{Cd}^+ {}^2S_{1/2} - {}^2P_{3/2}$ electronic transition at a wavelength of 214.5 nm. The fluorescence is imaged onto a CCD camera with an f/2.1 objective lens, resulting in a near diffraction limited spot with $\sim 1 \mu\text{m}$ resolution at the ion. The profile of the electrodes is also clearly visible as scattered radiation from a deliberately misaligned laser that strikes the electrodes. The vertical gap between the top and bottom electrodes is $s = 60 \mu\text{m}$.

We directly measure the frequency of small oscillations of the trapped ion by



Figure 6.13: This histogram shows the lifetime statistics for 32 different ions while being continuously Doppler cooled. The events are binned into time groupings of 0-5 minutes, 5-10 minutes, The second peak at the 20-25 minute bin suggests that once an ion has survived past the high pressure period caused by the oven being fired, it is most likely to last till this 20-25 minute period. Most ions, however, do not survive this long due to a collision with a background molecule or Cd atom.

applying a weak, variable frequency potential to one of the nearby electrodes and observe changes in the ion fluorescence owing to the resonant force while it is continuously laser cooled [36]. For an applied radiofrequency potential amplitude of $V_0 = 8.0$ V at a drive frequency of $\Omega/2\pi = 15.9$ MHz and a static DV voltage of 1.00 V on the end-cap electrodes and -0.33 V on the center electrodes, we measured the axial secular frequency to be $\omega_z/2\pi = 1.0$ MHz. The measured transverse secular frequencies were $\omega_x/2\pi = 3.3$ MHz and $\omega_y/2\pi = 4.3$ MHz, indicating a radiofrequency trap stability factor of $q = .62$. These measurements are consistent with a three dimensional numerical simulation of the trapping potential, which further indicates that one of the transverse principal axes of the trap is rotate $\sim 40^\circ$ out of the plane of the chip (this is the \hat{x} axis).

Additionally, we suppressed micromotion along the direction of the Doppler cooling beam by applying static offset potentials to electrodes that minimize both the broadening of the atomic fluorescence spectrum (half-width of ~ 50 MHz, compared with the natural half-width of 30 MHz) and the time correlation of the atomic fluorescence with the trap drive frequency (figure 6.14).

6.6.2 Motional heating

Of particular concern for this trap was the anomalous heating rate. We had evidence that it was relatively high from the observation that without continuous Doppler cooling the ion would boil out of the trap within $\tau \sim .1$ s (see figure 6.15). This lifetime is contingent upon both the heating rate and the trap depth, and due to the anharmonic nature of the trap at the point where the potential turns around, is difficult to estimate the heating rate at the bottom of the trap based on the boil-out time.

To make a quantitative determination of the motional heating rate at the bottom of the trap we performed stimulated Raman spectroscopy on the hyperfine qubit levels of the ion. Given the already high temperature of the ion, it was not possible to perform the standard sideband thermometry technique discussed in section 2.2.6 because

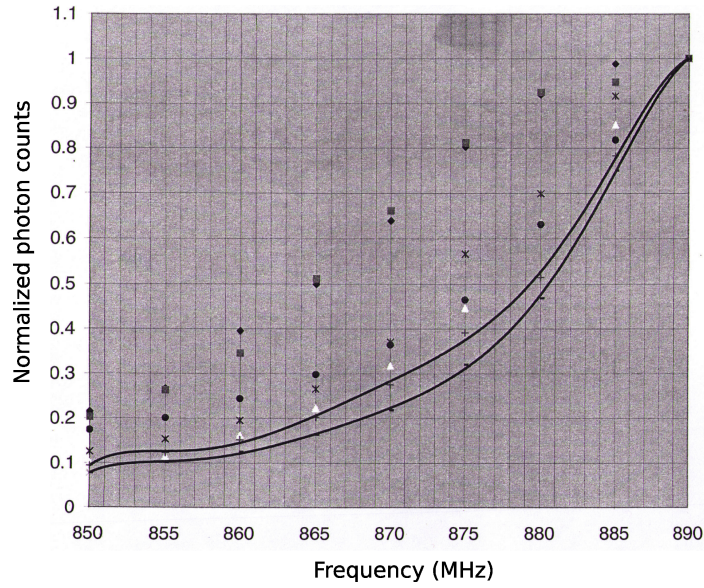


Figure 6.14: This data shows the 100 MHz linewidth achieved in the GaAs trap after compensating voltages were applied to DC electrodes. Multiple data series are shown, with fits to the narrowest two. The frequency on the bottom refers to the drive frequency of the 1 GHz double pass AOM that is used to lock the laser to the Tellurium reference line. Since this light is double passed and then gets doubled in the BBO cavity afterwards, the actual frequency should be multiplied by 4. The peak of the resonance occurs at 894 MHz.

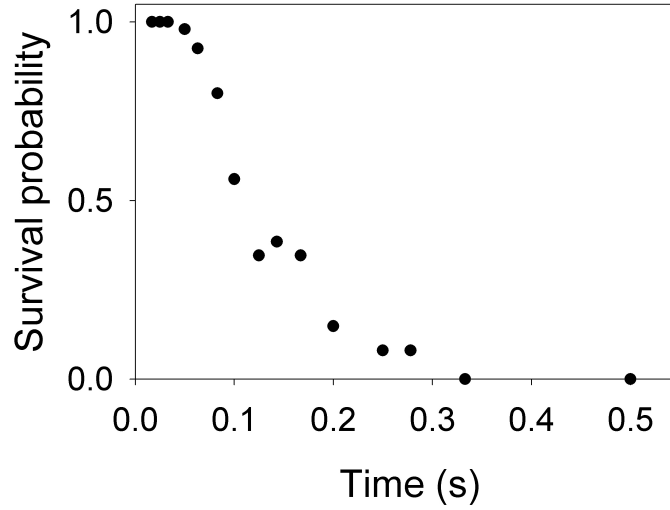


Figure 6.15: These statistics show the boil out time of an ion which is not laser cooled. Many more samples could be taken than in figure 6.13 because the time duration was shorter and a single ion could provide many data points at short time durations. From the graph it can be seen that the ion has about a 50% chance of surviving for .1 s, which gives an indication of the heating rate in the trap.

we could not cool to near the ground state using Raman sideband thermometry. By using the fact that the Raman transition rate is suppressed by the Debye-Waller factor which is temperature dependent, we could measure this suppression for different delay times. In figure 6.19 we can see the difference between the Raman transition rates for data taken .002 ms after the Doppler cooling beams were turned off and data taken 1 ms after the doppler cooling beam was turned off.

To perform this experiment required a combination of the techniques discussed in chapter 2, including initialization, detection, and as mentioned driving Raman carrier transitions. We achieved an initialization fidelity of $\sim 95\%$, as can be seen in the dark state counts from figure 6.16. A long Raman carrier transition can be seen in figure 6.17; the high heating rate increases the temperature for long Raman transition times, causing a dephasing and loss of coherence visible in the figure. The probability tends towards the bright state due to detection beam leakage from the AOM; otherwise it would tend towards a 50% bright state probability. The Raman frequency scan shown in figure 6.18 gives shows the carrier as well as red and blue

sidebands of the Raman transition.

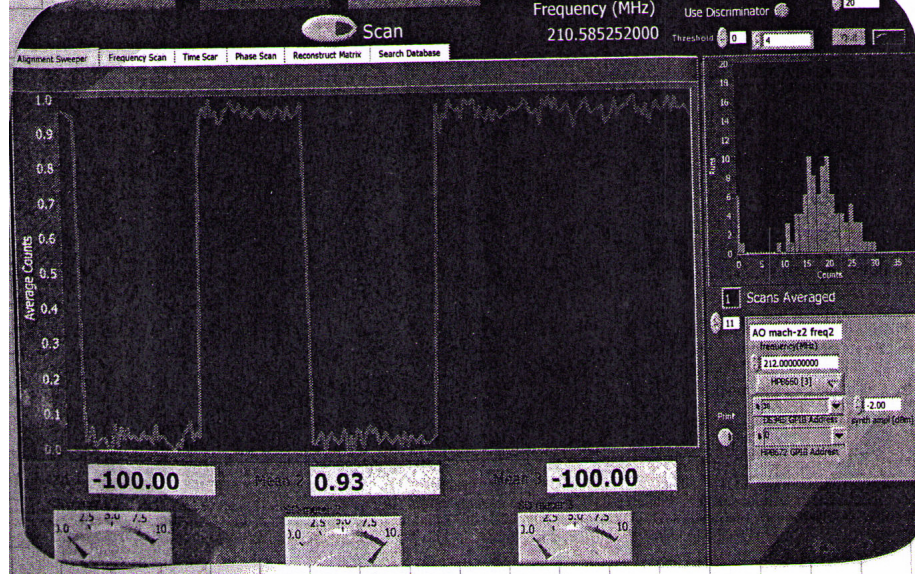


Figure 6.16: This screenshot of the dark state initialization and detection shows an experiment being run in which the initializing π beam is applied for $5 \mu\text{s}$ followed by the detection beam for $200 \mu\text{s}$. When the bright state probability is low ($\sim 5\%$), the π beam is unblocked, and when it is bright ($\sim 95\%$), the π beam is blocked.

6.6.3 Motionally sensitive carrier transition

To drive these motionally sensitive stimulated Raman transitions (SRTs) requires a pair of laser beams detuned $\sim 70 \text{ GHz}$ from the $^2S_{1/2} \rightarrow ^2P_{3/2}$ transition with an optical beat note near the 14.53 GHz atomic hyperfine splitting. The two Raman beams have a 7° angular separation, with the wavevector difference oriented 45° from the axis of the trap. This nearly copropagating Raman arrangement was chosen to minimize the axial Lamb-Dicke parameter ($\eta \sim .018$) such that even high thermal occupation levels would have a measurable carrier transition rate.

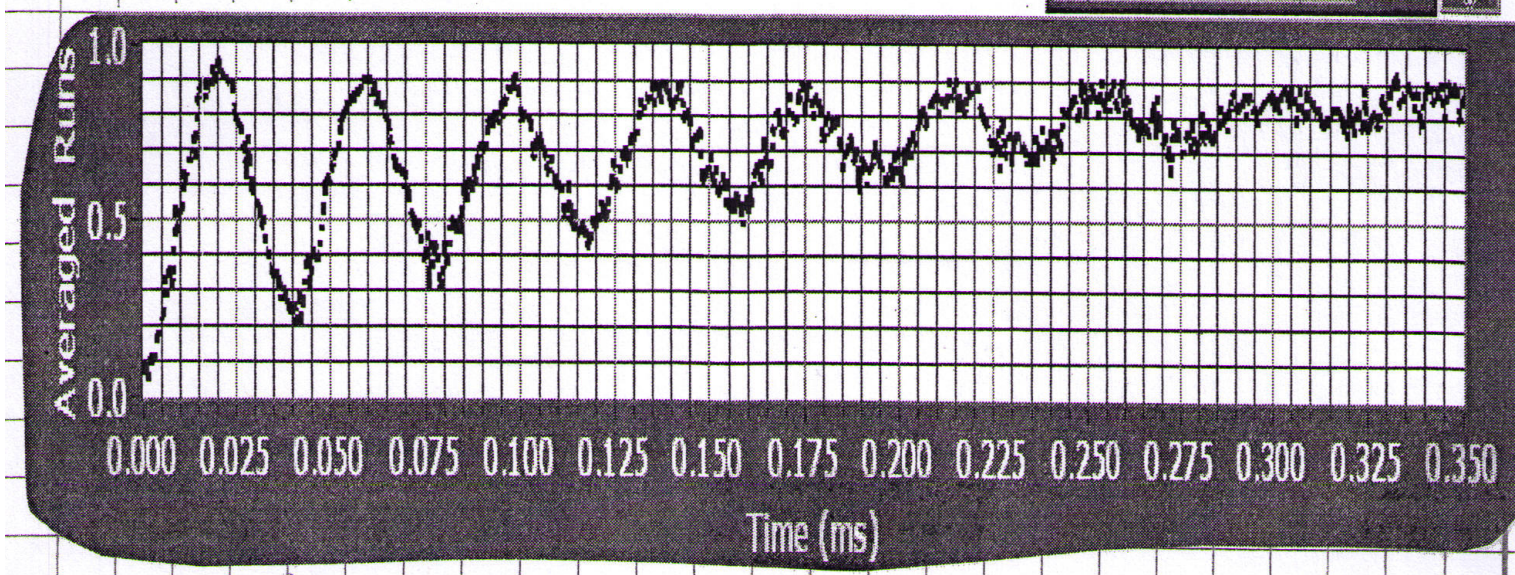


Figure 6.17: This screenshot shows several Rabi flops on the carrier transition in the GaAs trap. The loss of contrast is due to the decoherence as a result of the high heating rate in the trap. It tends towards the bright state because of AOM leakage.

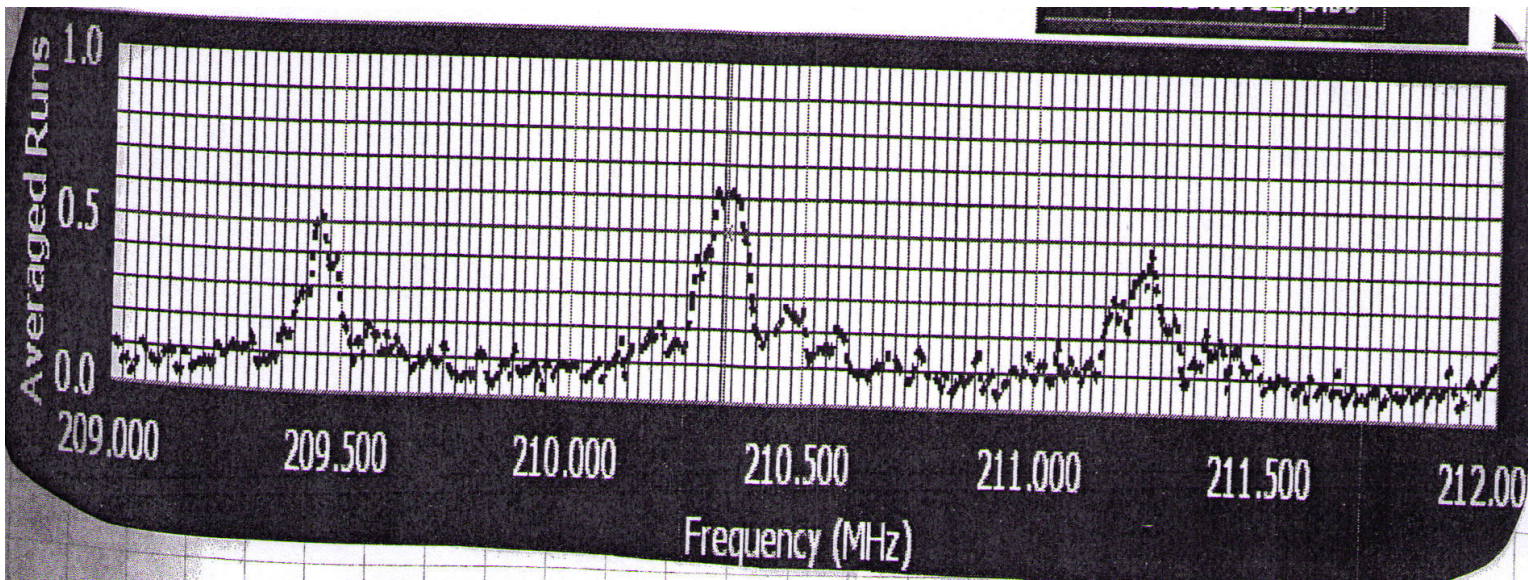


Figure 6.18: This Raman frequency scan shows the carrier transition as well as the red and blue sidebands at $\sim \pm 1$ MHz.

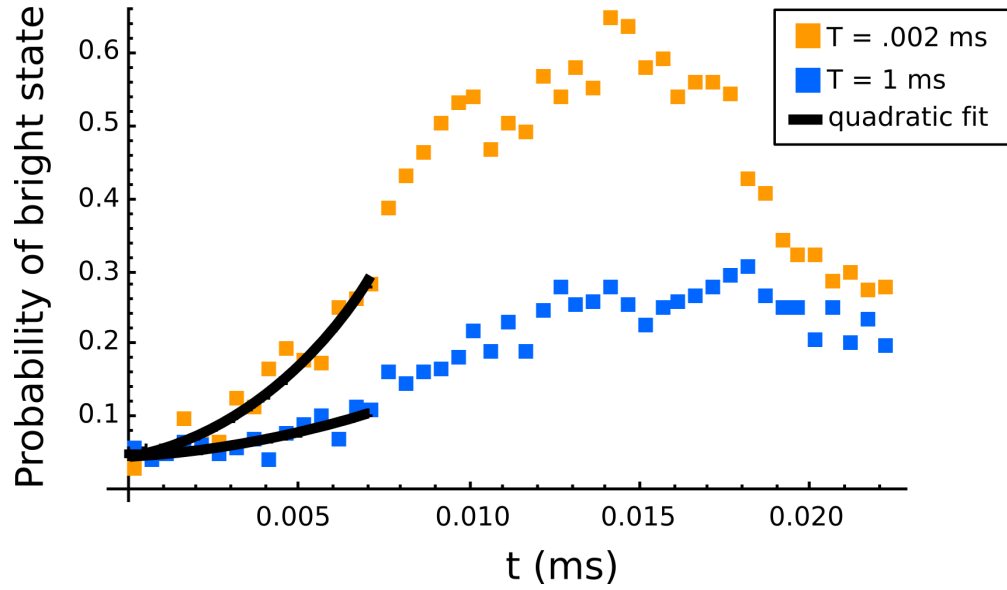


Figure 6.19: The Raman transition probability shown here are dependent on the temperature of the ion as quantified by the Debye-Waller factor. This is evident from the reduced transition rate seen in an ion which is not laser cooled for $T = 1$ ms, as opposed to the case where the Raman transition is measured immediately after ($T=0$ s). Since the transition is only fitted to 7 μ s of Raman data (the black lines), the time for an experiment is not significant compared to the delay time.

After Doppler cooling and initializing in the $|\uparrow\rangle$ state, the Raman beams were applied and the probability of a spin flip to the $|\downarrow\rangle$ state was measured for different Raman times. The probability of a spin flip occurring is:

$$S(t) = \sum_n P_n \sin^2\left(\frac{\Omega_n t}{2}\right) \quad (6.21)$$

where

$$P_n = \left(\frac{\bar{n}}{\bar{n}+1}\right)^n \frac{1}{\bar{n}+1} \quad (6.22)$$

and the carrier Rabi flopping rate is

$$\Omega_n = \Omega_0 e^{-\eta^2/2} L_n(\eta^2) \quad (6.23)$$

For $\Omega_n t/2 \ll 1$ ($\Omega_n t/2 \sim .3$ for the data we use) and $\eta \ll 1$ we can approximate

$$\sin^2(\Omega_n t/2) \approx \frac{\Omega_0^2 t^2}{4} e^{-\eta^2} L_n^2(\eta^2) \approx \frac{\Omega_0^2 t^2}{4} L_n^2(\eta^2) \quad (6.24)$$

The Laguerre polynomial can be expanded as

$$L_n(\eta^2) \approx 1 - n\eta^2 + \frac{1}{4}n^2\eta^4 - \frac{1}{36}n^4\eta^6 \dots \quad (6.25)$$

Plugging this back into equation 6.21 and keeping the first three orders of n gives us

$$S(t) = \frac{\Omega_0^2 t^2}{4} \frac{1}{\bar{n}+1} \sum_{n=0}^{\infty} \left(\frac{\bar{n}}{\bar{n}+1}\right)^n (1 - 2n\eta^2 + \frac{3}{2}n^2\eta^4 - \frac{5}{9}n^3\eta^6) \quad (6.26)$$

$$= \frac{\Omega_0^2 t^2}{4} (1 - 2\eta^2\bar{n} + 3\eta^4\bar{n}^2 - \frac{10}{3}\eta^6\bar{n}^3) \quad (6.27)$$

Defining a heating rate Γ , we set $\bar{n} = \bar{n}_0 + \Gamma T$, where T is the delay time after ion has been cooled to \bar{n}_0 via Doppler cooling till the Raman beams are applied. Inserting

this above gives

$$\frac{S(t)}{t^2} = \frac{\Omega_0^2}{4} \left[(1 - 2\eta^2 \bar{n}_0 + 3\eta^4 \bar{n}_0^2 - \frac{10}{3} \eta^6 \bar{n}_0^3) \right. \quad (6.28)$$

$$\left. - 2\eta^2 \Gamma T (1 - \frac{3}{2} \eta^2 \Gamma T - 3\eta^2 \bar{n}_0 + \frac{5}{3} \eta^4 \Gamma^2 T^2 + 5\eta^4 \bar{n}_0^2 + 5\eta^4 \bar{n}_0 \Gamma T) \right] \quad (6.29)$$

$$= A - BT \quad (6.30)$$

If we assume that $\eta^2 \bar{n}_0 \ll 1$, which is reasonable if the ion is Doppler cooled to n_D ($\eta^2 \bar{n}_D \sim .01$), then we can take the ratio $\frac{B}{A} = 2\eta^2 \Gamma \rightarrow \Gamma = \frac{B}{2A\eta^2}$.

We took data at three time delays (see figure 6.20): 0 μs , 500 μs , and 1000 μs . In the final data analysis we actually had three sets of the graphs seen in the figure, taking the average of the heating rate values found from a linear fit in each graph. This is because the data was taken at different times, and in order for the Rabi frequency to drop out in the ratio $\frac{B}{A}$, the Rabi frequency has to be the same for each time delay. Since the beam position and power can drift over time, we took data at $T = 0, 500 \mu s$, and $1000 \mu s$, and then repeated, rather than taking multiple data sets at one time delay.

The initial Raman transition rate is fit to the function $f(t) = a + bt^2$ in Mathematica, and errors are determined assuming a Gaussian distribution about the mean. This is repeated for the three time delays above, and a line is fit to that data, taking into account the error for each data point. The intercept and slope of this line are the coefficients $A \pm \sigma_A$ and $B \pm \sigma_B$, giving us a final heating rate of:

$$\Gamma = \frac{B}{A} \pm \sqrt{\left(\frac{\sigma_B}{A}\right)^2 + \left(\frac{B}{A}\sigma_A\right)^2} \quad (6.31)$$

From the three values we get for Γ , we get a mean value of $\Gamma = -1.2 \pm .4$ quanta/ μs . This value only includes statistical errors, not systematic errors. Unavoidable systematic error in this calculation are the ignored terms in equation 6.28. To make the problem more clear, we will rewrite B as:

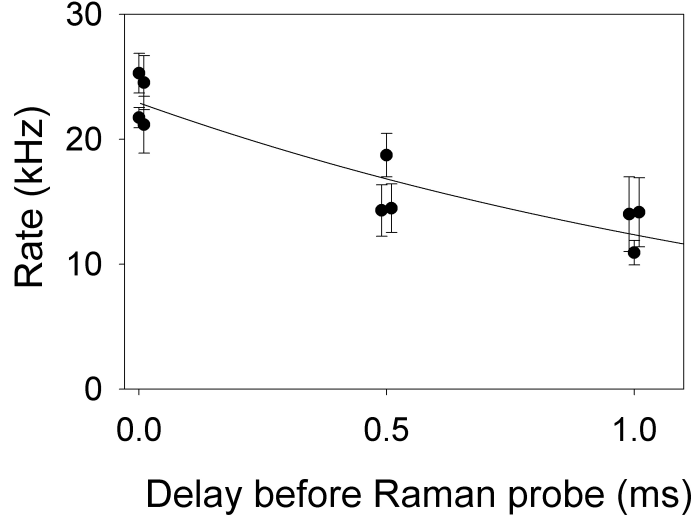


Figure 6.20: The suppression of the Raman transition after a given delay time T is shown in this graph. A line is fit to the data to determine the slope and intercept, from which the heating rate can be derived.

$$B = 2\eta^2\Gamma A \left(1 - \frac{-\eta^2\bar{n}_0 + 2\eta^4\bar{n}_0^2 - \frac{3}{2}\eta^2\Gamma T + 5\eta^4\bar{n}_0\Gamma T + \frac{5}{3}\eta^4\Gamma^2 T^2}{1 - 2\eta^2\bar{n}_0 + 3\eta^4\bar{n}_0^2} \right) \quad (6.32)$$

If we assume that $\bar{n}_0 \ll \Gamma T$ for $T = 500 \mu s$ and $1000 \mu s$, this leads to a correction in the mean heating rate which will make it lower than the fit would indicate (see figure 6.21). By factoring that correction in we get a final heating rate for the GaAs trap of $\Gamma = -1.0 \pm .5$ quanta/ μs .

We can now compare this value to that predicted from the boil-out time shown in figure 6.15. As mentioned before, this calculation is complicated by the fact that the trap becomes anharmonic farther away from the center (this will be discussed in greater detail in chapter 8), but we can make an upper-bound estimate of the heating rate at the bottom of the trap based on assuming that it is harmonic up till the trap depth, so that the heating rate is $\Gamma \leq \frac{E_{max}}{\hbar\omega_x t_{lifetime}} \approx 60$ quanta/ μs . Note that this is not measuring the same heating rate as measured with the Raman transition rate experiment above, as that heating rate was along the weak axis, and this measures it along the transverse axis. It is an upper bound on the heating rate at the bottom of the

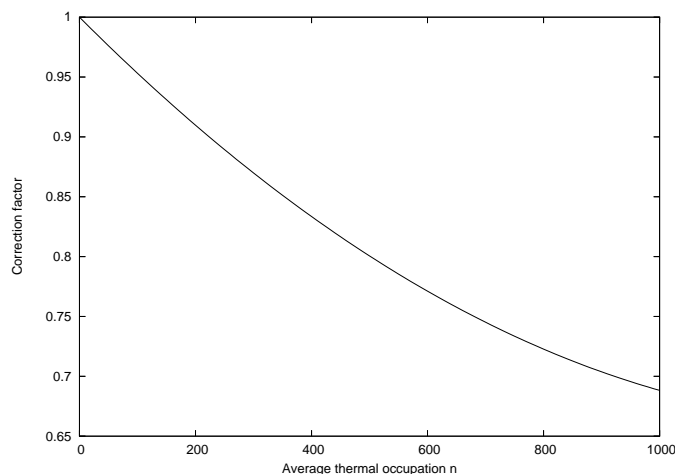


Figure 6.21: The Raman transition rate can be parameterized by A and B , which would ideally be independent of temperature. This graph shows that the coefficient B , as a linear function of A , is not independent of temperature, and must be accounted for in the final heating rate estimate of $\Gamma \approx 1$ quanta per μs .

trap because the spectrum of electric field noise as determined in other experiments [56, 29] has a $\sim 1/f$ dependence, so that the heating rate should be faster the hotter the ion is, and therefore we are overestimating E_{max} (or underestimating t_{boil}) for the perfectly harmonic case. The fact that this method predicts a factor of 60 greater heating rate than the Raman transition measurement suggests that the trap is quite anharmonic far away from the trap minimum. Another possible explanation could be that the heating mechanism that heats in the direction perpendicular to the trap surface is stronger than the one that heats along the trap axis; this is unlikely, however, given that the high aspect ratio of the trap makes the electric field component in this perpendicular direction small compared to the lateral components.

6.7 Future work on two layer traps

In trying to isolate the source of the anomalously high heating rate in the above trap, we searched for the mechanical resonance of the cantilevers using an interferom-

etry setup that detected the motion of the cantilevers. The cantilevers were driving with a 1 V oscillating voltage source to attempt to excite this resonance, but no conclusive resonances were found. To get more heating statistics for another GaAs trap we plan on fabricating a similar structure out of substrate with 10 μm thick $\text{Al}_{0.7}\text{Ga}_{0.3}\text{As}$ layers (thanks to Greg Peake of Sandia National Labs). This will allow us to apply much more voltage because the electric field in the insulator layer will drop by a factor of 2.5 and the power dissipated will drop by 2.5^2 for the same voltage applied.

In our GaAs traps we observed that the ion would move when a laser was applied to an electrode, due to the positive charge imbalance in the area that the laser hit. This is a promising technique for controlling and shuttling ions in a region in which it is difficult to have separated DC electrodes. While we have been able to demonstrate 15 μm shuttling with this technique, we would like to further explore its affect on the ion, especially whether power fluctuations of the laser have a large affect on the heating of the ion. If they do not, this proposal would offer a solution to the speed limit on shuttling, currently set by low pass filters with a shoulder in the 100's of kHz.

We are also looking at fabricating a nearly identical structure out of doped silicon, using silicon oxide as an insulator. This structure was fabricated by using the process shown in figure 6.22. Starting with a heavily doped silicon substrate, 2 μm of thermal oxide were grown on the structure. Then another heavily doped silicon wafer was annealed on top of the oxide layer and mechanically polished down till it is only 5 μm thick. These two steps are repeated again till the same two layer electrode insulator structure is achieved as in the GaAs trap.

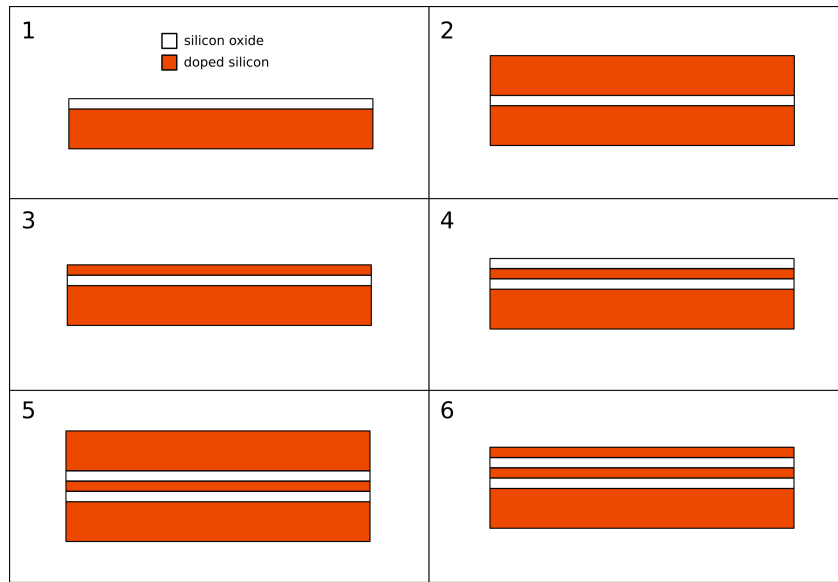


Figure 6.22: A nearly identical structure to that grown with MBE on GaAs can also be fabricated with silicon and silicon oxide. The process starts (1) with a doped silicon wafer with a thermal oxide layer grown on it. Then (2) another doped silicon wafer is annealed to this first one, physically attaching the two. After mechanically polishing this second wafer down to $5\ \mu\text{m}$ (3), another layer of oxide is grown and the process is repeated (4-6), resulting a two layered silicon/silicon oxide heterostructure.

CHAPTER 7

Other microfabricated traps

During my work on the GaAs trap, the Disruptive Technology Office (formerly ARDA) began to sponsor an effort to have outside foundries design and build ion traps which could be scaled to larger systems. As part of my research over the last two years I have been involved in designing the vacuum chamber to host these traps, discussing system requirements with the foundry researchers, and finally testing the traps. This chapter will describe their fabrication processes and our results.

7.1 Lucent trap

The first surface trap was demonstrated at NIST [57] in 2006. It was fabricated on a fused quartz substrate, which was chosen for its low RF loss insulator properties. Gold electrodes were evaporated and then electroplated on top of the quartz in a pattern similar to that shown in figure 3.17c. In this trap the RF node is $40\text{ }\mu\text{m}$ above the surface, and all laser beams come across the surface at an angle to the weak axis. A promising attribute of this trap is the low heating rate of 5 quanta/ms, which is small given the ion-electrode distance. The success of this trap along with the natural advantages of surface traps (discussed in section 3.6) inspired a version fabricated by a group at Lucent, headed by Dick Slusher.

7.1.1 Fabrication

As seen in figure 7.1, these surface traps are fabricated on a silicon substrate with

a layer of silicon nitride insulating the substrate from the aluminum/tungsten DC electrodes. Below the silicon nitride layer is an aluminum ground plane. On top of the nitride layer are two $10\text{ }\mu\text{m}$ tall rails of silicon oxide which hold the RF electrodes off the surface of the trap. These are used to decrease the capacitance between the RF rail and the DC electrodes and allow for higher RF voltage to be applied before breakdown. On top of these rails is a metal layer of aluminum with a bottom layer of tungsten which forms the RF electrodes. The capacitance between the RF rail and one DC electrode is $\sim .1\text{ pF}$, whereas the capacitance between the DC electrode and ground is $\sim 30\text{ pF}$, giving a 300:1 ratio of capacitance which shows that the DC electrodes are effectively RF grounded. A top view of a trap can be seen in figure 7.2.

The RF rails get closer together as they move from left to right in this figure. There are four different spacings: $150\text{ }\mu\text{m}$, $125\text{ }\mu\text{m}$, $100\text{ }\mu\text{m}$, and $75\text{ }\mu\text{m}$. The DC control electrodes in the region where the RF rails are separated by $150\text{ }\mu\text{m}$ are $300\text{ }\mu\text{m}$ wide; everywhere else they are $200\text{ }\mu\text{m}$ wide, with the exception of an electrode meant to separate two ions that is $60\text{ }\mu\text{m}$ wide. The RF rails themselves are $20\text{ }\mu\text{m}$ wide.

7.1.2 Simulations

Because the electrodes on the surface trap are not symmetric about the RF nodal axis, simulations in CPO were particularly useful for determining static voltages which would have zero electric field at the node, and therefore minimal micromotion. To achieve this, the standard simulations are first performed in CPO: 1 volt is applied to the RF rails to find the ponderomotive potential, and then 1 volt is applied to each of the other electrodes while the others are grounded. These DC voltages are linearly added in Mathematica to find an overall DC voltage. After the ponderomotive potential is calculated (see figures 7.3, 7.4, 7.5), the RF minima is found at a position x_0, y_0 .

Once this RF minima is found, the DC potential is calculated for the case where 1 volt is applied to each of the outer left electrodes and a volts are applied to the

Planar Ion Trap Scalable Silicon VLSI

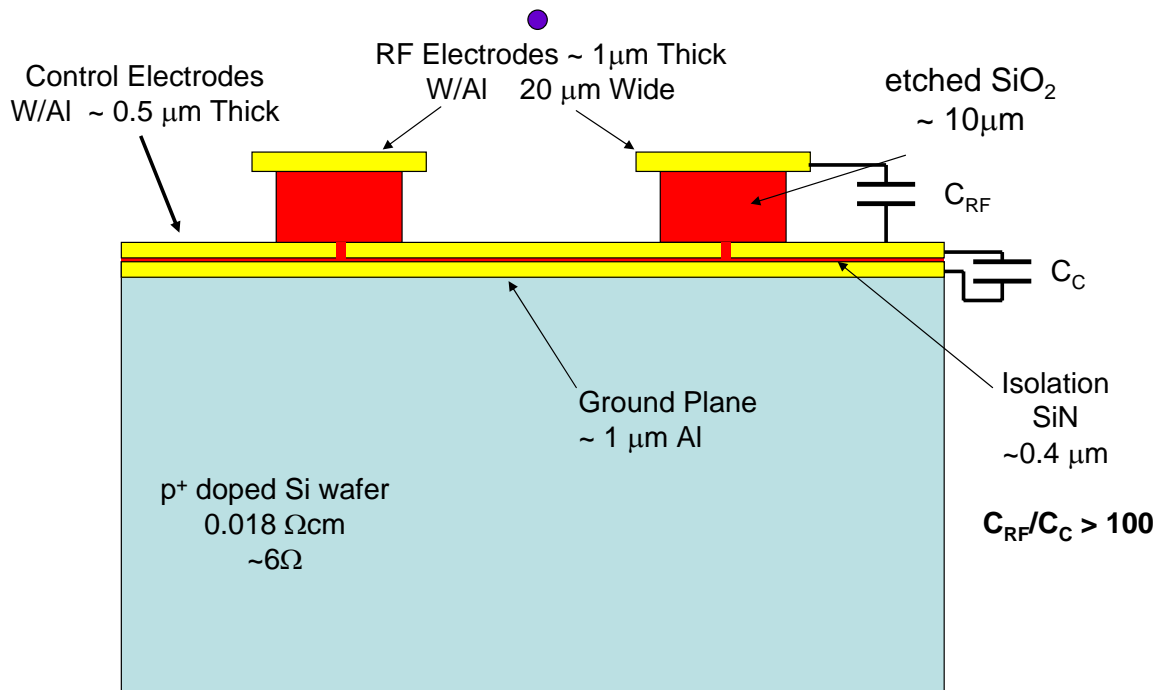


Figure 7.1: This transverse image of the Lucent surface trap (image courtesy of Dick Slusher) shows a cross section of the silicon substrate and electrodes comprising the trap. The RF rails run the length of the trap, with the DC electrodes arranged next to each other like railroad ties.

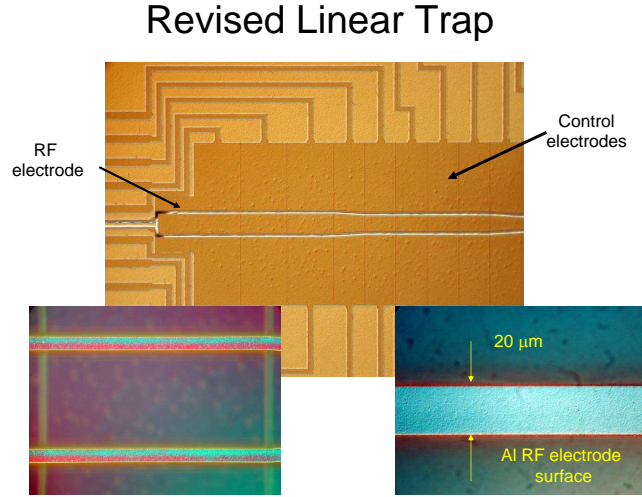


Figure 7.2: This overhead view of the Lucent surface trap (image courtesy of Dick Slusher) shows the DC control electrodes above and below the RF rails. The RF rails come closer to each other while running from left to right, so that heating measurements can be performed in traps with varying ion height. There is one central DC electrode which is connected at the right end (out of view).

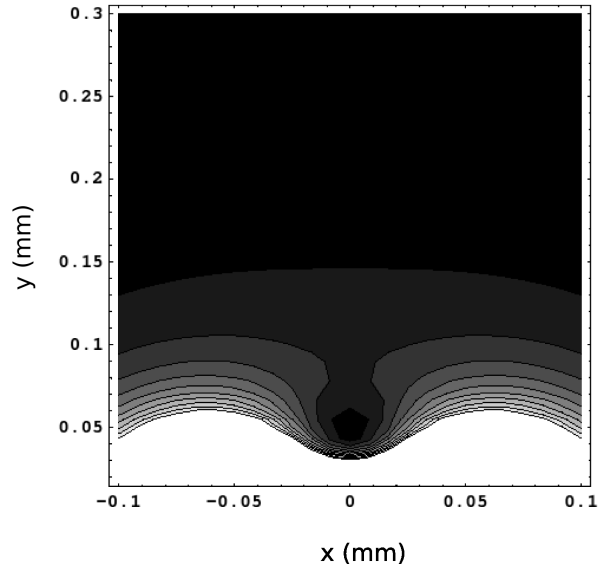


Figure 7.3

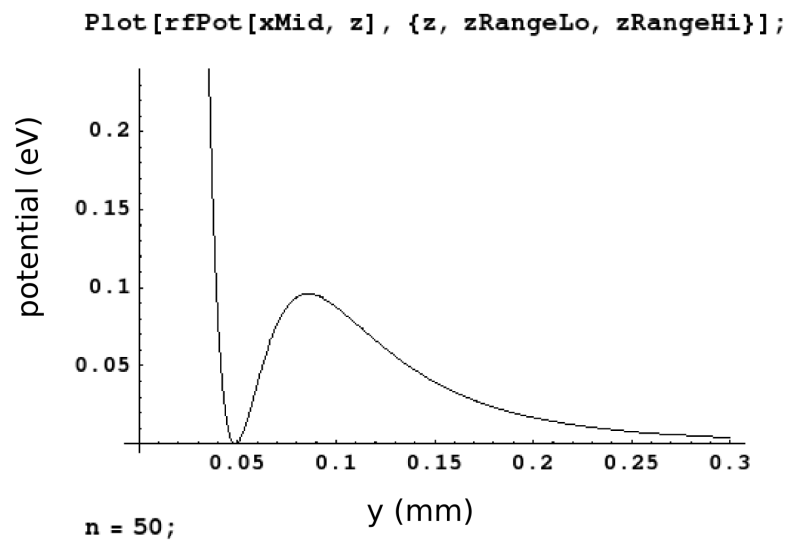


Figure 7.4

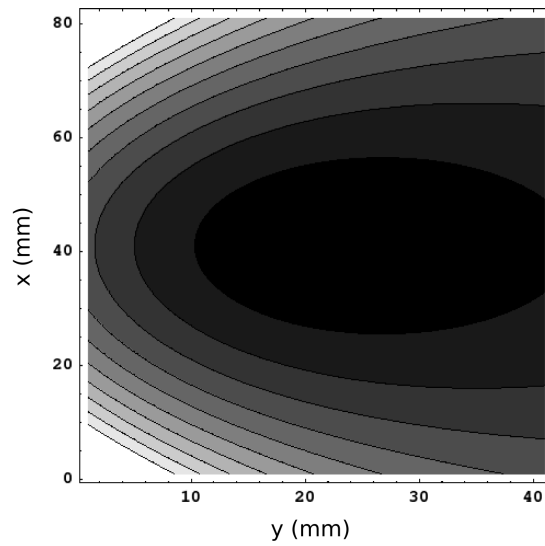


Figure 7.5

middle left one (figure 7.6, where $l = 1$, $r = c = 0$). The voltage a is varied until the electric field in the \hat{x} direction is 0 at the RF node, i.e. $E_x(x_0, y_0) = 0$. Now a voltage c is applied to all electrodes, including the RF rails, until the vertical electric field is zero at the RF node, i.e. $E_y(x_0, y_0) = 0$. Because the same voltage c is applied on all of the electrodes, there will be no E_x component to c , and so now there is no offset electric field at the node. The same analysis can be done for the right electrodes. By applying r volts to the outside right electrodes and ar volts to the middle right electrode, $E_x(x_0, y_0)$ remains 0. However now $E_y(x_0, y_0) \neq 0$; to compensate, we have to add an additional rc volts to all electrodes. To make this more general, we now scale the left outside electrodes to have l volts on them. Once a and c are determined, r and l can be varied in any desirable way (as long as the trap is not destabilized) and $E_x(x_0, y_0) = E_y(x_0, y_0) = 0$. The final applied voltages are shown in figure 7.6.

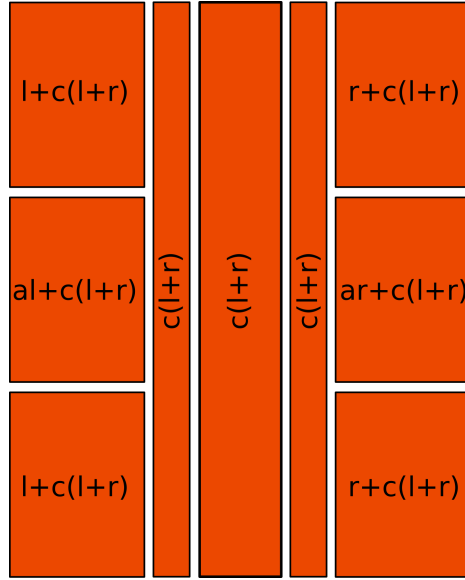


Figure 7.6: To minimize the static electric field at the trap node, the constants a and c must be determined from CPO simulations. Once these are determined, any voltage r and l can be chosen and the electric field at the RF node will be zero.

An example of a DC potential in which the electric field is zero at the RF node can be seen in figure 7.7. The voltages applied to each side are not equal ($l \neq r$) in order to tilt the principal axes of the trap - this can be seen in the contour lines leaning off to one side. Without tilting DC voltages applied, the principal axes are naturally perpendicular and parallel to the plane of the trap. Since the cooling laser comes across the surface of the trap, it is perpendicular to the vertical principal axis, and therefore does not cool the ion's motion in that direction. Therefore the principal axes have to be tilted by applying different voltages to the left and right electrodes. When the ponderomotive potential is combined with the DC potential, the total potential that the ion sees (minus the micromotion driven terms) is shown in the contour plot in figure 7.8. The tilt of the principal axes can be seen in figure 7.9. The difficult aspect of choosing l and r in order to achieve sufficient tilt is that it significantly weakens the nearly vertical axis. Once l and r are chosen such that the axes are tilted and the trap is sufficiently deep, the secular frequency in both the axial direction and both transverse directions is determined, as well as the trap depths. The potential is plotted along these axes and a quadratic fit to the trap minima is calculated to determine the secular frequency.

7.1.3 Operating parameters and results

Of the three traps that we received, we were only able to trap successfully in the first one. This one did not have an aluminum ground plane as shown in figure 7.1, and subsequently had a lower Q than other tested traps ($Q_{loaded} \sim 100$). In traps with this ground plane the loaded Q was closer to 150. We were able to trap in the region with the $150 \mu\text{m}$ separated RF electrodes, with the height of the trap $75 \mu\text{m}$ above the surface. The applied voltages which successfully trapped can be seen in figure 7.11. They generated a principal axis rotation of 12° , a trap depth of .5 eV, and transverse secular frequencies of 5.9 MHz and 5.7 MHz. Up till now we had only applied a maximum of $370 V_{RF}$ to the rails, with up to $10 V_{DC}$ to the control electrodes. Even still we were noticing some of the DC electrodes were shorting to the ground plane

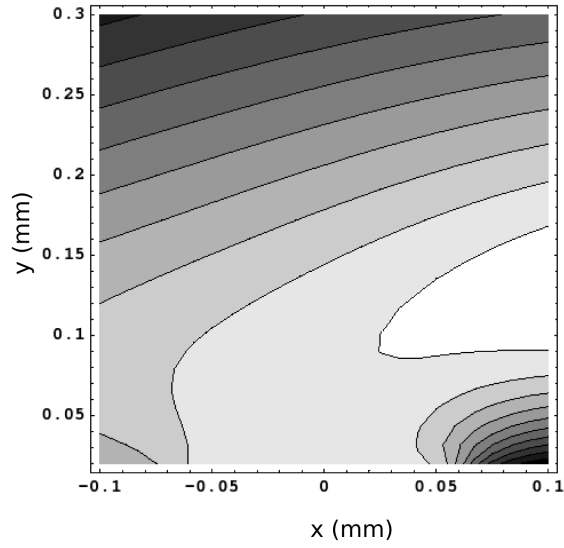


Figure 7.7: This contour plot of the total DC potential applied to the surface trap shows how the principal axes are tilted from perpendicular and parallel to the surface of the trap.

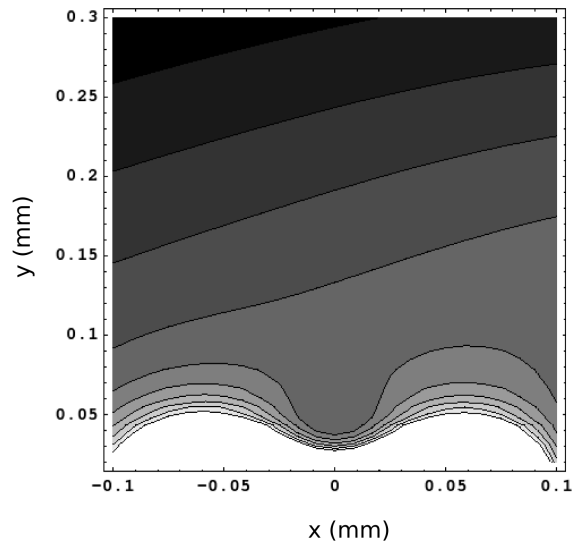


Figure 7.8: The total surface trap potential, including the pseudopotential and the static potential.

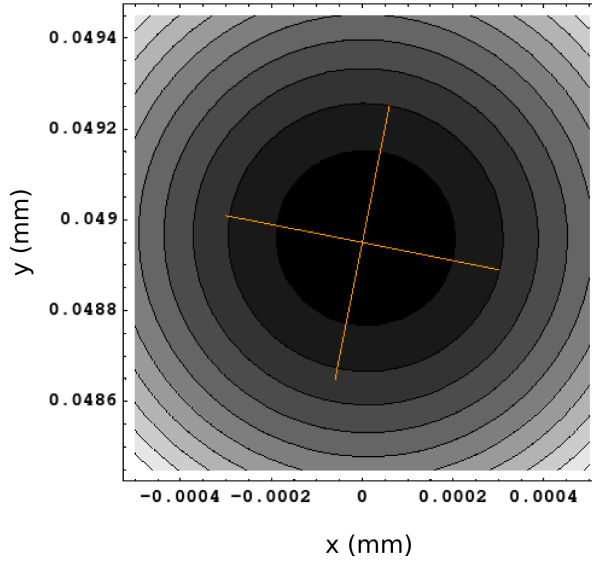


Figure 7.9: The orange lines designate the principal axes of the surface trap, as determined by finding the eigenvectors of the Hessian matrix at the trap minima. Typical values for this tilt are between 5° and 15° .

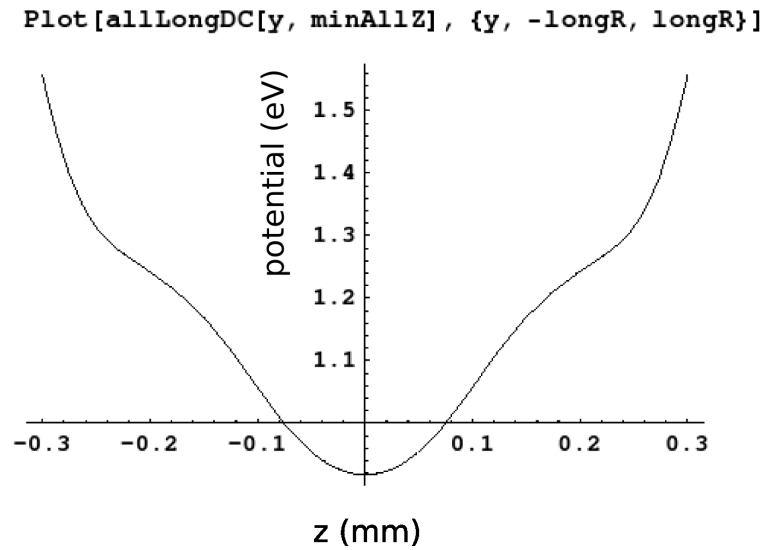


Figure 7.10: The axial potential of the trap is plotted here. The range extends beyond the edges of the middle electrode (which is .3 mm long), which explains the anharmonic nature of the trap. The secular frequency in this direction is determined by fitting a harmonic potential to the bottom of the trap.

below, and this trend continued after we successfully trapped, preventing us from characterizing the trap as much as we would have liked. From the statistics which we were able to collect we found that the ion would stay trapped down to a minimum RF voltage of 250 V, and at 370 V_{RF} would last an average of ~ 1.5 minutes and a maximum of ~ 5 minutes. On the CCD the loaded ion consistently drifted in from the region closer to where the RF wires attach to the rails. We attributed this to a background electric field associated with the pulsed ionization laser. By simply blocking the cooling beam we determined that the ion would last at most 5 s without cooling before it left the trap.

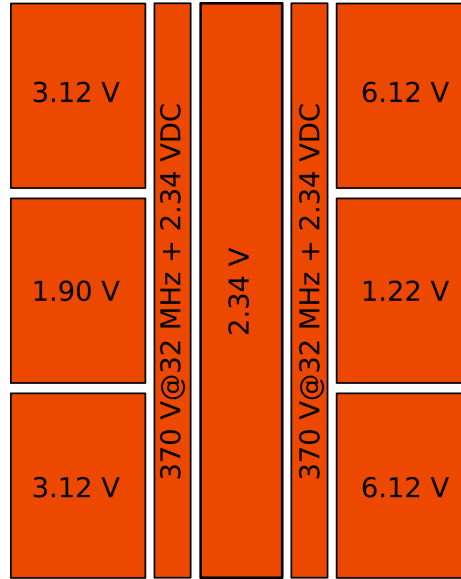


Figure 7.11: These were the voltages applied to the surface trap which were successful at trapping ions.

The next trap we received had a loading slot in it, though this is not something that we needed. In fact, we determined that it could be detrimental since the central DC electrode which we used to compensate for the vertical electric field due to the other DC electrodes was now absent. While we were not successful at loading in this

trap, the group at NIST has successfully used it. From communications with them [58], they witnessed similar lifetimes, problems with DC electrode breakdown, and the ion drifting in from along the RF rail after the photoionization laser is turned off. The last Lucent trap that we received did not have a backside loading slot and did have an aluminum grounding plane. Electrically this trap seemed fine from our in situ measurements of its Q (~ 150) and the RF and DC electrode capacitances. Nonetheless, we were unsuccessful at trapping in this version, and are waiting to try it again in the future.

Assuming the problems encountered with the first few iterations of the Lucent trap can be solved through improved fabrication and operation methods, the upsides to the surface trap are great. For one, surface traps can be combined with on board optics - such as the MEMS mechanical mirrors shown in figure 7.12.

One final area of interest for surface traps is the issue of making a junction. Many trapping geometries suffer from the presence of an RF hump right before the junction region. This feature requires the ion to be shoved over the hump into the junction region where it can be pushed out again. In this process a great deal of motional energy is imparted to the ion (see chapter 5). To minimize this, researchers at NIST [40] have been working with analytic solutions to the trapping potential and have determined surface trap electrode shapes which minimize the residual pseudopotential that comprises the RF hump. In figure 7.13 they show that differently shaped electrodes in the junction region can reduce the RF hump maxima by two orders of magnitude. Interestingly, they note that the curvature of the RF hump does not decrease so drastically, which may mean that significant motional heating is still inevitable through this region.

7.2 Sandia trap

Another type of trap that we tested was fabricated at Sandia National Labs through an effort led by Matt Blain. This trap used a single layer geometry like that shown in figure 3.15a. The RF electrodes as seen in figure 7.14 are made of

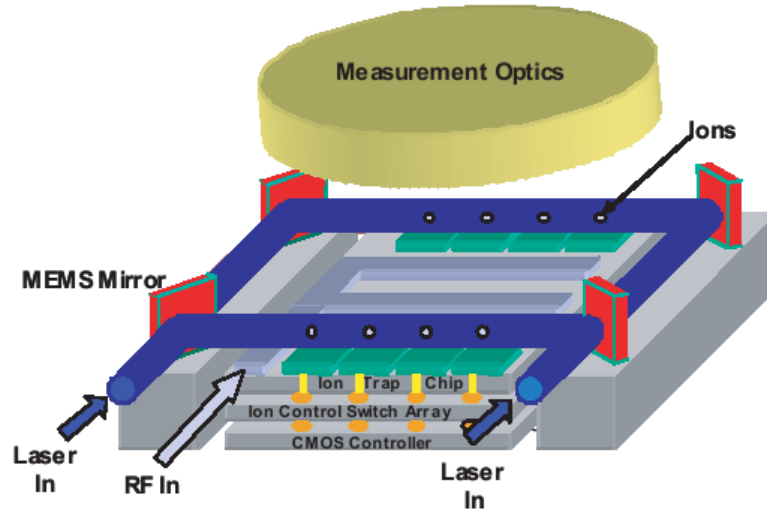


Figure 7.12: This conceptual design of a surface (image courtesy of Dick Slusher) trap shows a possible solution to the problem of having many lasers coming across the surface of the trap which could interfere with ions in other traps. By fabricating movable mirrors in conjunction with the trap, the ions could be illuminated by lasers which reflect off of mirrors positioned and activated depending on the operation to be run. This schematic also shows CMOS circuitry underlying the trap array. By having a library of necessary routines which would be necessary for shuttling or storage, for instance, the electrical control signals, which would otherwise require one wire going out of the vacuum chamber for each electrode, could be run through addressable CMOS logic. Given the large number of separate traps necessary for a viable quantum computer, this aspect will have to be part of any serious proposal.

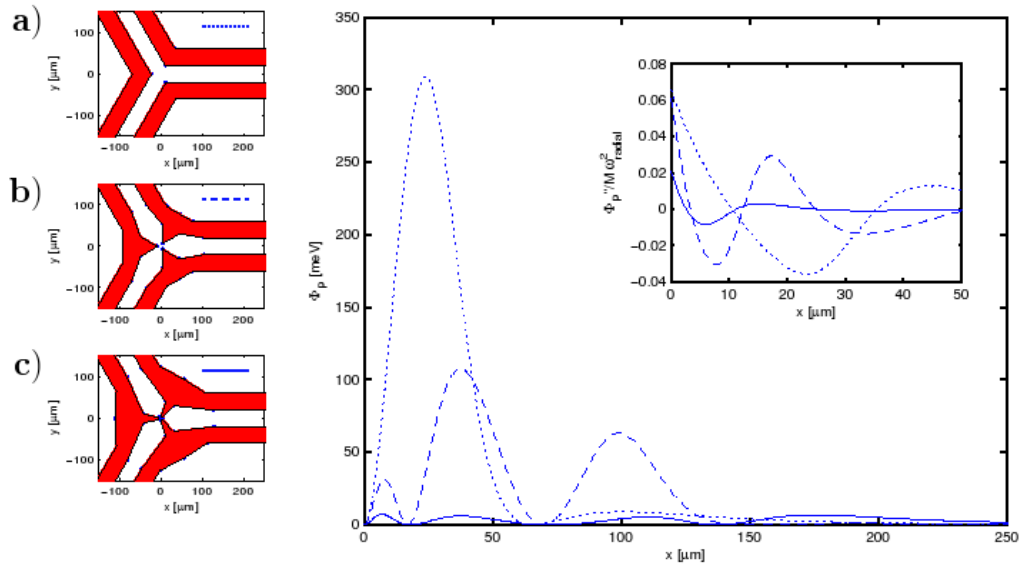


Figure 7.13: The three junctions shown here (image courtesy of Janus Wesenberg) show three different surface electrode geometries in the junction region. From the graph, it is seen that the RF hump potential Φ_P can be suppressed by two orders of magnitude simply by shaping the electrodes. A result of the electrode shaping and subsequent RF hump minimization is that the height of the ion above the trap changes in the junction region, although this is not a particular concern. The inset shows that the curvature of Φ_P is not so drastically suppressed, and this may have more of an implication for the motional heating of the ion as it passes through a junction.

deposited tungsten wires which are held under tension by anchors to each far end of the trap. They use a unique set of circular links which can flex under the tension, so that when the underlying layer is released they do snap under the stress.

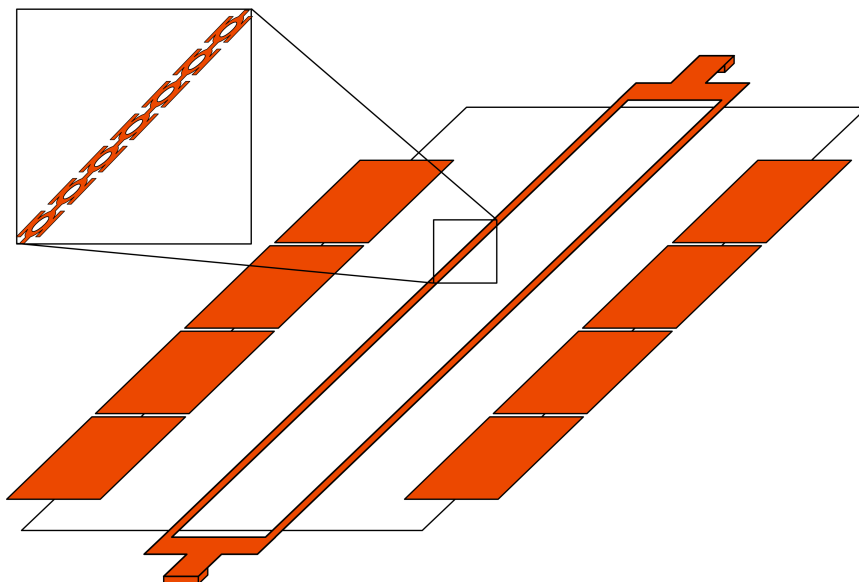


Figure 7.14: The Sandia trap consists of one layer of tungsten electrodes. The RF wires are not solid, but rather consist of linked circles which can flex under the tension provided by the anchors. This tension is a result of the release step which leaves them suspended over empty space. The DC electrodes are supported on the edge of the hole.

While the NIST and Innsbruck groups were able to demonstrate the Sandia trap, we were not able to get it to work. This trap has extremely low capacitance, but as a diagnostic we were able to check that the electrodes were connected as expected by illuminating them with the photoionization laser and detecting the resulting current. The loaded Q of the trap was 70, as expected. Having recently switched lasers for the trap development project, we have recently confirmed that part of the setup by trapping in the needle trap, and plan on testing the Sandia trap again.

7.3 Polysilicon MEMS Exchange trap

The polysilicon trap came out of a proposal for MEMS Exchange, which is a consortium of fabrication facilities used by researchers to fabricate non-production size fabrication jobs. Our proposal to fabricate a two layer ion trapping structure out of polysilicon was started by Bill Noonan is currently being led by Michael Pedersen. One advantage of using polysilicon is a somewhat higher conductivity compared to GaAs - our structure has a sheet resistance of $7.5 \Omega/\text{square}$ for electrodes that are only $.75 \mu\text{m}$ thick. Additionally, the fact that the structure can be fabricated on a silicon substrate allows the possibility in the distant future of integrating CMOS components with it. In the near term, it has the advantage of the backside etch being a relatively simple and accurate KOH etch. Since the polysilicon can be deposited after various processing steps (as opposed to the GaAs MBE requirement), it is much more flexible as far as having vertical structure. For instance, the bridges which NIST uses to make a junction in a two layer trap would be possible in a polysilicon trap. The ability to use polysilicon glass as a temporary spacer before it is removed via wet etching allows air gaps to be used instead of a material insulator between the polysilicon layers. This allows for larger breakdown voltages and lower capacitances between the polysilicon layers. Though the air gap ($2 \mu\text{m}$) is half as thick as in the GaAs trap, the lack of material means that the capacitance is 5 times smaller, so the power dissipated is 25 times smaller than in the GaAs trap, given roughly equal electrode resistances.

Figure 7.16 shows the structure up till the bond pad metallization step. Figure 7.17 shows the final structure after the backside etch. As of the time of the writing of this thesis, MEMS Exchange was having a difficult time removing the silicon nitride from the bottom of the bottom layer cantilevers without damaging them. We have decided that it should not be a serious concern and hope to have the first polysilicon traps in the summer of 2007.

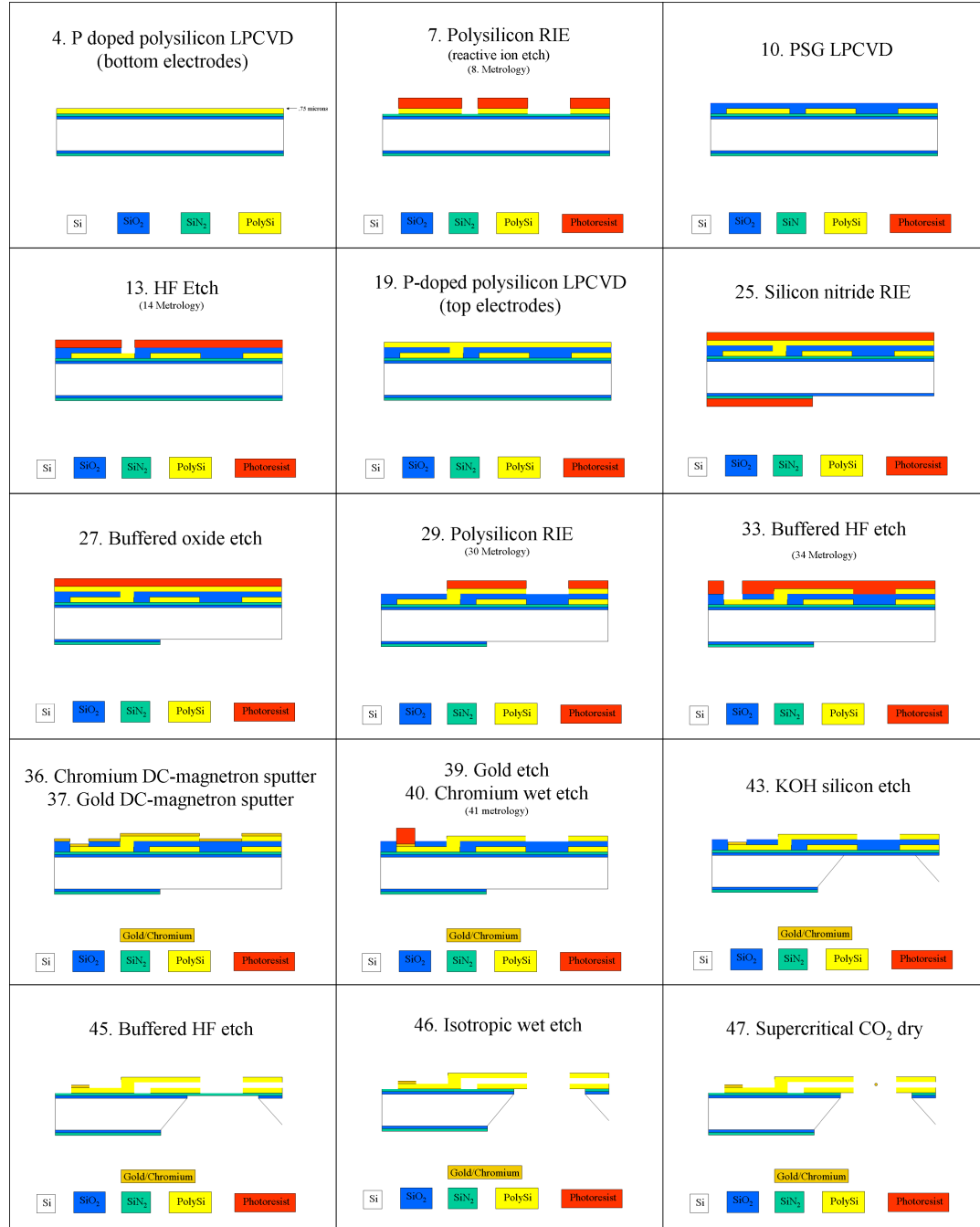


Figure 7.15: This figure shows the important steps in the polysilicon fabrication process (images courtesy of Michael Pedersen). The first steps are to grow thermal oxide and nitride on the wafer as insulation and future masking layers. Then the bottom phosphorous doped polysilicon layer is grown and etched. Polysilicon glass is grown on top of this to space out the second polysilicon layer. At this point the backside nitride and oxide are removed. Then the top layer polysilicon electrodes are defined through a reactive ion etch, and HF is used to expose the electrodes so that chromium and gold can be deposited to form bond pads. After etching the excess metal, a KOH defines the backside hole, followed by a buffered HF etch and an isotropic wet etch to remove all polysilicon glass, and the cantilevers are released after a supercritical dry step.

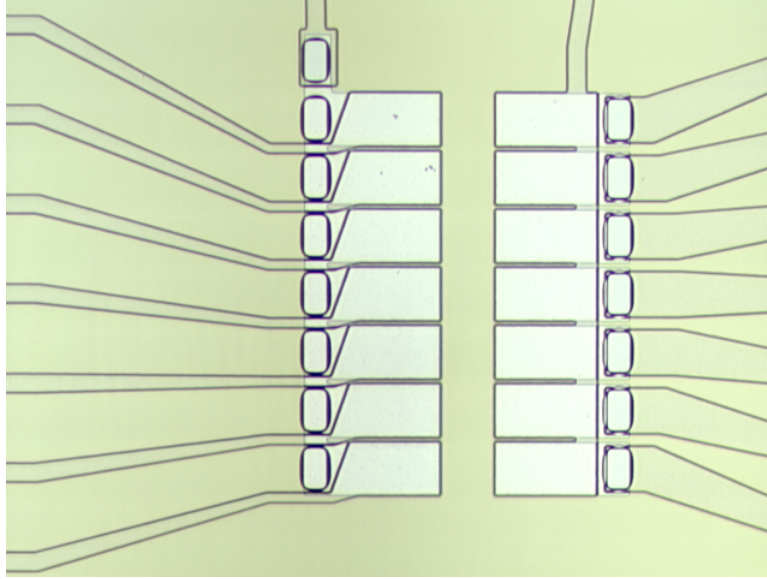


Figure 7.16: This figure shows the polysilicon trap up till the metalization step. For the cantilevers on the right the RF electrodes are on top and the DC electrodes are on the bottom, and visa versa for the left side.

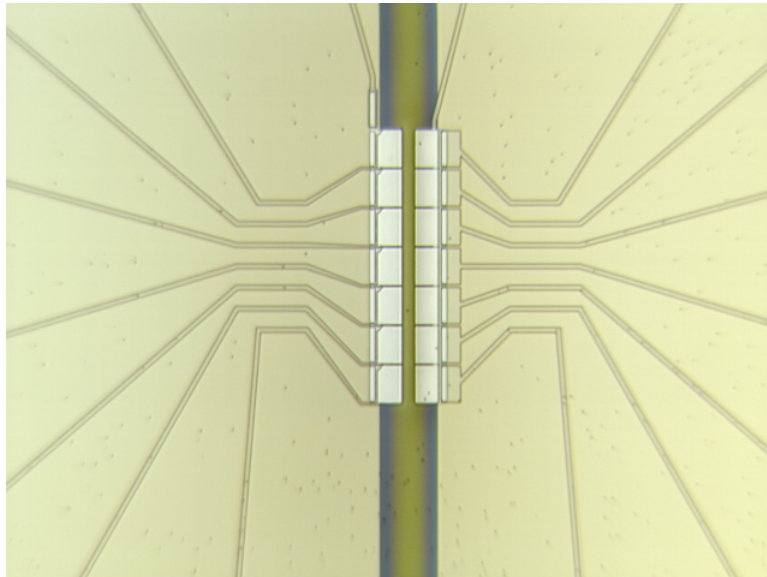


Figure 7.17: This micrograph shows a polysilicon trap which has made it through the entire process. The backside hole can be clearly seen in the figure with the electrodes cantilevered over it.

CHAPTER 8

Sources of motional heating

Voltage fluctuations on surrounding electrodes couple to the motional energy of the ion, in essence heating it. The two primary contributors are thermal (Johnson) noise and patch potential noise, aptly named because it describes voltage fluctuations on a particular region, or patch. When the electrodes are at room temperature, it is orders of magnitude more influential than thermal noise. The subject of heating is particularly important for the microfabricated traps because the spectral density of electric field noise is observed to scale as $\sim 1/z_0^4$ with the ion-electrode distance z_0 , and the typically low potential depths of a microtrap combined with a high heating rate make continuous laser cooling necessary to retain the ion. In addition to ion traps, a related type of noise is observed in other systems, including solid state QC systems [59] and precision measurements of gravity involving proximate masses [60].

In setting out to design an ion trap capable of characterizing the patches in situ, we first had to determine the relevant parameters to vary. From figure 8.1 we see a plot of many different ion traps used in various groups to trap a variety of species [56]. From this plot we can see that regardless of the material used in the trap (this graph shows traps made out of molybdenum, gold coated alumina, and GaAs), the spectral density of electric field noise was similar in each of them, to within about an order of magnitude. Also obvious is the strong dependence on the ion electrode distance. And finally, based on the gray area showing the level of Johnson noise, we can tell that patch potential noise was the dominant effect in each trap. We therefore set out to make a trap with movable electrodes such that the distance z_0 could be

measured [29]. Furthermore we wanted to be able to cool the electrodes to see what effect, if any, temperature had on the patch potential heating.

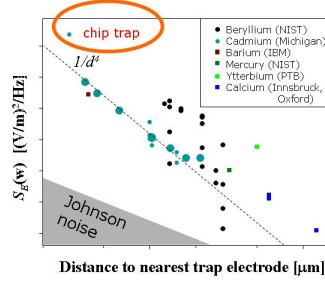


Figure 8.1: Spectral density of electric field noise for different traps and ions: The spectral density of electric field noise is shown here plotted as a function of the electrode to ion distance for a variety of different traps and ions. A line is drawn to guide the eye and reveal the roughly $1/z_0^4$ scaling of S_E .

8.1 Heating rate and spectral density of electric field noise

To model the heating rate (see [42] for additional details), we treat an anomalous electric field $\epsilon(t)$ as a perturbation on the usual Hamiltonian $H_0 = p^2/2m + m^2\omega_z^2 z^2/2$:

$$H = H_0 - q\epsilon(t)z \quad (8.1)$$

First order perturbation theory [24] can be applied to find the the transition rate

from the $|0\rangle$ state to the $|1\rangle$ state:

$$\Gamma_{0 \rightarrow 1} = \frac{1}{\hbar^2} \int_{-\infty}^{\infty} d\tau e^{i\omega_z \tau} \langle \epsilon(t) \epsilon(t + \tau) | \rangle \langle 0 | qz | 1 \rangle^2 \quad (8.2)$$

$$= \frac{q^2}{4m\hbar\omega_z} S_E(\omega_z) \quad (8.3)$$

This is the \dot{n} heating rate that we measure when the ion is first cooled to the ground state and then probed after a delay time with the sideband thermometry technique discussed in chapter 2. We have to add a term corresponding to heating of the micromotion oscillation, so that equation 8.2 becomes:

$$\Gamma_{0 \rightarrow 1} = \dot{n} = \frac{q^2}{4m\hbar\omega_z} (S_E(\omega_z) + \frac{\omega_z^2}{2\Omega^2} S_E(\Omega \pm \omega_z)) \quad (8.4)$$

Note that the micromotion term is at the drive frequency modulated by the secular frequency, $\Omega \pm \omega_z$, as seen from equation 3.11. This additional heating term is reduced by a factor of $\frac{\omega_z^2}{2\Omega^2}$, and so can be ignored for most traps.

8.2 Thermal (Johnson) noise

The incoherent sum of all sources of noise due to thermally fluctuating charges in a conductor [61] is called Johnson noise. The voltage noise from a thermal source is:

$$S_V(\omega) = 4k_B T R(\omega) \quad (8.5)$$

and it is treated as being correlated over the entire electrode. The sum of all these thermal noise sources R_i (given that there are two needles) is [29]:

$$S_V(\omega) = \sum_i \frac{8k_B T_i R_i(\omega)}{1 + R_i(\omega)^2 C_i^2 \omega^2} \quad (8.6)$$

The various R_i sources can be seen in figure 8.2. The dominant contributor is the needle itself, primarily because it is unfiltered. The RF choke R_F and the resonator resistance R_{res} , although both larger, are filtered and so do not contribute signifi-

cantly.

To find the effect of the voltage noise on the ion, we compare it to a parallel plate capacitor separated by $2z_0$. In this case the electric field noise at the ion would be:

$$S_E(\omega) = \frac{S_V(\omega)}{(2z_0)^2} \quad (8.7)$$

In the case of the needle we parametrize its efficiency compared to the capacitor with ϵ :

$$S_E(\omega) = S_V(\omega) \left(\frac{\epsilon}{2z_0} \right)^2 \quad (8.8)$$

From numerical simulations in Maxwell we were able to determine that $\epsilon \approx .7$ for the dimensions of the second needle. Given this, we estimate the total Johnson noise contribution to the heating rate at 300 K to be $\dot{n} \sim (200/z_0)^2 (\omega_z/2\pi)^{-1}$, for z_0 in μm and $\omega_z/2\pi$ in MHz. When the temperature is lowered from 300 K to 150 K we expect the Johnson noise heating rate contribution to fall by a factor of 6; a factor of 2 due to the thermal noise dependence and a factor of 3 due to the resistance in tungsten dropping.

The affect of patch potential noise requires more intensive simulations, as the patch potentials are not considered to be correlated over the size of the needle. For this reason simulations have to be done in which a patch of size α located at position k has 1 volt applied, and the electric field in \hat{z} is measured, at an ion-needle distance z_0 . The electric field then is $E_z = V_n \xi_{k,\alpha,z_0}$. If we plug this formula for E_z into equation 8.2 and sum over all positions k for a single patch size and needle spacing, we can bring the constant sum out front and get:

$$S_E(\omega) = 2 \left(\sum_k (\xi_{k,\alpha,z_0})^2 \right) S_V(\omega) \quad (8.9)$$

That sum $\Xi_\alpha(z_0) = \sum_k (\xi_{k,\alpha,z_0})^2$ could then be plotted versus z_0 for different values of α and compared with actual data to find α .

8.3 Trap construction

The chosen moveable electrode geometry uses two needles attached to linear positioners (see figure 8.2). This type of trap is similar to the hyperbolic traps discussed in chapter 3, with the difference that the radius of the ring electrode is taken to infinity. From numerical simulations performed in Maxwell 3D, it was found that the needle tips had to have a sufficiently low curvature in order to maintain a reasonably high trapping strength, as parametrized by the η variable in equation 8.10:

$$\omega_z = \sqrt{\frac{eV_0\eta}{mz_0^2} + \left(\frac{eV_0\eta}{\sqrt{2}\Omega z_0^2}\right)^2} \quad (8.10)$$

Also, it was discovered after testing the first needle trap that cylindrical electrodes recessed from the needle tips were necessary to shield the ion from stray electric fields that built up on the insulator. Although the first trap iteration (consisting of just needles and no cylindrical grounds) was able to trap, the micromotion of the ion changed over time periods of 10 minutes as a result of repeated firing of the photoionization laser. It is suspected that when the laser hits the boron nitride needle mount (directly or after reflecting off the viewport) it becomes charged up, and that as that charge changes the bias electric fields at the ion changes, which increases the micromotion.

Adding the grounding sleeves also had the added benefit of increasing the efficiency of the trap. In the first needle trap there was no sleeve, and the radius of curvature of the needle tip was $\sim 8 \mu\text{m}$. With these dimensions, η ranged from .08 to .12 as z_0 ranged from $25 \mu\text{m}$ to $75 \mu\text{m}$. In the second needle, which had a grounded sleeve 2.3 mm recessed from the end of the needle and a tip with a $3 \mu\text{m}$ radius of curvature, η ranged from .16 to .18 as z_0 ranged from $25 \mu\text{m}$ to $250 \mu\text{m}$. In each case the needle electrodes were made out of tungsten rods which were mechanically polished (with a dremel tool and fine grain sand paper) and chemically polished (with phosphoric and HF acid) to a point with a 4° half angle. Typical operating values for this trap are $U_0 = 0$ and $V_0 = 600$ at $\Omega/2\pi = 29 \text{ MHz}$ and $z_0 = 136 \mu\text{m}$, $\omega_z/2\pi = 2.77 \text{ MHz}$.

8.4 Heating results

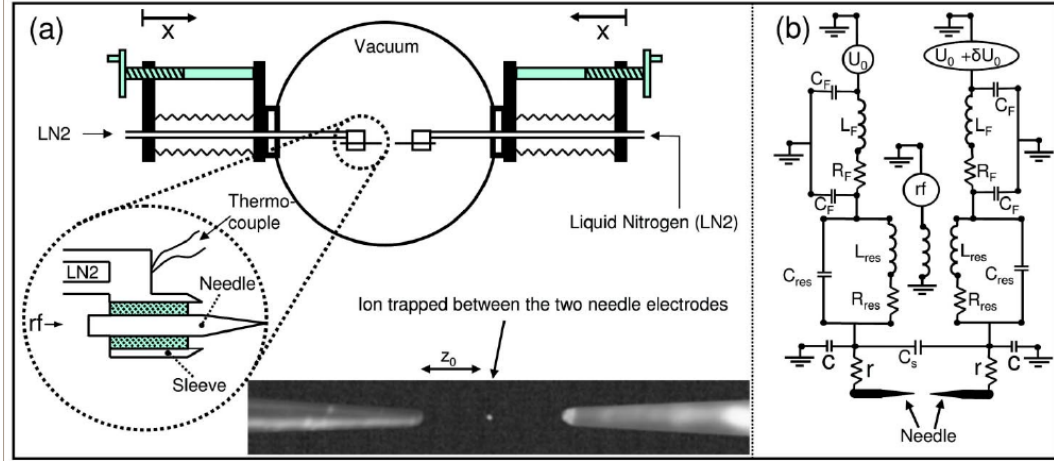


Figure 8.2: Needle schematic: This schematic diagram of the needle trap shows the vacuum chamber, liquid nitrogen cooled cold fingers, and needle and sleeve electrodes in part **a**. The inset shows a composite image of the actual needles illuminated on the CCD camera with an ion in the middle. In part **b** the circuit diagram for the needle structure is shown.

First the heating rate \dot{n} was measured as a function of the trap frequency (figure 8.3) using sideband thermometry. In this case the trap distance was fixed at $z_0 = 103 \mu\text{m}$ while keeping $V_0 = 600 \text{ V}$ and changing U_0 to change the trap frequency ω_z . The graph shows the data from this experiment (the last point uses $V_0 = 700 \text{ V}$). The fit to this data reveals $\dot{n} \sim \omega^{-1.8 \pm 0.2}$, or $S_E(\omega) \sim \omega^{-0.8 \pm 0.2}$ obeys a $1/f$ noise scaling law.

Secondly, the heating rate was measured as a function of ion-electrode spacing z_0 . From figure 8.4, the 300 K data follows a relatively straight line (corresponding to a power law in this log log plot). The data was taken at a trap frequency of $\omega_z/2\pi = 2.07 \text{ MHz}$, where both the static and RF voltages were changed as z_0 changed to maintain the same trap frequency. The line is fit to $\dot{n} \sim z_0^{-3.5 \pm 0.1}$. At 150 K, the second and third data points were taken with $\omega_z/2\pi = 2.07 \text{ MHz}$, while the first point was taken at $\omega_z/2\pi = 4.9 \text{ MHz}$ and scaled according to the fit in figure 8.3. Based on previous experiments we know that increased RF voltage does not increase the heating rate, provided the secular frequency and distances are the same. The gray region shows the heating rate from thermal noise expected for this trap; for both of the temperature shows here it is well over an order of magnitude lower than that measured. Additionally, the observed noise does not follow the expected $1/z_0^2$

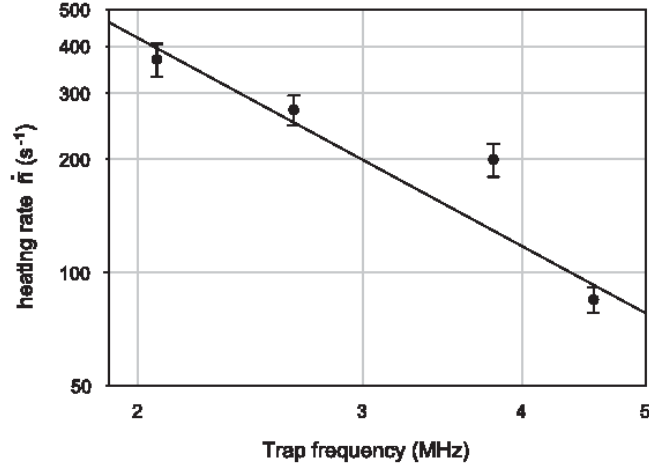


Figure 8.3: Heating rate in the needle trap as a function of trap frequency: In this experiment the RF potential and trap distance were held constant, only varying U_0 to change ω_z .

relationship with heating rate and distance.

8.5 Future work - molybdenum trap

We are currently in the process of testing a needle trap nearly identical to the aforementioned needle, but with needles made of molybdenum rather than tungsten. Molybdenum was chosen because the work function of its oxide is nearly identical to the work function of the metal. It is thought that electrons hopping from the metal to the oxide could be related to the source of patch potential noise, and by using a metal where there is no potential difference between these transitions, perhaps the anomalous heating rate will be suppressed. Additionally, there is historical evidence that molybdenum is an ideal material as a ring and fork molybdenum trap was tested with a heating rate so low it could not be measured with sideband thermometry. That heating rate eventually rose over the course of the experiment due to contamination from the ovens being fired.

An additional feature of the molybdenum trap is the heaters on each needle to provide finer temperature control. While liquid nitrogen will still be used to cool the electrodes, the heaters (which consist of tungsten wire wrapped around a ceramic

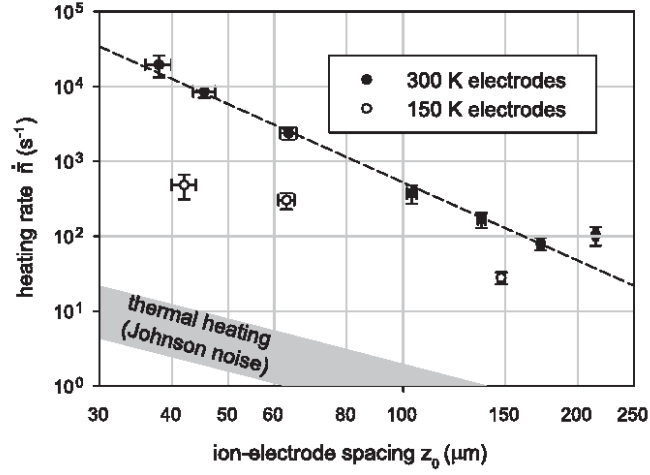


Figure 8.4: Heating rate in the needle trap as a function of trap distance: In this experiment the trap frequency was held constant while the needles were moved apart with the linear positioner, varying U_0 and V_0 to maintain a constant ω_z .

core and covered by a ceramic tube) will be able to regulate more finely (there are thermocouples on each needle mount as well) the temperature of the needle. We hope this data will give further insight into the nature of patch potentials.

CHAPTER 9

Conclusion

In conclusion, the experiments presented here, namely constructing microfabricated traps, shuttling ions in junction regions, and characterizing motional heating due to patch potentials on the trap electrodes, are meant to demonstrate the efficacy of constructing a trapped ion quantum computer. My focus has been on the scalability requirement, leaving discussions on the progress made in the other equally important DiVincenzo criteria (section 1.4) to other texts and research groups [30, 62]. Over the last few years research in extending the number of entangled qubits [63], improving gate fidelities, and increasing coherence times has achieved impressive results and had a postivitive effect in driving interest in the work presented here. While the time frame is uncertain, hopefully it is apparent to the reader that the field of trapped ion quantum computing holds a promising future.

BIBLIOGRAPHY

BIBLIOGRAPHY

- [1] W Paul. Electromagnetic traps for charged and neutral particles. *Rev. Mod. Phys.*, 62:531–540, 1990.
- [2] H G Dehmelt. Radiofrequency spectroscopy of stored ions i: Storage. *Adv. Atom. Mol. Phys.*, 3:53–72, 1967.
- [3] F Diedrich, J C Bergquist, W M Itano, and D J Wineland. Laser cooling to the zero-point energy of motion. *Phys. Rev. Lett.*, 62(14):403–406, October 1989.
- [4] D L Moehring, B B Blinov, D W Gidley, R N Kohn Jr., M J Madsen, T B Sanderson, R S Vallery, and C Monroe. Precision lifetime measurement of a single trapped ion with ultrafast laser pulses. *Phys. Rev. A*, 73:023413, 2006.
- [5] S Diddams, T Udem, J C Bergquist, E A Curtis, R E Drullinger, L Hollberg, W M Itano, W D Lee, C W Oates, K R Vogel, and D J Wineland. An optical clock based on a single trapped $^{199}\text{Hg}^+$ ion. *Science*, 293:825–828, 2001.
- [6] D J Wineland, C Monroe, W M Itano, D Leibfried, B E King, and D M Meekhof. Experimental issues in coherent quantum-state manipulation of trapped atomic ions. *J. Res. Nat. Inst. Stand. Tech.*, 103:259–328, May 1998.
- [7] D P Divincenzo. The physical implementation of quantum computation. *Fortschritte der Physik*, 48:771–783, 2000.
- [8] M J Bass and C M Christensen. The future of the microprocessor business. *IEEE Spectrum*, 39(4):34–39, 2002.
- [9] R P Feynman. Simulating physics with computers. *Int. J. Th. Phys.*, 21(6/7):467–488, 1981.
- [10] D. Deutsch. Quantum-theory, the church-turing principle and the universal quantum computer. *Proceedings of the Royal Society of London Series A - Mathematical, Physical, and Engineering Sciences*, 400(1818):97 – 117, 1985.
- [11] P W Shor. Algorithms for quantum computation: Discrete logarithms and factoring. In *Proceedings of the 35th Annual Symposium on the Foundations of Computer Science*, page 124, New York, 1994. IEEE Computer Society, IEEE Computer Society Press.
- [12] M Nielsen and I Chuang. *Quantum Computation and Quantum Information*. Cambridge University Press, 2000.
- [13] C Pomerance. A tale of two sieves. *Notices of the AMS*, pages 1473–1485, 1996.

- [14] 2005.
- [15] A Steane. Error correcting codes in quantum theory. *Phys. Rev. Lett.*, 77(5):793–796, July 1996.
- [16] S Aaronson. Np-complete problems and physical reality. *quant-ph/0502072*, 2005.
- [17] D P DiVincenzo. Quantum computation. *Science*, 270(1):255–261, October 1995.
- [18] P O Schmidt, T Rosenband, C Langer, W M Itano, J C Bergquist, and D J Wineland. Spectroscopy using quantum logic. *Science*, 309:749–752, 2005.
- [19] C Monroe, D M Meekhof, B E King, W M Itano, and D J Wineland. Demonstration of a fundamental quantum logic gate. *Phys. Rev. Lett.*, 75(25):4714–4717, December 1995.
- [20] F schmidt Kaler, H Haffner, M Riebe, S Gulde, G Lancaster, T Deuschle, C Becher, C Roos, J Eschner, and R Blatt. Realization of the Cirac-Zoller controlled-NOT quantum gate. *Nature*, 422:408–411, 2003.
- [21] K Mølmer and A Sørensen. Multiparticle entanglement of hot trapped ions. *Phys. Rev. Lett.*, 82:1835–1838, 1999.
- [22] J J Garcia-Ripoll, P Zoller, and J I Cirac. Speed optimized two-qubit gates with laser coherent control techniques for ion trap quantum computing. *Phys. Rev. Lett.*, 91:157901, 2003.
- [23] M Acton, K A Brickman, P C Haljan, P J Lee, L Deslauriers, and C Monroe. Near-perfect simultaneous measurement of a qubit register. *Quantum Information and Computation*, 6:465, 2006.
- [24] Richard Liboff. *Introductory Quantum Mechanics, 3rd Ed.* Addison-Wesley, New York, 1998.
- [25] R Ozeri, C Langer, J D Jost, B DeMarco, A Ben-Kish, B R Blakestad, J Britton, J Chiaverini, W M Itano, D B Hume, D Leibfried, T Rosenband, P O Schmidt, and D J Wineland. Hyperfine coherence in the presence of spontaneous photon scattering. *Phys. Rev. Lett.*, 95:030403, 2005.
- [26] D J Wineland, R E Drullinger, and F L Walls. Radiation-pressure cooling of bound resonant absorbers. *Phys. Rev. Lett.*, 40:1639–1642, 1978.
- [27] D J Wineland and W M Itano. Laser cooling of atoms. *Phys. Rev. A*, 20(4):1521–1540, October 1979.
- [28] H J Metcalf and P van der Straten. *Laser Cooling and Trapping*. Springer, New York, 1999.

- [29] L Deslauriers, S Olmschenk, D Stick, W K Hensinger, J Sterk, and C Monroe. Scaling and suppression of anomalous quantum decoherence in ion traps. *Phys. Rev. Lett.*, 97:103007, 2006.
- [30] D Leibfried, R Blatt, C Monroe, and D Wineland. Quantum dynamics of single trapped ions. *Rev. Mod. Phys.*, 75:281, 2003.
- [31] P K Ghosh. *Ion Traps*. Clarendon Press, Oxford, 1995.
- [32] G. M. Murphy. *Ordinary Differential Equations and their Solutions*. D. Van Nostrand Company, Inc., Princeton, NJ, 1960.
- [33] N. W. McLachlan. *Theory and Application of Mathieu Functions*. Dover Publications, Inc., New York, NY, 1964.
- [34] H G Dehmelt. *Advances in Atomic and Molecular Physics*, volume 3. Academic Press, Inc., New York, 1967.
- [35] B Blinov, L Deslauriers, P Lee, M Madsen, R Miller, and C Monroe. Sympathetic cooling of trapped cd^+ isotopes. *Phys. Rev. A*, 65:040304, 2002.
- [36] S R Jefferts, C Monroe, E Bell, and D J Wineland. Coaxial-resonator driven rf (paul) trap for strong confinement. *Phys. Rev. A*, 51(4):3112–3116, April 1995.
- [37] M Madsen, W Hensinger, D Stick, J Rabchuk, and C Monroe. Planer ion trap geometry for microfabrication. *Appl. Phys. B*, 78:639, 2004.
- [38] S R Valluri, D J Jeffery, and R M Corless. Some applications of the lambert w function to physics. *Can. J. Phys.*, 78:823, 2000.
- [39] J Chiaverini, R B Blakestad, J Britton, J D Jost, C Langer, D Leibfried, R Ozeri, and D J Wineland. Surface-electrode architecture for ion-trap quantum information processing. *Quantum Information and Computation*, 5(6):419–439, 2005.
- [40] J Wesenberg and R Reichle. private communication, 2006.
- [41] W W Macalpine. Coaxial resonators with helical inner conductor. *Proceedings of the IRE*, 1959.
- [42] Q A Turchette, D Kilepinski, B E King, D Leibfried, D M Meekhof, C J Myatt, M A Rowe, C A Sackett, C S Wood, W M Itano, C Monroe, and D J Wineland. Heating of trapped ions from the quantum ground state. *Phys. Rev. A*, 61:063418, June 2000.
- [43] L Deslauriers, M Acton, B Blinov, K Brickman, P Haljan, W Hensinger, D Hucul, S Katnik, R Kohn, P Lee, M Madsen, P Maunz, S Olmschenk, D Moehring, D Stick, J Sterk, M Yeo, K Younge, and C Monroe. Efficient photoionization loading of trapped ions with ultrafast pulses. *Phys. Rev. A*, 74(6):063421, 2006.

- [44] A Yariv and P Yeh. *Optical Waves in Crystals*. John Wiley & Sons, New York, 1984.
- [45] P J Lee, B B Blinov, K Brickman, L Deslauriers, M J Madsen, R Miller, D L Moehring, D Stick, and C Monroe. Atomic qubit manipulations with an electro-optic modulator. *Optics Lett.*, 28:1852, 2003.
- [46] K A Brickman, P C Haljan, P J Lee, M Acton, L Deslauriers, and C. Monroe. Implementation of grover’s quantum search algorithm in a scalable system. *Phys. Rev. A*, 72(050306(R)), 2005.
- [47] W Hensinger, S Olmschenk, D Stick, D Hucul, M Yeo, M Acton, L Deslauriers, C Monroe, and J Rabchuk. T-junction ion trap array for two-dimensional ion shuttling, storage, and manipulation. *Applied Physics Letters*, 88(3), 2006.
- [48] M A Rowe, A Ben-Kish, B DeMarco, D Leibfried, V Meyer, J Beall, J Britton, J Hughes, W M Itano, B Jelenkovic, C Langer, T Rosenband, and D J Wineland. Transport of quantum states and separation of ions in a dual rf ion trap. *Quantum Information and Computation*, 2(4):257–271, 2002.
- [49] D Hucul, M Yeo, W K Hensinger, J Rabchuk, S Olmschenk, and C Monroe. On the transport of atomic ions in linear and multidimensional ion trap arrays. *arxiv*, quant-ph/0702175, 2007.
- [50] J P Cleveland, S Manne, D Bocek, and P K Hansma. A nondestructive method for determining the spring constant of cantilevers for scanning force microscopy. *Rev. Sci. Instr.*, 64:403–405, 1993.
- [51] R G Beck, M A Eriksson, R M Westervelt, K D Maranowski, and A C Gossard. Measuring the mechanical resonance of a gaas/algaas cantilever using a strain-sensing field-effect transistor. *Semicond. Sci. Tech.*, 13:A83–A85, 1998.
- [52] et al D E Aspnes. Gaas lower conduction band minima: Ordering and properties. *Phys. Rev. B*, 14(12):5331–5343, 1976.
- [53] M Mangalaraj, M Radhakrishnan, and C Balasubramanian. Electrical conduction and breakdown properties of silicon nitride films. *Journal of Materials* 17, pages 1474–1478, 1982.
- [54] D Rutledge. *The electronics of radio*. Cambridge University Press, Cambridge, UK, 1999.
- [55] Ralph Williams, editor. *Modern GaAs Processing Methods*. Artech House, Boston, MA, 1990.
- [56] L Deslauriers, P C Haljan, P J Lee, K-A Brickman, B B Blinov, M J Madsen, and C Monroe. Zero-point cooling and low heating of trapped cd ions. *Phys. Rev. A*, 70:043408, 2004.

- [57] S Seidelin, J Chiaverini, R Reichle, J J Bollinger, D Leibfried, J Britton, J H Wesenberg, R B Blakestad, R J Epstein, D B Hume, W M Itano, J D Jost, C Langer, R Ozeri, N Shiga, and D J Wineland. Microfabricated surface-electrode ion trap for scalable quantum information processing. *Phys. Rev. Lett.*, 96:253003, 2006.
- [58] D Leibfried. private communication, 2006.
- [59] J M Martinis, S Nam, J Aumentado, K M Lang, and C Urbina. Decoherence of a superconducting qubit due to bias noise. *Phys. Rev. B*, 67:094510, 2003.
- [60] C W Stubbs, E G Adelberger, F J Raab, J H Gundlach, B R Heckel, K D McMurry, H E Swanson, and R Watanabe. Search for an intermediate-range interaction. *Phys. Rev. Lett.*, 58(11):1070–1073, 1987.
- [61] J Johnson. Thermal agitation of electricity in conductors. *Phys. Rev.*, 32:97, 1928.
- [62] D Leibfried, B DeMarco, V Meyer, D Lucas, M Barrett, J Britton, W M Itano, B Jelenkovic, C Langer, T Rosenband, and D J Wineland. Experimental demonstration of a robust, high-fidelity geometric two ion-qubit phase gate. *Nature*, 422:412–415, 2003.
- [63] H Häffner et al. Scalable multiparticle entanglement of trapped ions. *Nature*, 438:643–646, 2005.